Czech Technical University in Prague

Faculty of Nuclear Sciences and Physical Engineering

DISSERTATION

Advanced Three-Dimensional Architectures of Graphene

Prague, 2022 Ing. Martin Šilhavík

Bibliografický záznam

Autor	Ing. Martin Šilhavík České vysoké učení technické v Praze Fakulta jaderná a fyzikálně inženýrská Katedra fyzikální elektroniky
Název práce	Pokročilé Třídimenzionální Struktury Grafenu
Studijní program	Aplikace přírodních věd
Studijní obor	Fyzikální inženýrství
Školitel	RNDr. Antonín Fejfar, CSc. Fyzikální ústav AV ČR
Školitel specialista	doc. Ing. Ivan Richter, Dr. České vysoké učení technické v Praze Fakulta jaderná a fyzikálně inženýrská Katedra fyzikální elektroniky
Akademický rok	2022-2023
Počet stran	128
Klíčová slova	3D grafen, grafenový aerogel, superelasticita, mechanické senzory, odolnost plameni,

Bibliographic entry

Author	Ing. Martin Šilhavík Czech Technical University in Prague Faculty of Nuclear Sciences and Physical Engineering Department of Physical Electronics
Title of Dissertation	Advanced Three-Dimensional Architectures of Graphene
Degree Programme	Applications of Natural Sciences
Field of Study	Physical Engineering
Supervisor	RNDr. Antonín Fejfar, CSc. Institute of Physics of the Czech Academy of Sciences
Supervisor specialist	doc. Ing. Ivan Richter, Dr. Czech Technical University in Prague Faculty of Nuclear Sciences and Physical Engineering Department of Physical Electronics
Academic Year	2022-2023
Number of Pages	128
Keywords	3D graphene, graphene aerogel, superelasticity, mechanical sensors, flame resistance

Declaration

I hereby declare I have written this dissertation independently and quoted all the sources of information used in accordance with methodological instructions on ethical principles for writing an academic thesis. Moreover, I state that this thesis has neither been submitted nor accepted for any other degree.

In Prague, 2022

……

Ing. Martin Šilhavík

Abstrakt

Grafenové aerogely, trojrozměrné porézní struktury sestávající se z navzájem propojených grafenových vrstev, byly detailně studovány od roku 2010, jako jedno z potenciálních řešení pro využití vlastností grafenu v makroměřítku. Tato práce se zaměřuje na výzvy spojené s vývojem robustních 3D grafenových aerogelů pomocí bezšablonové metody přípravy. Tato metoda využívá na začátku oxid grafenu, který je převeden na 3D strukturu kovalentně zesíťovaného grafenu s póry vyplněnými vzduchem. Práce nabízí praktické řešení pro zlepšení reprodukovatelnosti výrobní metody obrácením stárnutí prekurzorů oxidu grafenu pomocí kyslíkového plazmatu. Jsou zkoumány účinky různých teplot žíhání grafenových aerogelů. Je prokázáno, že vysokoteplotní žíhání, při teplotách >1300 °C, umožňuje úplné odstranění kyslíku a vytvoření kovalentního zesítění mezi jednotlivými grafenovými listy v aerogelech. Takto připravené aerogely vykazují výjimečně vysokou elasticitu v tlaku i tahu a zároveň největší měrnou mez kluzu v tlaku, která byla dosud pozorována u jakéhokoli materiálu. Nekonvenční elastické chování v tlaku je vysvětleno analytickým modelem, který je založen na výjimečné flexibilitě jednotlivých atomárně tenkých grafenových vrstev. Grafenové aerogely navíc vykazují nezvyklé tlumení se schopností tlumit mechanické vibrace během nanosekund. Grafenový aerogel také vykazuje jednu z nejvyšších elektrických vodivostí uváděnou u trojrozměrných grafenových materiálů a jednu z nejnižších tepelných vodivostí u pevných látek. Kombinace výjimečných mechanických, elektrických a tepelných vlastností je využita v několika praktických aplikacích. Grafenové aerogely jsou použity k výrobě ultrarychlých, citlivých a širokorozsahových hmatových senzorů. Široký rozsah pracovní zátěže a tlaku umožňuje pokrýt celý rozsah lidské činnosti v rámci jednoho senzoru. Senzory navíc vykazují zanedbatelnou hysterezi, díky které je lze použít pro měření deformace a současně s tím i tlaku. Senzory využívají nový detekční mechanismus založený na měření kontaktního odporu, který přináší několik výhod pro využití v biomedicínských aplikacích, nositelné elektronice a robotice. Grafenový aerogel je nakonec použit jako ohnivzdorný materiál, který vykazuje nekonvenční odolnost vůči plamenu se samozhášecí schopností až do 1500 °C. Všechny tyto výsledky ukazují, že vysoce kvalitní grafenové aerogely jsou jedinečnou třídou materiálů, které mohou zachovat některé jedinečné vlastnosti grafenu, a současně přinášejí mnoho vzrušujících příležitostí, pro vývoj nových funkčních materiálů a zařízení.

Abstract

Graphene aerogels, three-dimensional porous structures consisting of interconnected graphene layers, have been deeply studied since 2010 as one of the solutions for utilizing graphene properties on a macroscale. This thesis focuses on the challenges associated with developing robust and elastic 3D graphene aerogels using a template-free synthesis method. The method starts with graphene oxide which is converted into a 3D structure of covalently cross-linked graphene with air-filled pores. The thesis provides a practical solution for improving the reproducibility of the fabrication method by reversing the ageing of graphene oxide precursors using oxygen plasma. The effects of different annealing temperatures of graphene aerogels are investigated. It is demonstrated that high-temperature annealing at temperatures > 1300 °C enables the complete removal of oxygen and the creation of covalent cross-linking among individual graphene sheets in the aerogels. The as-prepared graphene aerogels exhibit exceptionally high compressive and tensile elasticity and the largest specific compressive yield strength observed in any material so far. The unconventional elastic behavior in compression is explained by an analytical modular origami bending model which is based on the exceptional flexibility of individual atomic graphene layers. Additionally, the graphene aerogels show anomalous damping with the ability to damp mechanical vibrations within nanoseconds. The graphene aerogel also exhibits one of the highest electrical conductivity reported in three-dimensional graphene materials and one of the lowest thermal conductivity in solid-state materials. The combination of exceptional mechanical, electrical and thermal properties is used in several practical applications. The graphene aerogels are used for the fabrication of ultrafast, sensitive, and broad-range tactile sensors. The wide working strain and pressure range enable it to cover the whole human bodily action range within a single sensor. Additionally, the sensors demonstrate negligible hysteresis, which can be used for simultaneous strain and pressure measurement. The sensors utilize a novel sensing mechanism based on contact resistance detection, which brings several advantages for the development of sensors in biomedicine, wearable electronics, and robotics. Finally, graphene aerogel is used as fire resistant material, demonstrating unconventional resistance to flame with self-extinguishing properties up to 1500 °C. All these results show that high-quality graphene aerogels are a unique class of materials that can preserve some of the unique properties of graphene yet provide many new exciting possibilities for developing novel functional materials and devices.

Acknowledgment

I want to thank to the whole NMS group (Jiří, Ali, Kumar, Wahab) based at the FZU for good cooperation and help throughout the whole PhD studies. Our group leader Jiří Červenka was in fact my supervisor. Without his guidance and approach in leading the group, this thesis would not contain so many unique results. Zahid Ali Zafar, who started his PhD studies in the group at the same time as me, was always here to help. Prabhat Kumar, who joined the group at the end of 2019, was crazy enough to help me with number of experiments with graphene aerogels.

I would also like to thank to my official supervisor Antonín Fejfar for keeping the studies official, believing me, and leaving all the guidance of my PhD studies on my group leader Jiří.

I am also grateful to the rest of my colleagues from the department of Thin Films and Nanostructures. They wished to be enumerated :) : Martin Muller, Martin Ledinský, Aleš Vlk, Matěj Hývl, Pavla Bauerová, Martin Hladík and others. They were always here for scientific and mainly non-scientific discussions.

List of Figures

List of Tables

List of Acronyms

GA	Graphene aerogel prepared in this work
GO	Graphene oxide
SEM	Scanning electron microscopy
XPS	X-ray photoelectron spectroscopy
CVD	Chemical vapor deposition
FTIR	Fourier transform infrared spectroscopy
DLS	Dynamic light scattering
LFA	Laser flash analysis
TGA	Thermal gravimetric analysis
SOP	Standard operating procedure
rGA	Reduced graphene oxide aerogel
XRD	X-ray diffraction
aGO	Graphene oxide affected by ageing for 1 year
pGO	Plasma treated graphene oxide affected by ageing for 1 year
MOBM	Modular origami bending model
IPA	Isopropyl alcohol
DTGA	Differential thermal gravimetric analysis

Contents

1 Introduction

1.1 Introduction

Graphene is a two-dimensional material consisting of sp^2 hybridized carbon atoms, which are interconnected into a hexagonal honeycomb lattice.[1] It has been deeply studied by the scientific community since its discovery in 2004,[2] thanks to its incredible physical properties,[1] which can be used in practical applications such as transistors,[3] batteries,[4,5] sensors,[6,7] protective coatings,[8,9] and many others. These unique physical properties originate from graphene's atomic structure. The lattice structure of graphene has a hexagonal symmetry characterized by the D6h point group. The unit cell contains two carbon atoms. Each carbon atom has 6 electrons. The core orbital 1s contains 2 electrons, and the valence orbitals 2s and 2p contain 4 electrons. The electrons in the valence orbitals participate in the sp^2 hybridized carbon-carbon bonding. The hexagonal arrangement in the 2D plane allows forming 3 covalent σ bonds with 3 neighboring carbon atoms using the hybridized 2s orbital with two 2p orbitals. The last 1 electron in the third 2p orbital remains unchanged as a π orbital. The resulting sp^2 carbon-carbon bonds in graphene are stronger than in sp^3 hybridized diamond because the bonds are shorter and have more s orbital character. The π orbitals are responsible for the unique electronic properties of graphene. As the experimentally prepared graphene samples are not perfect, there is a huge variation in published results. The broad range of mechanical, electrical, and thermal properties of graphene materials originates from the crumpling, wrinkling, rippling, presence of defects (mainly point defects and single vacancy), dopants, adsorbates, the influence of substrate, or different preparation and measurement methods.[10–15]

Graphene possesses exceptional mechanical properties such as stiffness, strength, elasticity, and toughness. The mechanical properties of graphene are a direct result of the strong sp^2 carbon-carbon bonding. The Young's modulus of graphene measured using an atomic force microscope was reported in the range of hundreds GPa to 1 TPa.[16] The measurement of elastic behavior provided the intrinsic strength value in the range of 50-130 GPa at 10-25% of strain.[17] Graphene demonstrated elastic response even at the nonlinear part of the stress-strain curve. This elastic behavior is unique because usual materials such as steel are elastic only within the linear range of the stress-strain curve.

The electrical properties of graphene are influenced by the bonding and anti-bonding of π orbitals and benefit from the zero-overlap semimetal characteristics. Graphene exhibits electrical conductivity in the range of 10^5-10^6 $S.m^{-1}$, which was measured by the four-probe method or using conductive atomic force microscopy.[18–20] Additionally, the carrier mobility achieves over 20×10^4 $cm^2.V^{-1}.s^{-1}$.[21,22] As mentioned above, every imperfection in the atomic structure affects the physical properties of graphene. This fact is used in straintronics, where a stimulated deformation by mechanical strain leads to a reversible (only in the elastic region of deformation) change of graphene electrical properties.[23] Electrical properties of graphene can also be tuned using dopants, adsorbed molecules, liquids, etc.[24–26]

The thermal conductivity of graphene is also governed by the strong sp^2 covalent bonding. The thermal conductivity of graphene was determined using Raman spectroscopy, owing to the high sensitivity of the G band to the change of temperature.[27] Graphene exhibits a thermal conductivity in the range of 3000-5000 $W.m^{-1}.K^{-1}$.[28,29] The thermal conductivity of graphene is dominated by phonon transport,[30,31] and can be modified by doping, functionalization, etc.[32,33]

Despite its unique properties and possibility of real applications, graphene also has many disadvantages. Most of its properties stem from an ideal defect-free structure,[14] which is difficult to prepare cheaply in large quantities. The handling of atomically thin material is complicated and there is a risk of damaging it during manipulation or transfer from a substrate. For many applications, it would be desired to create a 3D structure from graphene that would be mechanically robust for manual handling and replicate the unique properties of graphene. An intuitive option is to add graphene as an additive to other bulk materials. Graphene additives have been shown to improve the properties of many materials,[34] but their mechanical strength and elasticity are still far from the values of graphene. Another way is to prepare 3D material directly from graphene layers. Graphite can be considered as one of many possible arrangements of 3D graphene structure. However, graphite has very strong anisotropy of the physical properties because of the weak van der Waals bonds between the individual layers and strong covalent sp^2 bonds in the plane of graphene.[35] Ideally, graphene layers in 3D structure should be connected by the same covalent bonds as in graphene, avoiding weak van der Waals bonding.

The main objective of this dissertation thesis is to explore novel possibilities for utilizing the extraordinary properties of graphene in 3D graphene structures (Figure 1.1). The thesis exploits the synthesis of free-standing graphene materials arranged into a

3D porous structure and investigates their mechanical, electrical, and fire-resistant properties. It shows that mechanically stable macroscopic graphene aerogels made of covalently cross-linked networks of graphene sheets can be experimentally prepared. Their properties preserve some of the characteristics of graphene, but they differ in some aspects significantly. The thesis summarizes the most important results of the experimental characterization of the graphene aerogels using mechanical and electrical testing, Raman spectroscopy, X-ray photoelectron spectroscopy (XPS) and Scanning electron microscopy (SEM). It also provides new insights into the fundamental understanding of the observed phenomena, particularly in the role of defects and impurities on the superelasticity and fire resistance of the materials. Moreover, it explores possible practical applications of the graphene aerogels in electromechanical sensors and fire resistant materials, providing new avenues for the development of novel devices in engineering, electronics, and biomedicine.

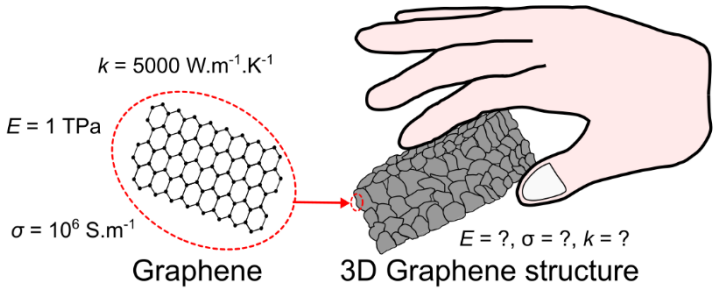

Figure 1.1 Schematic of a transformation of graphene into a mechanically robust 3D graphene structure with unknown mechanical (E), electrical (σ), and thermal (k) properties.

1.2 Synthesis of 3D graphene based structures

In recent years, several methods for 3D graphene structure synthesis have been reported.[36] These methods can be divided into two major groups: (i) templated synthesis and (ii) template-free methods. Each of the methods has its advantages and disadvantages, as described below. The as-prepared 3D graphene structures are called graphene aerogels if the liquid component of the gel is replaced with air. Other terms include graphene foams, sponges, or 3D graphene. Most of these methods start from solid or gas precursors. Graphene oxide (GO) has been the most used solid precursor for synthesizing 3D graphene structures.

1.2.1 Graphene oxide

Graphene oxide is an oxidized form of graphene containing various oxygen functional groups such as hydroxyl, carboxyl, and epoxy groups bonded all over the graphene plane.[37] This combination of different bonds leads to the mixture of sp^2 and sp^3 hybridized carbon atoms in GO. The oxygen groups additionally make GO hydrophilic,[38] which enables GO to be dispersed in water or polar solvents. The huge number of oxygen groups also acts as a potential place for the chemical functionalization of graphene. Except for all these properties, which are extremely important for the synthesis of 3D graphene structures, GO also possesses many other interesting properties. For example, GO can have good dielectric properties (depending on its structure and carbon to oxygen ratio), which can be used in memristors,[39] membrane gas or ion separation,[40] and sensors[41]. Most importantly, GO might be used as an intermediary in the large-scale production of graphene.[42]

The basic and most used strategy for synthesizing GO is the Hummers method, or nowadays the Tour's method.[43,44] These methods are based on the oxidative treatment of graphite. The Hummers method starts with a piece of graphite immersed into a mixture of potassium permanganate, sulfuric acid, and sodium nitrate.[43] The reaction takes place for 8-12 hours, and then the unreacted parts of the mixture are neutralized using a solution of H_2O_2.[43] The resulting GO has a C/O ratio of 2-3.[46] The disadvantage of this method is the creation of environmentally unfriendly NO_x molecules during the reaction. The Tour's method is presented as an eco-friendly modification of the Hummers method. In this process, the graphite is immersed in a mixture of potassium permanganate, sulfuric acid, and phosphoric acid, which is kept in an ice bath.[44] The reaction proceeds for 12 hours, while the mixture is stirred and kept at 50 °C.[45] The mixture is poured on ice, and the neutralization is done in the same way as in the Hummers method. The Tour's method is more yielding and environmental-friendly, producing GO with a lower C/O ratio than the Hummers method.[47]

The number and dimensions of GO layers and the ratio of carbon to oxygen along with the ratio of different oxygen groups are the main parameters monitored when using GO as the starting material in the synthesis of 3D graphene structures. The change in the composition of GO has been found to strongly affects the properties of the resulting 3D graphene structures.

1.2.2 Templated synthesis of 3D graphene structures

The templated synthesis methods are based on growing a material according to the pattern of a template. Once the structure is grown, the template is removed, and the structure is free-standing. Choosing and manufacturing the right template is a crucial part of the templated synthesis. There are either hard (metallic and polymeric foams or ice crystals) or soft (bubbles, organic droplets) templates, which are used in different template methods. The template methods can be divided into chemical vapor deposition (CVD), dip-coating,[48] and freeze-casting methods.[49] The common disadvantage of these methods is the need for the template, which can negatively affect the resulting structure and properties of the fabricated graphene materials.

Chemical vapor deposition

The CVD synthesis method is an analogy of graphene's most commonly used synthesis technique of graphene layers on surfaces, with the difference of using a porous substrate. The porous substrate serves as a template, which determines the structure and porosity of the resulting graphene foams.[50] The method utilizes catalytic metal, such as Ni or Cu, which allows controlling the number of graphene layers using the concentration of the carbon source. The first graphene foam synthesis was done by Chen et al.,[51] who used Ni foam as the template and CH_4 as the carbon precursor at 1000 °C. The as-prepared graphene foam followed exactly the structure of the Ni foam template, resulting in continuous graphene sheets over the whole surface of the template, without any aggregation.[51]

Generally, the CVD method produced graphene foams that have the most similar structural properties out of all 3D graphene structures to graphene.[52] On the other hand, the CVD processes are costly and require expensive equipment. Therefore, other templated methods, such as dip-coating (covering the substrate with GO/polymer suspension) and freeze-casting, are more favorable.

Freeze-casting method

The freeze-casting method is the most used fabrication method for 3D graphene structures out of the template synthesis group because of its simplicity. In this method, ice crystals act as the template and prevent the GO sheets from creating random

connections.[49] An aqueous GO suspension is frozen, and the phase separation between GO sheets and ice causes the GO sheets to be trapped between the growing ice crystals.[53] Once the sublimation of the ice happens, the porous structure is prepared. The shape of the porous structure can be tailored by controlling the directions of freeze-casting. Unfortunately, the number of graphene layers cannot be controlled using this method. This method can be further improved by introducing a second template in the form of air bubbles.[54] The air bubbles are created via mixing the GO suspension with a surfactant. The bubbles are isotropically distributed in the solution and let the GO sheets to self-assemble into a hydrogel. The self-assembled hydrogel can be dried using freeze-casting or other drying methods to create a graphene aerogel. Air bubbles cause circular holes into the ordered structure created via freeze-casting.[54]

1.2.3 Template-free methods

Without the presence of a template, a 3D graphene structure can be formed using various random self-assembly processes of GO sheets.[55] These methods are relatively cheap and allow controlling the density of the 3D structure via the concentration of GO in the suspension. The pore size can be affected by the temperature of freeze-drying. Reproducing the self-assembled structure can locally lead to some differences in properties, but overall properties remain the same throughout the whole material. In all these methods, the porous structure is random, and the number of graphene layers can be controlled only in a limited fashion.

Hydrothermal synthesis

The widely used method utilizing GO self-assembly is hydrothermal synthesis. This method is based on the self-assembly of GO layers at higher temperatures and pressure.[56] The process starts with a suspension of GO. In the suspension, individual layers of GO contain a lot of functional groups whose electrostatic repulsion is in balance with the van der Waals attraction.[57] The balance is broken by ultrasonication and the gelation begins. High temperature (around 200 °C) and high pressure are necessary to begin and control reduction processes, the gelling rate, and the integrality of the gel.[58] Once the hydrogel is formed, the drying technique (freeze or supercritical) is used to replace the solvent with air to create the graphene aerogel. This method is used for the synthesis of 3D graphene structures in this thesis (Chapter 3).

Chemical reduction

The chemical reduction uses the help of reducing agents such as ascorbic acid, hydrazine, $NaHSO_3$, ethylene diamine, and other acids or bases (H_2O_2).[59,60] These reduction agents are mixed with GO solution. Unlike the hydrothermal method, the reduction agents decrease the temperature and pressure necessary for the self-assembly of GO sheets into the hydrogel to temperatures below 100 °C and down to atmospheric pressure. The last step involving the transition of the hydrogel to aerogel is the same as for the hydrothermal methods. The as-prepared graphene aerogels are usually highly porous and possess low density.[61]

Cross-linking

The cross-linking method is introduced to improve the mechanical stability of the final graphene aerogel using various cross-linking agents.[62] These agents increase the strength of bonds between GO sheets in the process of gelation. The GO sheets are usually linked via hydrogen bonding, π-π and electrostatic interactions. The cross-linking agents are of 3 types: increasing hydrogen bonds (HCl), polymerizing (polyvinyl alcohol, formaldehyde, resorcinol), and ion linkings (Ca^{2+}, Mg^{2+}, Cr^{3+}, etc.).[63,64]

The GO suspensions are stable in water until the pH of the solution is decreased. Decreasing pH using hydrogen bonding or ion linking agents induces breaking of the GO sheets, weak electrostatic repulsion, and the bonding of hydrogen atoms into carboxyls.[65] This leads to an increase in hydrogen bonding between GO sheets or ion cross-linking of GO sheets.

The polymerization is caused by the combination of cross-linking agents, where the first agent reacts with the oxygen-containing groups of GO sheets. The second agent, usually polymer, creates a link between different GO sheets.[65] The metal ion acts as a link between GO sheets via the creation of a bond to the sheet. Once the GO suspension is prepared, the procedure is similar to the hydrothermal method.

These three methods are the same concerning the required laboratory equipment and differ only in the composition of GO suspensions. All of them allow tuning the density of the graphene aerogel via the concentration of GO in the suspension. Moreover, they enable the formation of different graphene aerogel shapes as the container used during the gel formation determines the final shape of the aerogel. The chemical reduction and

cross-linking methods introduce contamination into the final aerogel. Different additives can be used to increase the mechanical stability of graphene aerogel materials using this method. In contrast, graphene aerogels prepared via the hydrothermal method consist of only carbon and oxygen because only GO and solvent (mostly water) are used as precursors. If required, mechanical stability improvement can be made using post-synthesis treatments, such as thermal annealing.

3D printing

In recent years 3D printing technology has been adapted for many applications, including industrial material preparation. The crucial step for graphene aerogel preparation using 3D printing is the viscosity of the ink.[66] The ink is prepared from the usual GO solution mixed with additives such as polymers, SiO_2, $CaCl_2$, etc., which helps to achieve the desired viscosity.[67,68] This GO based ink is applied through the nozzle, and the printed structure is dried to form the aerogel.

This technique, unlike the previous template-free methods, allows controlling the morphology of the structure and large-scale production. On the other hand, the concentration of GO in the ink is fixed during the whole printing process. Therefore, there is no easy way to tune the final density of the materials. Moreover, the ink contains other elements. Thus, the graphene aerogel also contains other elements besides carbon and oxygen.

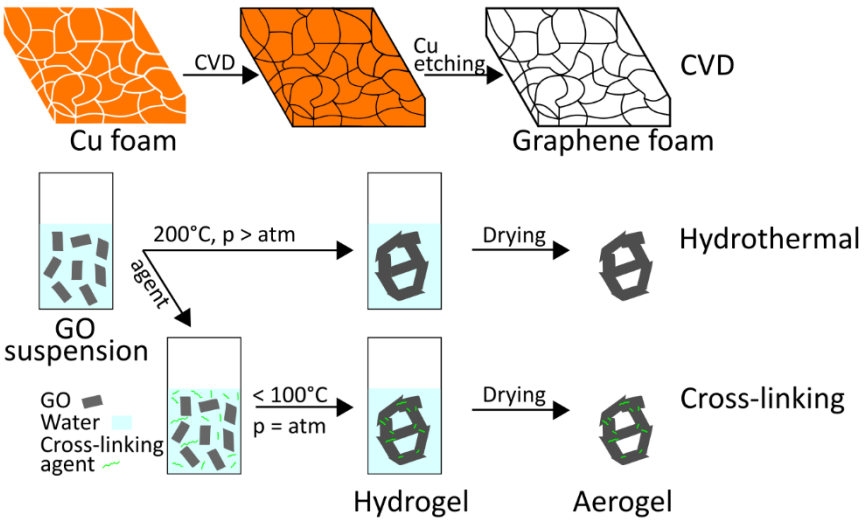

Figure 1.2 Schematic of 3D graphene structure synthesis. Chemical vapor deposition (CVD) and template-free methods (Hydrothermal and Cross-linking) using graphene oxide (GO) are shown.

1.3 Graphene aerogels

Aerogels are porous materials prepared by replacing the liquid component of a gel with gas without destroying their structure.[69] The porous structure is open with pores of dimensions in the range of 1 nm to 100 μm. Therefore, the aerogel contains, in terms of volume, more than 95% of air.[69] Due to a large amount of air in the structure, the aerogels reach extremely low densities, close to the air density (1.2 $mg.cm^{-3}$).[70] In addition to low density, aerogels also have extremely low thermal conductivity and a large specific surface area.[71]

Graphene aerogels have already been prepared by all the methods described above. The as-prepared graphene aerogels are open porous 3D materials exhibiting the following properties: large surface areas (> 1000 $m^2.g^{-1}$),[58] tunable porosity (from 1 nm to hundreds of μm),[62,72] ultralow densities (down to 0.16 $mg.cm^{-3}$),[73] extremely low thermal conductivity (< 4.7×10^{-3} $W.m^{-1}.K^{-1}$),[75] compressibility (> 99%),[74] and high electrical conductivity (900 $S.m^{-1}$).[49] The above-mentioned numbers in brackets represent the highest reported values for graphene aerogels in the literature up to now, but it is important to note that a single graphene aerogel sample has not been able to exhibit these properties all at once.

1.3.1 Mechanical properties

The mechanical properties of 3D graphene structures are dependent on the density, porosity, pore size, arrangement of graphene sheets, type and number of interconnections between graphene sheets, and the number of graphene layers.[76–80] These properties are defined during the synthesis. Therefore, the selection of the right preparation method is crucial for the resulting properties of the 3D graphene structures. The comparison of the reported compressive and tensile yield strength and corresponding strain and density within the different graphene and graphene composite aerogels, graphene foams, and other types of aerogels are shown in Table 1.1. Compressive and tensile yield strength is defined as the maximal stress at which the material is still elastic. Despite more than 10 years of studying graphene aerogels, the yield strength in compression has not yet been determined in these materials.[81] This might be because the usual hydraulic press can apply only pressures up to 1 GPa.[81] The mechanical testing showed a significant hysteresis in compression for many aerogels, revealing a parasitic non-elastic contribution to the elasticity in most of the materials.[82] Tensile testing has been successful only for CVD growth graphene foams, where the highest tensile strain of 17.5% at a stress

of 255 kPa has been reported for graphene foam prepared by CVD,[77] but the properties in compression are very poor.

So far, there is no report of tensile testing of pure graphene aerogel in the literature. This is because the tensile elasticity and strength of 3D graphene structures reported so far have been governed by the weak coupling of individual graphene sheets and a high number of defects in the materials.[58,83] Nevertheless, there are also reports in the literature promising exceptional tensile behavior of 3D graphene composites. But in these cases, the graphene is usually just an additive to rubbers that are originally highly stretchable. These composites show the maximum elongation of around tens of percent, with the exception of the multi-walled carbon nanotubes mixture with graphene aerogel.[84] This report shows 200% elongation, but the material withstands only 14% strain in compression. These results reveal that the preparation of highly elastic and strong 3D graphene structures that would sustain both high compressive and tensile strain is difficult.

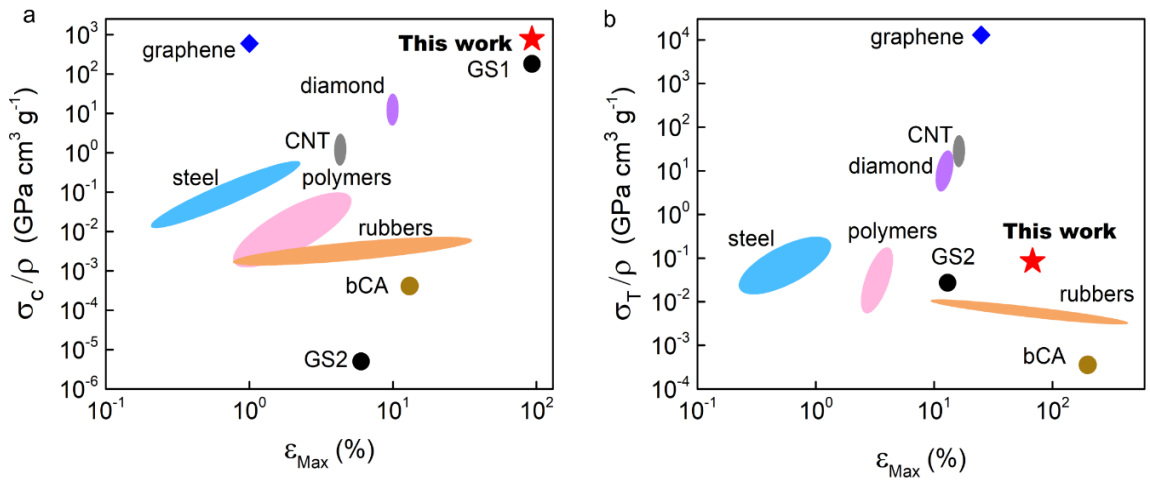

Figure 1.3 Mechanical properties of graphene aerogels. Comparison of compressive (a) and tensile (b) specific yield strength of different materials (graphene aerogels (GS1[81] GS2[77]), binary carbon aerogels (bCA[84]), graphene, diamond, carbon nanotube (CNT), stainless steel, polymers, and rubbers) as a function of the maximum elastic strain.

To compare the mechanical properties different graphene aerogels with well-known bulk materials, specific strength needs to be defined. The specific strength is the compressive and tensile yield strength related to the density. The results measured in this thesis (Chapter 4) with the maximum values of graphene aerogels/foams from the literature are

compared with those of steel, polymers, rubbers, and the highest reported values for graphene, diamond, and carbon nanotube. This comparison of specific strength is shown in Figure 1.3a,b as a function of the maximum elastic strain. The specific compressive strength of the graphene aerogel prepared in this thesis (GA) is comparable to that of graphene. However, the GA can be compressed up to more than 90% of strain, while graphene's elasticity ends at only 1% of strain. In tensile, the specific strength of the GA prepared in this thesis is similar to the stainless steel but has an order of magnitude larger elastic strain.

1.3.2 Electrical properties

The electrical conductivity of 3D graphene structures depends, similarly to graphene, on the quality of the material and, in addition, on the quality and type of interconnections among the individual graphene layers. A comparison of electrical conductivity of different 3D graphene structures is in Table 1.1. The least defective structure is graphene foam prepared by CVD methods.[85] On the contrary, graphene aerogels prepared from individual GO flakes are usually characterized by a huge number of defects and interconnections.[52] This is also reflected in the resulting electrical conductivity of the materials using these two methods. The high electrical conductivity of CVD graphene foams (up to 1000 $S.m^{-1}$) is related to the high temperature used in the growth because higher temperature allows the formation of higher crystallinity.[85] To achieve higher conductivity of graphene aerogels prepared from GO in this thesis, annealing at a high temperature was performed to remove defects and increase the crystallinity (Chapter 3). In addition, annealing can increase the number of bonds between the graphene layers, which also helps to increase electrical conductivity.[82] The dependence of electrical conductivity on the annealing temperature was measured for graphene aerogel prepared by chemical reduction.[58] The electrical conductivity was increased 5 times by increasing the annealing temperature from 1000 °C to 2500 °C.[58] Different reducing agents ($NaHSO_3$, Na_2S, HI, ascorbic acid, and hydroquinone) have been used in chemical reduction synthesis to investigate the effect on the electrical conductivity of as-prepared graphene aerogel.[86] It was found that using hydroiodic acid and $NaHSO_3$ leads to significantly higher values of electrical conductivity.[86]

Table 1.1 Mechanical and electrical properties of 3D graphene structures, where graphene aerogels were prepared via template-free methods and graphene foams via templated synthesis. Graphene-composite aerogel is a hybrid of graphene aerogel with other compounds.

		Mechanical				Electrical	
		Compression		Tension			
	Density ($mg.cm^{-3}$)	Stress (kPa)	Strain (%)	Stress (kPa)	Strain (%)	Conductivity ($S.m^{-1}$)	Ref.
Graphene aerogels	6-8	4 500 000	92	550	68		This work
	1.15	100	90	-	-	0.4	[87]
	8	700	99	-	-	100	[88]
	6	1000	99	-	-	130	[89]
	5.8	1 057 000	99.8	-	-	17	[81]
	123	1200	90	-	-	278	[90]
Graphene composite aerogels	5.7	2.5	14	2	200	1000	[84]
	2.32	94.5	50	-	-	11.7	[91]
	3	4.3	50	-	-	2.5	[92]
	6	5	50	-	-	16	[93]
	13.2	6	60	-	-	0.2	[94]
	5.8	10	95	-	-	34.8	[95]
	0.16	6	50	-	-	0.6	[73]
	92	231	99.6	-	-	-	[96]
	6.7	58	80	-	-	-	[74]
	14.1	25	80	-	-	6.7	[97]

Graphene foam	69.7	-	-	1190	4	-	[77]
	11	500	8	255	17.5	-	[77]
	5.1	-	-	-	-	1000	[85]
	5.1	18	80	-	-	12	[83]

1.3.3 Applications

As mentioned above, 3D graphene structures exhibit unique mechanical, thermal, and electrical properties, which can be used in a wide range of applications, such as piezoresistive sensors [98], thermal insulators [99], electrodes in batteries [100], and supercapacitors [101], absorption of pollutants [102] and so on.

Absorption of pollutants

Lack of drinking water threatens today's society with increasing environmental pollution. Various porous materials are already used as pollutant cleaners of water, where the main requirement is specific pore size. As mentioned, the pore size of graphene aerogels can vary from nm to hundreds of micrometers depending on the type of preparation. In addition, graphene aerogels are hydrophobic, which makes them suitable for absorbing oils from water.[103] Due to different pore sizes and hydrophobicity, graphene aerogels have been demonstrated to have a higher adsorption capacity compared to other types of absorbers.[104]

Energy storage

Efficient energy storage is one of the main challenges for today's society. Batteries and supercapacitors provide an attractive solution for energy storage. However, their efficiency and energy/power density needs to be significantly improved to compete with fossil fuels. The efficiency of batteries and supercapacitors relies mainly on the properties of the electrodes.[105] Electrodes should have a high surface area, high electrical conductivity, good mechanical stability, and low cost. In batteries, electrodes are the place where the intercalation/insertion or ion transfer processes can happen. To support these processes,

electrodes should be porous, elastic, and conductive. Graphene aerogels fulfill all of these basic requirements, so they are great candidates for the development of advanced electrodes in supercapacitors and batteries.

Sensors

The human-machine interface and skin monitoring are currently very important for extending the use of robots and sensors that monitor bodily functions. A highly sensitive sensor with a wide dynamic range is required for these applications. Human body activities manifest themselves in a wide range of pressures. Low pressures from 0.2 to 10 kPa are characteristic of a gentle wrist pulse, intraocular pressure, and finger pressure.[106,107] High pressures from 10 to 500 kPa for activities related to standing and sitting movements.[106,108,109] Despite great advances in materials research, a material with similar properties as found in biological tissues has not yet been achieved on a large scale.[110] Current tactile sensors only operate in a certain range of pressures, so they cannot detect the entire variety of human bodily actions.[111,112] More sensors are needed to detect all of them, which is highly impractical.

In recent years, 3D graphene structures have been tested for tactile sensor applications due to their good electrical conductivity and piezoresistivity under compression.[111,113–115] A comparison of the response time and the maximum detectable pressure of various sensors is shown in Figure 1.4. The response time of the sensor studied in this thesis (Chapter 5) is demonstrated to be several orders of magnitude faster than the other sensors based on 3D graphene structures reported so far.[113,116,117] Moreover, the response time is even faster than sensors working on the base of other materials such as composites of CNT,[118,119] metal nanoparticles,[120,121] graphene transferred on polymer,[122,123] or porous sponges.[124,125] The GA sensors react faster and in a wider pressure range than other previously reported sensors. The only comparable sensor in terms of the response time is a laser-scribed graphene aerogel,[126] which provides fast response only at pressures in the range of 50-113 kPa.

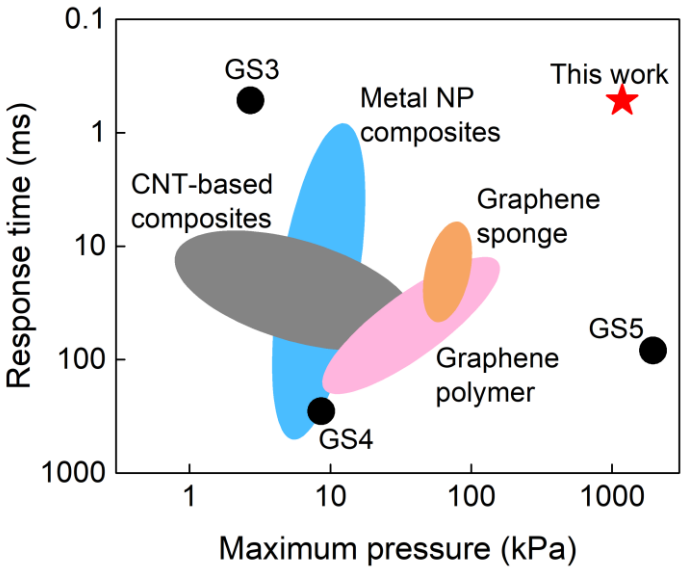

Figure 1.4 The response time of graphene aerogel strain sensors. Comparison of the response time and maximum pressure limit of the graphene aerogel sensors with different strain sensors based on graphene aerogel (GS3[113], GS4[117], GS5[116]), carbon nanotube (CNT), and other materials.

A comparison of different characteristics of pressure sensors based on 3D graphene structures is given in Table 1.2. The gauge factor is defined as the ratio of relative electrical resistance change ($\Delta R/R_0$) to mechanical strain (ε), and the sensitivity is the ratio of relative current change ($\Delta I/I_0$) to applied pressure difference (ΔP). If there are multiple numbers in the column gauge factor or sensitivity, it means a bilinear response of a sensor. It is shown that the sensor reported in this thesis (Chapter 5) is better in all characteristics than all the other 3D graphene based sensors, except for the CVD grown graphene foam strengthened with PDMS.[116] This sensor is comparable in terms of the gauge factor and the range of detectable pressures. However, our sensor has the possibility of sensing in compressive (up to 1.18 MPa) as well as tensile (0.55 MPa) regimes within a single sensor and incredibly high sensitivity in both regimes.

Table 1.2 Comparison of graphene aerogel sensors with other reported strain-gauge sensors based on graphene aerogels. Graphene-composite aerogel is a hybrid of graphene aerogel with other compounds. The range of strain and pressure, where the Gauge factor and Sensitivity are applied, is mentioned in brackets.

	Sensing type	Gauge factor	Sensitivity (kPa^{-1})	Response time (ms)	Ref.
Graphene aerogels	Compression	11.6 (0-10%) 0.38 (10-80%)	53500 (0-8 kPa) 12200 (0.008-1.18 MPa)	0.52	This work
	Tension	0.6 (0-35%) 3.4 (35-70%)	390 (0-0.3 MPa) 1085 (0.3-0.55 MPa)	-	
	Compression	1.3	-	-	[127]
	Compression	1.6 (60%)	-	250	[117]
	Compression	-	22.8	-	[128]
	Compression	1 (0-50%)	-	-	[90]
	Compression	1.34 (0-20%)	-	-	[129]
	Compression	-	0.96 (0-50 kPa) 0.005 (50-113 kPa)	212 0.4	[126]
Graphene composite aerogels	Compression	-	229.8 (0-0.1 kPa) 26.7 (0.4-1kPa)	-	[130]
	Compression	-	1.75	< 750	[131]
	Compression	2.6 (0-18%) 8.5 (22-40%)	0.09 (0-2 MPa)	80	[116]
	Compression	-	0.26 (0-2kPa) 0.03 (2-10kPa)	-	[132]
	Compression	-	3.08	14	[125]
	Compression	-	1.04 (13-260Pa) 0.12 (0.26-20kPa)	34	[133]

References

1. Novoselov, K. S. *et al.* Electric Field Effect in Atomically Thin Carbon Films. *Science* **306**, 666–669 (2004).
2. Tiwari, S. K., Sahoo, S., Wang, N. & Huczko, A. Graphene research and their outputs: Status and prospect. *Journal of Science: Advanced Materials and Devices* **5**, 10–29 (2020).

3. Schwierz, F. Graphene transistors. *Nature Nanotech* **5**, 487–496 (2010).
4. Zeng, M. *et al.* Metallic Cobalt Nanoparticles Encapsulated in Nitrogen-Enriched Graphene Shells: Its Bifunctional Electrocatalysis and Application in Zinc–Air Batteries. *Advanced Functional Materials* **26**, 4397–4404 (2016).
5. Yoo, E. & Zhou, H. Li−Air Rechargeable Battery Based on Metal-free Graphene Nanosheet Catalysts. *ACS Nano* **5**, 3020–3026 (2011).
6. Bae, S.-H. *et al.* Graphene-based transparent strain sensor. *Carbon* **51**, 236–242 (2013).
7. Lu, C.-C., Lin, Y.-C., Yeh, C.-H., Huang, J.-C. & Chiu, P.-W. High Mobility Flexible Graphene Field-Effect Transistors with Self-Healing Gate Dielectrics. *ACS Nano* **6**, 4469–4474 (2012).
8. Zhang, L. *et al.* Graphene enhanced anti-corrosion and biocompatibility of NiTi alloy. *NanoImpact* **7**, 7–14 (2017).
9. Yu, Z. *et al.* Fabrication of graphene oxide–alumina hybrids to reinforce the anti-corrosion performance of composite epoxy coatings. *Applied Surface Science* **351**, 986–996 (2015).
10. Li, Z. *et al.* Deformation of Wrinkled Graphene. *ACS Nano* **9**, 3917–3925 (2015).
11. Qin, H., Sun, Y., Liu, J. Z. & Liu, Y. Mechanical properties of wrinkled graphene generated by topological defects. *Carbon* **108**, 204–214 (2016).
12. Vicarelli, L., Heerema, S. J., Dekker, C. & Zandbergen, H. W. Controlling Defects in Graphene for Optimizing the Electrical Properties of Graphene Nanodevices. *ACS Nano* **9**, 3428–3435 (2015).
13. Salehi, M. *et al.* Low defect and high electrical conductivity of graphene through plasma graphene healing treatment monitored with in situ optical emission spectroscopy. *Sci Rep* **11**, 20334 (2021).
14. Li, M. *et al.* Effect of Defects on the Mechanical and Thermal Properties of Graphene. *Nanomaterials (Basel)* **9**, E347 (2019).
15. Malekpour, H. *et al.* Thermal conductivity of graphene with defects induced by electron beam irradiation. *Nanoscale* **8**, 14608–14616 (2016).
16. Lee, C., Wei, X., Kysar, J. W. & Hone, J. Measurement of the Elastic Properties and Intrinsic Strength of Monolayer Graphene. *Science* **321**, 385–388 (2008).
17. Cao, K. *et al.* Elastic straining of free-standing monolayer graphene. *Nature Communications* **11**, 284 (2020).

18. Lim, S., Park, H., Yamamoto, G., Lee, C. & Suk, J. W. Measurements of the Electrical Conductivity of Monolayer Graphene Flakes Using Conductive Atomic Force Microscopy. *Nanomaterials (Basel)* **11**, 2575 (2021).
19. Bøggild, P. *et al.* Mapping the electrical properties of large-area graphene. *2D Mater.* **4**, 042003 (2017).
20. Fang, X.-Y. *et al.* Temperature- and thickness-dependent electrical conductivity of few-layer graphene and graphene nanosheets. *Physics Letters A* **379**, 2245–2251 (2015).
21. Bolotin, K. I. *et al.* Ultrahigh electron mobility in suspended graphene. *Solid State Communications* **146**, 351–355 (2008).
22. Orlita, M. *et al.* Approaching the Dirac Point in High-Mobility Multilayer Epitaxial Graphene. *Phys. Rev. Lett.* **101**, 267601 (2008).
23. Bukharaev, A. A., Zvezdin, A. K., Pyatakov, A. P. & Fetisov, Y. K. Straintronics: a new trend in micro- and nanoelectronics and materials science. *Phys.-Usp.* **61**, 1175 (2018).
24. Singh, A. K. *et al.* Tailoring the Electrical Properties of Graphene Layers by Molecular Doping. *ACS Appl. Mater. Interfaces* **5**, 5276–5281 (2013).
25. Kim, Y.-J., Kim, Y., Novoselov, K. & Hong, B. H. Engineering electrical properties of graphene: chemical approaches. *2D Mater.* **2**, 042001 (2015).
26. Deka, M. J. & Chowdhury, D. Tuning Electrical Properties of Graphene with Different π-Stacking Organic Molecules. *J. Phys. Chem. C* **120**, 4121–4129 (2016).
27. Chen, S. *et al.* Raman Measurements of Thermal Transport in Suspended Monolayer Graphene of Variable Sizes in Vacuum and Gaseous Environments. *ACS Nano* **5**, 321–328 (2011).
28. Ghosh, S. *et al.* Extremely high thermal conductivity of graphene: Prospects for thermal management applications in nanoelectronic circuits. *Appl. Phys. Lett.* **92**, 151911 (2008).
29. Chen, S. *et al.* Thermal conductivity of isotopically modified graphene. *Nature Mater* **11**, 203–207 (2012).
30. Balandin, A. A. Thermal properties of graphene and nanostructured carbon materials. *Nature Mater* **10**, 569–581 (2011).
31. Jauregui, L. A. *et al.* Thermal Transport in Graphene Nanostructures: Experiments and Simulations. *ECS Trans.* **28**, 73 (2010).

32. Su, Z. *et al.* Enhanced thermal conductivity of functionalized-graphene/boron nitride flexible laminated composite adhesive via a facile latex approach. *Composites Part A: Applied Science and Manufacturing* **99**, 166–175 (2017).
33. Zhang, T., Li, J., Cao, Y., Zhu, L. & Chen, G. Tailoring thermal transport properties of graphene by nitrogen doping. *J Nanopart Res* **19**, 48 (2017).
34. Verma, D., Gope, P. C., Shandilya, A. & Gupta, A. Mechanical-Thermal-Electrical and Morphological Properties of Graphene Reinforced Polymer Composites: A Review. *Trans Indian Inst Met* **67**, 803–816 (2014).
35. Xiao, J. *et al.* Anisotropic friction behaviour of highly oriented pyrolytic graphite. *Carbon* **65**, 53–62 (2013).
36. Zhang, Y., Wan, Q. & Yang, N. Recent Advances of Porous Graphene: Synthesis, Functionalization, and Electrochemical Applications. *Small* **15**, 1903780 (2019).
37. Shin, D. S. *et al.* Distribution of oxygen functional groups of graphene oxide obtained from low-temperature atomic layer deposition of titanium oxide. *RSC Adv.* **7**, 13979–13984 (2017).
38. Wang, G. *et al.* Synthesis of enhanced hydrophilic and hydrophobic graphene oxide nanosheets by a solvothermal method. *Carbon* **47**, 68–72 (2009).
39. Sahu, D. P., Jetty, P. & Jammalamadaka, S. N. Graphene oxide based synaptic memristor device for neuromorphic computing. *Nanotechnology* **32**, 155701 (2021).
40. Unimpeded Permeation of Water Through Helium-Leak–Tight Graphene-Based Membranes. https://www.science.org/doi/10.1126/science.1211694.
41. Imamura, G. *et al.* Graphene Oxide as a Sensing Material for Gas Detection Based on Nanomechanical Sensors in the Static Mode. *Chemosensors* **8**, 82 (2020).
42. Zhu, Y. *et al.* Graphene and Graphene Oxide: Synthesis, Properties, and Applications. *Advanced Materials* **22**, 3906–3924 (2010).
43. Hummers, W. S. & Offeman, R. E. Preparation of Graphitic Oxide. *J. Am. Chem. Soc.* **80**, 1339–1339 (1958).
44. Marcano, D. C. *et al.* Improved Synthesis of Graphene Oxide. *ACS Nano* **4**, 4806–4814 (2010).
45. Jiříčková, A., Jankovský, O., Sofer, Z. & Sedmidubský, D. Synthesis and Applications of Graphene Oxide. *Materials (Basel)* **15**, 920 (2022).
46. P. Araújo, M., P. Soares, O. S. G., S. Fernandes, A. J., R. Pereira, M. F. & Freire, C. Tuning the surface chemistry of graphene flakes: new strategies for selective oxidation. *RSC Advances* **7**, 14290–14301 (2017).

47. Habte, A. T. & Ayele, D. W. Synthesis and Characterization of Reduced Graphene Oxide (rGO) Started from Graphene Oxide (GO) Using the Tour Method with Different Parameters. *Advances in Materials Science and Engineering* **2019**, e5058163 (2019).
48. Samad, Y. A., Li, Y., Schiffer, A., Alhassan, S. M. & Liao, K. Graphene Foam Developed with a Novel Two-Step Technique for Low and High Strains and Pressure-Sensing Applications. *Small* **11**, 2380–2385 (2015).
49. Lin, Y. *et al.* Pristine Graphene Aerogels by Room-Temperature Freeze Gelation. *Advanced Materials* **28**, 7993–8000 (2016).
50. Huang, M. *et al.* CVD Growth of Porous Graphene Foam in Film Form. *Matter* **3**, 487–497 (2020).
51. Chen, C.-M. *et al.* Macroporous 'bubble' graphene film via template-directed ordered-assembly for high rate supercapacitors. *Chem. Commun.* **48**, 7149–7151 (2012).
52. Gorgolis, G. & Galiotis, C. Graphene aerogels: a review. *2D Mater.* **4**, 032001 (2017).
53. Ouyang, A. *et al.* Polymer-Coated Graphene Aerogel Beads and Supercapacitor Application. *ACS Appl. Mater. Interfaces* **8**, 11179–11187 (2016).
54. Zhang, R. *et al.* A Bubble-Derived Strategy to Prepare Multiple Graphene-Based Porous Materials. *Advanced Functional Materials* **28**, 1705879 (2018).
55. Mohd Firdaus, R., Berrada, N., Desforges, A., Mohamed, A. R. & Vigolo, B. From 2D Graphene Nanosheets to 3D Graphene-based Macrostructures. *Chemistry – An Asian Journal* **15**, 2902–2924 (2020).
56. Xu, Y., Sheng, K., Li, C. & Shi, G. Self-Assembled Graphene Hydrogel via a One-Step Hydrothermal Process. *ACS Nano* **4**, 4324–4330 (2010).
57. Bourlinos, A. B. *et al.* Synthesis, characterization and gas sorption properties of a molecularly-derived graphite oxide-like foam. *Carbon* **45**, 852–857 (2007).
58. Worsley, M. A. *et al.* Synthesis and Characterization of Highly Crystalline Graphene Aerogels. *ACS Nano* **8**, 11013–11022 (2014).
59. Zhang, X. *et al.* Mechanically strong and highly conductive graphene aerogel and its use as electrodes for electrochemical power sources. *J. Mater. Chem.* **21**, 6494–6497 (2011).
60. Worsley, M. A. *et al.* Mechanically robust 3D graphene macroassembly with high surface area. *Chem. Commun.* **48**, 8428–8430 (2012).
61. Zhang, L., Chen, G., Hedhili, M. N., Zhang, H. & Wang, P. Three-dimensional assemblies of graphene prepared by a novel chemical reduction-induced self-assembly method. *Nanoscale* **4**, 7038–7045 (2012).

62. Worsley, M. A. *et al.* Synthesis of Graphene Aerogel with High Electrical Conductivity. *J. Am. Chem. Soc.* **132**, 14067–14069 (2010).
63. Li, Y., Sun, J., Wang, J., Qin, C. & Dai, L. Preparation of well-dispersed reduced graphene oxide and its mechanical reinforcement in polyvinyl alcohol fibre. *Polymer International* **65**, 1054–1062 (2016).
64. Jiang, X., Ma, Y., Li, J., Fan, Q. & Huang, W. Self-Assembly of Reduced Graphene Oxide into Three-Dimensional Architecture by Divalent Ion Linkage. *J. Phys. Chem. C* **114**, 22462–22465 (2010).
65. Bai, H., Li, C., Wang, X. & Shi, G. On the Gelation of Graphene Oxide. *J. Phys. Chem. C* **115**, 5545–5551 (2011).
66. Guo, H., Lv, R. & Bai, S. Recent advances on 3D printing graphene-based composites. *Nano Materials Science* **1**, 101–115 (2019).
67. Jiang, Y. *et al.* Direct 3D Printing of Ultralight Graphene Oxide Aerogel Microlattices. *Advanced Functional Materials* **28**, 1707024 (2018).
68. Yang, Z., Chabi, S., Xia, Y. & Zhu, Y. Preparation of 3D graphene-based architectures and their applications in supercapacitors. *Progress in Natural Science: Materials International* **25**, 554–562 (2015).
69. Pierre, A. C. & Pajonk, G. M. Chemistry of Aerogels and Their Applications. *Chem. Rev.* **102**, 4243–4266 (2002).
70. Madec, T. *et al.* Determination of the density of air: a comparison of the CIPM thermodynamic formula and the gravimetric method. *Metrologia* **44**, 441–447 (2007).
71. Kong, Y., Zhang, J., Zhao, Z., Jiang, X. & Shen, X. Monolithic silicon nitride-based aerogels with large specific surface area and low thermal conductivity. *Ceramics International* **45**, 16331–16337 (2019).
72. Bi, H. *et al.* Spongy Graphene as a Highly Efficient and Recyclable Sorbent for Oils and Organic Solvents. *Advanced Functional Materials* **22**, 4421–4425 (2012).
73. Sun, H., Xu, Z. & Gao, C. Multifunctional, Ultra-Flyweight, Synergistically Assembled Carbon Aerogels. *Advanced Materials* **25**, 2554–2560 (2013).
74. Lu, H., Li, C., Zhang, B., Qiao, X. & Liu, C.-Y. Toward highly compressible graphene aerogels of enhanced mechanical performance with polymer. *RSC Adv.* **6**, 43007–43015 (2016).
75. Xie, Y. *et al.* Interface-mediated extremely low thermal conductivity of graphene aerogel. *Carbon* **98**, 381–390 (2016).

76. Shen, Z., Ye, H., Zhou, C., Kröger, M. & Li, Y. Size of graphene sheets determines the structural and mechanical properties of 3D graphene foams. *Nanotechnology* **29**, 104001 (2018).
77. Kashani, H., Ito, Y., Han, J., Liu, P. & Chen, M. Extraordinary tensile strength and ductility of scalable nanoporous graphene. *Science Advances* **5**, eaat6951 (2019).
78. Cheraghi Bidsorkhi, H. *et al.* 3D Porous Graphene Based Aerogel for Electromagnetic Applications. *Sci Rep* **9**, 15719 (2019).
79. Yocham, K. M. *et al.* Mechanical Properties of Graphene Foam and Graphene Foam - Tissue Composites. *Adv Eng Mater* **20**, (2018).
80. Carvalho, A. F., Kulyk, B., Fernandes, A. J. S., Fortunato, E. & Costa, F. M. A Review on the Applications of Graphene in Mechanical Transduction. *Advanced Materials* **34**, 2101326 (2022).
81. Li, C., Ding, M., Zhang, B., Qiao, X. & Liu, C.-Y. Graphene aerogels that withstand extreme compressive stress and strain. *Nanoscale* **10**, 18291–18299 (2018).
82. Cheng, Y. *et al.* Enhanced mechanical, thermal, and electric properties of graphene aerogels via supercritical ethanol drying and high-temperature thermal reduction. *Sci Rep* **7**, 1439 (2017).
83. Qiu, L., Liu, J. Z., Chang, S. L. Y., Wu, Y. & Li, D. Biomimetic superelastic graphene-based cellular monoliths. *Nature Communications* **3**, 1241 (2012).
84. Guo, F. *et al.* Highly stretchable carbon aerogels. *Nature Communications* **9**, 881 (2018).
85. Chen, Z. *et al.* Three-dimensional flexible and conductive interconnected graphene networks grown by chemical vapour deposition. *Nature Materials* **10**, 424–428 (2011).
86. Chen, W. & Yan, L. In situ self-assembly of mild chemical reduction graphene for three-dimensional architectures. *Nanoscale* **3**, 3132–3137 (2011).
87. Wu, Y. *et al.* Three-dimensionally bonded spongy graphene material with super compressive elasticity and near-zero Poisson's ratio. *Nature Communications* **6**, 6141 (2015).
88. Zhang, Q. *et al.* Hyperbolically Patterned 3D Graphene Metamaterial with Negative Poisson's Ratio and Superelasticity. *Advanced Materials* **28**, 2229–2237 (2016).
89. Xu, X. *et al.* Naturally Dried Graphene Aerogels with Superelasticity and Tunable Poisson's Ratio. *Advanced Materials* **28**, 9223–9230 (2016).
90. Zhu, C. *et al.* Highly compressible 3D periodic graphene aerogel microlattices. *Nature Communications* **6**, 6962 (2015).

91. Moon, I. K., Yoon, S., Chun, K.-Y. & Oh, J. Highly Elastic and Conductive N-Doped Monolithic Graphene Aerogels for Multifunctional Applications. *Advanced Functional Materials* **25**, 6976–6984 (2015).
92. Hu, H., Zhao, Z., Wan, W., Gogotsi, Y. & Qiu, J. Ultralight and Highly Compressible Graphene Aerogels. *Advanced Materials* **25**, 2219–2223 (2013).
93. Liu, X. *et al.* Electro-active shape memory composites enhanced by flexible carbon nanotube/graphene aerogels. *J. Mater. Chem. A* **3**, 11641–11649 (2015).
94. Yao, B., Chen, J., Huang, L., Zhou, Q. & Shi, G. Base-Induced Liquid Crystals of Graphene Oxide for Preparing Elastic Graphene Foams with Long-Range Ordered Microstructures. *Advanced Materials* **28**, 1623–1629 (2016).
95. Xu, X. *et al.* Self-Sensing, Ultralight, and Conductive 3D Graphene/Iron Oxide Aerogel Elastomer Deformable in a Magnetic Field. *ACS Nano* **9**, 3969–3977 (2015).
96. Ye, S., Feng, J. & Wu, P. Highly elastic graphene oxide–epoxy composite aerogels via simple freeze-drying and subsequent routine curing. *J. Mater. Chem. A* **1**, 3495–3502 (2013).
97. Gao, H.-L. *et al.* Super-elastic and fatigue resistant carbon material with lamellar multi-arch microstructure. *Nature Communications* **7**, 12920 (2016).
98. Li, G. *et al.* A Wide-Range Linear and Stable Piezoresistive Sensor Based on Methylcellulose-Reinforced, Lamellar, and Wrinkled Graphene Aerogels. *Advanced Materials Technologies* **7**, 2101021 (2022).
99. Zhang, Q. *et al.* Mechanically robust honeycomb graphene aerogel multifunctional polymer composites. *Carbon* **93**, 659–670 (2015).
100. Nitze, F., Agostini, M., Lundin, F., Palmqvist, A. E. C. & Matic, A. A binder-free sulfur/reduced graphene oxide aerogel as high performance electrode materials for lithium sulfur batteries. *Sci Rep* **6**, 39615 (2016).
101. Chen, P. *et al.* Hydrothermal synthesis of macroscopic nitrogen-doped graphene hydrogels for ultrafast supercapacitor. *Nano Energy* **2**, 249–256 (2013).
102. Li, J. *et al.* Ultra-light, compressible and fire-resistant graphene aerogel as a highly efficient and recyclable absorbent for organic liquids. *J. Mater. Chem. A* **2**, 2934–2941 (2014).
103. Wang, S., Zhang, Y., Abidi, N. & Cabrales, L. Wettability and Surface Free Energy of Graphene Films. *Langmuir* **25**, 11078–11081 (2009).
104. Xu, L. *et al.* Superhydrophobic and superoleophilic graphene aerogel prepared by facile chemical reduction. *J. Mater. Chem. A* **3**, 7498–7504 (2015).

105. M., A. & Paul, A. Importance of Electrode Preparation Methodologies in Supercapacitor Applications. *ACS Omega* **2**, 8039–8050 (2017).
106. Trung, T. Q. & Lee, N.-E. Flexible and Stretchable Physical Sensor Integrated Platforms for Wearable Human-Activity Monitoringand Personal Healthcare. *Advanced Materials* **28**, 4338–4372 (2016).
107. Kang, D. *et al.* Ultrasensitive mechanical crack-based sensor inspired by the spider sensory system. *Nature* **516**, 222–226 (2014).
108. Wang, X., Gu, Y., Xiong, Z., Cui, Z. & Zhang, T. Silk-Molded Flexible, Ultrasensitive, and Highly Stable Electronic Skin for Monitoring Human Physiological Signals. *Advanced Materials* **26**, 1336–1342 (2014).
109. Kenry, Yeo, J. C. & Lim, C. T. Emerging flexible and wearable physical sensing platforms for healthcare and biomedical applications. *Microsyst Nanoeng* **2**, 1–19 (2016).
110. Vatankhah-Varnosfaderani, M. *et al.* Mimicking biological stress–strain behaviour with synthetic elastomers. *Nature* **549**, 497–501 (2017).
111. Chen, S., Jiang, K., Lou, Z., Chen, D. & Shen, G. Recent Developments in Graphene-Based Tactile Sensors and E-Skins. *Advanced Materials Technologies* **3**, 1700248 (2018).
112. Yu, J., Zhang, K. & Deng, Y. Recent progress in pressure and temperature tactile sensors: principle, classification, integration and outlook. *Soft Science* **1**, 6 (2021).
113. Qiu, L. *et al.* Ultrafast Dynamic Piezoresistive Response of Graphene-Based Cellular Elastomers. *Advanced Materials* **28**, 194–200 (2016).
114. Yang, M. *et al.* Biomimetic Architectured Graphene Aerogel with Exceptional Strength and Resilience. *ACS Nano* **11**, 6817–6824 (2017).
115. Jeong, Y. R. *et al.* Highly Stretchable and Sensitive Strain Sensors Using Fragmentized Graphene Foam. *Advanced Functional Materials* **25**, 4228–4236 (2015).
116. Pang, Y. *et al.* Flexible, Highly Sensitive, and Wearable Pressure and Strain Sensors with Graphene Porous Network Structure. *ACS Appl Mater Interfaces* **8**, 26458–26462 (2016).
117. Hu, K., Szkopek, T. & Cerruti, M. Tuning the aggregation of graphene oxide dispersions to synthesize elastic, low density graphene aerogels. *J. Mater. Chem. A* **5**, 23123–23130 (2017).

118. Park, J. *et al.* Giant Tunneling Piezoresistance of Composite Elastomers with Interlocked Microdome Arrays for Ultrasensitive and Multimodal Electronic Skins. *ACS Nano* **8**, 4689–4697 (2014).
119. Liu, M. *et al.* Large-Area All-Textile Pressure Sensors for Monitoring Human Motion and Physiological Signals. *Advanced Materials* **29**, 1703700 (2017).
120. Lee, J. *et al.* Conductive Fiber-Based Ultrasensitive Textile Pressure Sensor for Wearable Electronics. *Advanced Materials* **27**, 2433–2439 (2015).
121. Wu, Y. *et al.* Channel Crack-Designed Gold@PU Sponge for Highly Elastic Piezoresistive Sensor with Excellent Detectability. *ACS Appl. Mater. Interfaces* **9**, 20098–20105 (2017).
122. Pang, Y. *et al.* Epidermis Microstructure Inspired Graphene Pressure Sensor with Random Distributed Spinosum for High Sensitivity and Large Linearity. *ACS Nano* **12**, 2346–2354 (2018).
123. Liu, W. *et al.* Piezoresistive Pressure Sensor Based on Synergistical Innerconnect Polyvinyl Alcohol Nanowires/Wrinkled Graphene Film. *Small* **14**, 1704149 (2018).
124. Dong, X. *et al.* A linear and large-range pressure sensor based on a graphene/silver nanowires nanobiocomposites network and a hierarchical structural sponge. *Composites Science and Technology* **155**, 108–116 (2018).
125. Luo, Y., Xiao, Q. & Li, B. Highly compressible graphene/polyurethane sponge with linear and dynamic piezoresistive behavior. *RSC Adv.* **7**, 34939–34944 (2017).
126. Tian, H. *et al.* A Graphene-Based Resistive Pressure Sensor with Record-High Sensitivity in a Wide Pressure Range. *Scientific Reports* **5**, 8603 (2015).
127. Kuang, J. *et al.* A hierarchically structured graphene foam and its potential as a large-scale strain-gauge sensor. *Nanoscale* **5**, 12171–12177 (2013).
128. Zang, X. *et al.* Unprecedented sensitivity towards pressure enabled by graphene foam. *Nanoscale* **9**, 19346–19352 (2017).
129. Zhang, Q. *et al.* 3D Printing of Graphene Aerogels. *Small* **12**, 1702–1708 (2016).
130. Lv, L., Zhang, P., Xu, T. & Qu, L. Ultrasensitive Pressure Sensor Based on an Ultralight Sparkling Graphene Block. *ACS Appl. Mater. Interfaces* **9**, 22885–22892 (2017).
131. Ma, Z. *et al.* Lightweight, compressible and electrically conductive polyurethane sponges coated with synergistic multiwalled carbon nanotubes and graphene for piezoresistive sensors. *Nanoscale* **10**, 7116–7126 (2018).

132. Yao, H.-B. *et al.* A Flexible and Highly Pressure-Sensitive Graphene–Polyurethane Sponge Based on Fractured Microstructure Design. *Advanced Materials* **25**, 6692–6698 (2013).
133. Chun, S., Hong, A., Choi, Y., Ha, C. & Park, W. A tactile sensor using a conductive graphene-sponge composite. *Nanoscale* **8**, 9185–9192 (2016).

2 Methods

2.1 Characterization techniques

2.1.1 Scanning electron microscopy

Electron microscopy is an imaging technique for visualizing objects which are too small for optical microscopy. The resolution of the microscopy can be expressed using the Rayleigh criterion for circular aperture, which defines the minimum distance of two points (d_{min}) which diffraction patterns are distinguishable from each other when it is observed by an objective having a particular numerical aperture (*NA*):

$$d_{min} = \frac{0.61\lambda}{NA},$$

where λ is the wavelength of used light.[1] For optical microscopy, the wavelength is roughly 250 nm, but for electron microscopy, the theoretical limit is in the range of pm. There are two types of microscopes which differ in the way the signal is received. A SEM is based on the reflected signal, while a transmission electron microscope analyzes the electrons after passing through the sample. The interaction of the electron beam with the sample usually induces signals used in SEM electron signals (Auger, secondary, and backscattered) and other radiation (characteristic and continuum X-ray and cathodoluminescence).

In this study, the micrography was carried out using a TESCAN MAIA3 system in which the secondary electrons signal was the only signal used for images. Secondary electrons are a product of inelastic interaction between the primary electron beam and the sample. Secondary electrons are generated from the surface or the near-surface regions (maximum tens of nm deep) of the sample. Therefore, they are a useful tool for describing the surface topography of the sample. The in-situ GA compression experiment was performed by using a nano manipulator (Kleindiek MMA3A-EM) inside the SEM setup.

2.1.2 X-ray photoelectron spectroscopy

X-ray photoelectron spectroscopy is a surface-sensitive, non-destructive characterization technique. It provides qualitative as well as quantitative information about the chemical

composition and electrical structure of the sample surface. The XPS is an application of the photoelectric effect, which is based on photoelectrons emitted by the sample as a response to incidental radiation. The sample is illuminated by X-ray radiation, and photoelectrons produced by the sample are detected as a function of energy.

Photoelectrons (E_{kin}) are produced only if the incident energy ($h\nu$) exceeds the binding energy (E_b) of electrons in the material (Figure 2.1).[2] The mean free path of electrons is small, therefore, the sample information comes from a maximum depth of 10 nm. The kinetic energy of photoelectrons is related to the binding energy of each electron. The resulting response in the form of emitted electrons has different binding energies (and kinetic energies) because the kinetic energy of the emitted electrons is related to the binding energy of each electron and the atom has multiple paths of different energy states. This can be written as the following equation:

$$E_{kin} = h\nu - E_b - \Phi,$$

where Φ is the work function. The work function is the energy difference between the Fermi level and the vacuum energy of a solid.[2] The quantity of a specific element within the irradiated area is directly proportional to the number of electrons detected at the energy, which is characteristic of the element.

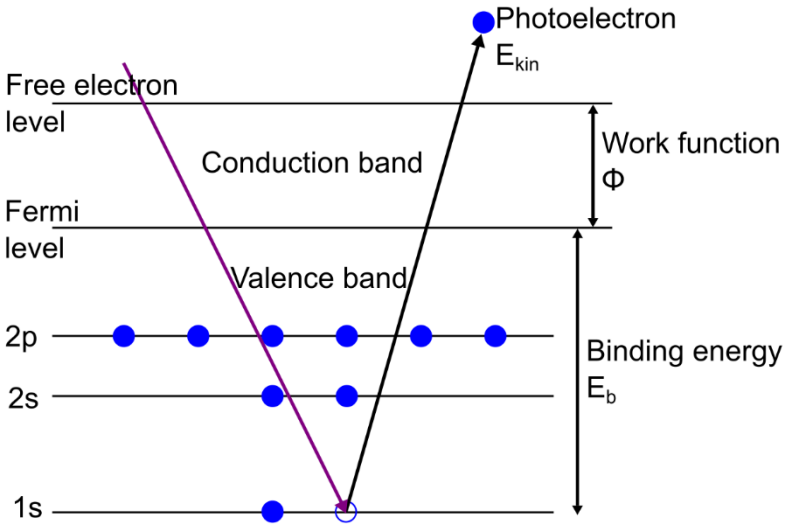

Figure 2.1 X-ray photoelectron spectroscopy. The principle of photoelectron emission.

2.1.3 Raman spectroscopy

The Raman scattering is an inelastic part of the scattering of photons (Figure 2.2a). The inelasticity lies in the different frequency (energy) of the scattered photon from the incident photon. The incident photon excites the molecule into the virtual energy state. The photon is emitted and the molecule relaxes to the higher (Stokes shift) or lower (anti-Stokes shift) energy state than the original energy state of the molecule.[3] The intensity of the Stokes part is proportional to the number of atoms in the ground state, whereas the intensity of the anti-Stokes part is proportional to the number of atoms in the excited state.[4] The specimen usually has more atoms in the ground state than in the excited states; therefore, the Stoke part is more intense than the anti-Stokes part.

Raman spectroscopy is the optical characterization technique used to find the molecular composition and molecular structure of the specimen. The Raman spectroscopy is based on analyzing the Raman scattering. The spontaneous Raman scattering is typically very weak; therefore, the sample needs to be illuminated with a source of monochromatic light, typically a laser with a wavelength in the visible, near IR, or UV range. The wavelength of the laser is chosen with respect to the relation of the intensity of the Raman scattering to λ^{-4} and that the light is not absorbed by the sample.[4] The elastically scattered radiation is filtered out and the inelastic scattering is captured on a detector. The spectrum of the signal from the detector is displayed as an intensity dependence on Raman shift $\Delta\omega$:

$$\Delta\omega = \frac{1}{\lambda_0} - \frac{1}{\lambda_1},$$

where λ_0 is the wavelength of the excitation laser and λ_1 is the wavelength of the scattered radiation.[3] The Raman shift depends on the temperature; thus the intensity of the excitation laser needs to be controlled.

Raman spectroscopy is a very important tool for graphene characterization. The number of layers, structural damage, chemical modifications, and functional groups can be determined by this measurement. However, in graphene aerogels, the Raman spectroscopy does not identify the number of layers due to the random orientation of graphene flakes. The typical Raman spectrum of graphene consists of 3 Raman modes G, D, and 2D.[5] The G band originates from a first-order Raman scattering process. The D with 2D modes are based on a second-order Raman process in graphene (Figure 2.2b,c,d). The Raman signal for the G band comes from the generation of in-plane transversal (iTO) and longitudinal (LO) optical phonon dispersion at the Brillouin zone caused by in-plane C-C bond stretching (sp^2).[6] This band is sensitive to in-plane

stretching, confirming sp^2 hybridization.[6] Unlike the other bands, the G-band is a single-order process in graphene. The D mode arises from a second-order process that involves iTO and one defect near the K point.[7] The need for a defect indicates a disorder in the sp^2 system.[7] The presence of D mode in Raman spectra is proof of a defect in structure. The ratio of the G and D band intensities (I_D/I_G) is used for the characterization of defect concentration. The 2D mode is associated with a second-order process involving two iTO phonons. Therefore, it is much dependent on two-dimensionality without a need of defect.[5] This mode is used for distinguishing the number of layers in graphene using the ratio of G and 2D band intensities (I_{2D}/I_G). The higher the ratio the fewer layers of graphene (~ 2 for a single layer).[7] In this thesis, The Raman spectroscopy was performed using a Raman system (Renishaw inVia Reflex) with HeCd laser (λ = 442 nm).

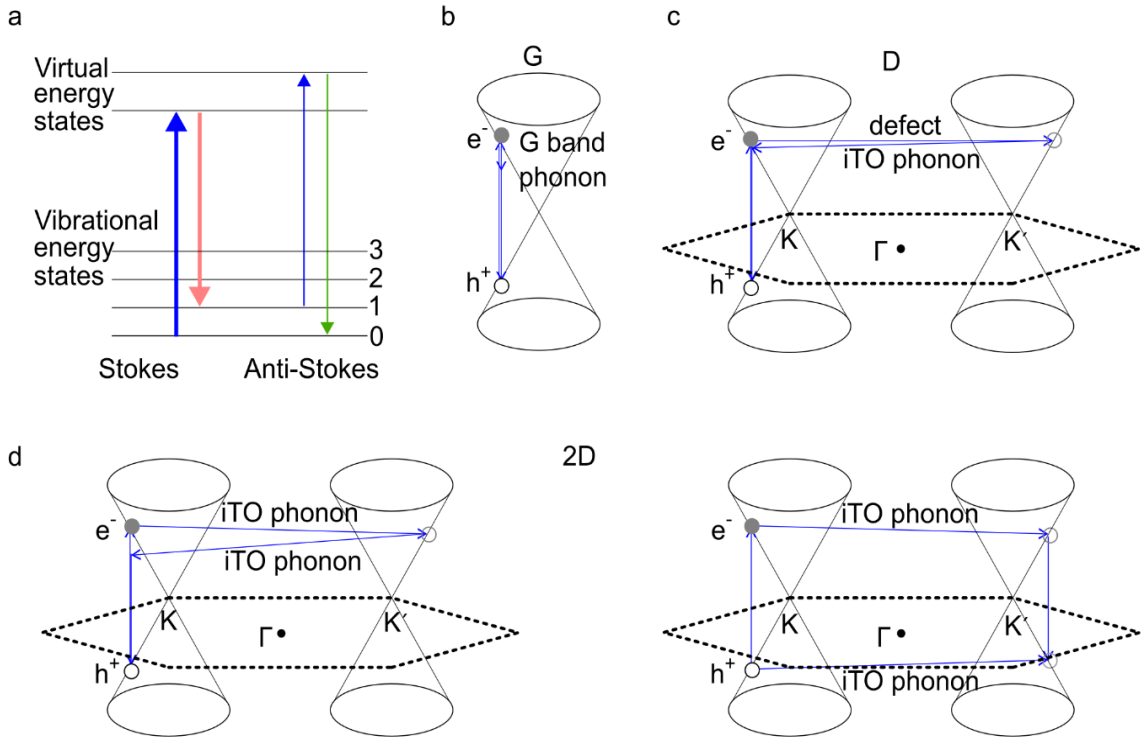

Figure 2.2 Raman spectroscopy. (a) Stokes and anti-Stokes Raman scattering process. The origin of (b) G, (c) D, and (d) 2D Raman signal in graphene.

2.1.4 Fourier transform infrared spectroscopy

Fourier transform infrared spectroscopy (FTIR) belongs to a group of non-destructive analytical techniques. FTIR provides qualitative and quantitative information about the sample composition. FTIR is based on the interaction of infrared radiation with a sample.

The radiation is absorbed when the energy of bond vibration is the same as the energy of the incident radiation. Different bonds have different vibration energy. Therefore, they absorb different wavelengths (frequency) of the radiation. The result of this method is a graph of intensity dependence on frequency, which determines the bonds present in the sample.

2.1.5 Dynamic light scattering

Dynamic light scattering (DLS) is a method for the determination of particle size distribution in a suspension. The principle of this method is based on evaluating the scattering pattern. A monochromatic light source is used to enlighten particles in suspension. Particles scatter the light, and due to their continuous movement (Brownian motion), destructive and constructive interference takes place. Hence the intensity of scattered light fluctuates. The intensity of scattered light is highly correlated to the size of particles, where the autocorrelation function is used for determining the hydrodynamic radius R_H of solid particles. It is usually assumed that the particles are spherical and then the Stokes-Einstein equation is used:

$$D_t = \frac{k_B T}{6\pi\eta R_H},$$

where k_B is the Boltzmann constant, T is the temperature, and η is the viscosity.

2.1.6 Zeta potential

Zeta potential is a parameter used for the determination of the surface charge of particles at the particle-liquid interface. It describes the electrostatic repulsion/attraction between particles. In colloids and suspensions, particles are surrounded by liquid, and an electrical double layer is formed on the surface of particles. The double layer consists of an inner (Stern) and outer (diffusion). In the inner layer, ions are strongly bound to the surface of the particle. In diffusion, layer ions are loosely associated with a particle. There is a boundary (slipping plane) in this layer, where the ions and particles form a stable entity. This stable entity of ions moves along with the particle, while the ions outside the slipping plane stay with the liquid. The potential at the slipping plane of the entity is the Zeta potential. The value of this potential indicates the stability of colloids and suspensions due to the electrostatic repulsion of particles. Generally, the suspension is considered stable when the potential is greater than +30 mV and smaller than −30 mV. If the potential is out

of these values, particles in suspension tend to aggregate and flocculate due to van der Waals forces.

Zeta potential is measured in a cell consisting of two electrodes and a solution. When a voltage is applied to the solution, particles (and ions within the slipping plane region) move toward the electrode of the opposite polarity. The particle velocity is measured at different applied voltages by the Doppler technique and used to calculate the Zeta potential. The Doppler technique is based on the relation between the particle velocity and the frequency of scattered light by moving particles:

$$\mu_e = \frac{\nu}{E},$$

where μ_e is the electrophoretic mobility, v is the particle migration (velocity in electrical field E). The Zeta potential (ζ) is then calculated by Henry´s, Helmholtz-Smoluchowski, or Hückel equation depending on the ratio of particle size and thickness of an electrical double layer:

$$\mu_e = \frac{2\varepsilon_r \varepsilon_0 f(\kappa a)}{3\eta} \zeta$$

$$\mu_e = \frac{\varepsilon_r \varepsilon_0}{\eta} \zeta$$

$$\mu_e = \frac{2\varepsilon_r \varepsilon_0}{3\eta} \zeta,$$

where ε_0 is the permittivity of vacuum, ε_r is the relative permittivity, η is the viscosity of a medium, $f(\kappa a)$ is Henry´s function, and ζ is the Zeta potential.

2.2 Mechanical testing

2.2.1 Compression

Figure 2.3 shows the experimental setups that were used for the compression testing of the GA. The first setup is a homemade version of a press. A weight is placed on the sample and the applied pressure is equaled to the gravitational force of a weight applied on the surface area of the sample. There is also a possibility to examine two-point probe electrical measurements with this setup by taking the contact on the top and bottom of the sample.

The samples measured using this approach are in the shape of a block with dimensions in the mm range. The second setup is a diamond anvil cell used for experiments above GPa pressures. The cell is based on two opposing diamonds which push against each other. The pressure created by diamonds is transmitted using a pressure-transmitting medium (NaCl, silicone oil, or gases) to the sample which is surrounded by the medium. Along with the sample pressure monitor (such as ruby) is kept in the medium. The behavior of pressure monitors under applied pressure is known. Therefore, the fluorescence shift of the ruby monitor under applied pressure determines the actual pressure on the studied sample. The elasticity is determined by the reversibility of the G peak shift in the Raman measurement of the GA.

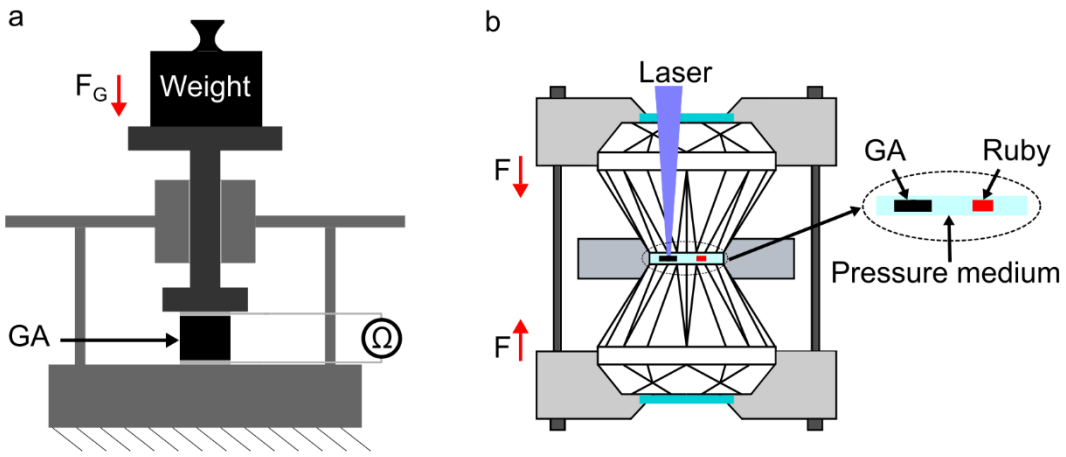

Figure 2.3 Schematic drawings of the experimental setups for the compression testing of graphene aerogels (GA): (a) a mechanical press used for low-pressure stress-strain and electrical measurements, and (b) a diamond anvil cell used for high-pressure measurements using Raman spectroscopy.

2.2.2 Tensile

The tensile testing was performed using a homemade setup (Figure 2.4a). The sample is shaped into a similar shape used in standard tensile measurement consisting of two shoulders and a thinner part in between. One of the shoulders is attached to a fixed metal block and a hook is glued to the other shoulder. The sample is pulled via a mass of a container (water is added into a container) and hung on a metal hook. The gravitational force acting on a container per the surface area of the thin part of the sample is the applied pressure. To perform the electrical and mechanical measurements simultaneously, gluing is done with electrically conductive glue (silver epoxy or carbon glue), and rigid contact is

achieved by non-conductive epoxy glue. Standard mechanical clamping cannot be used due to the high flexibility of the GA samples.

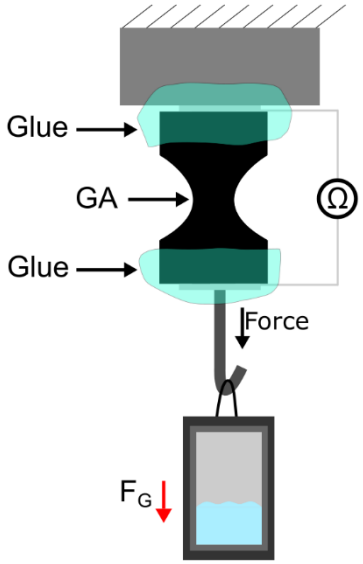

Figure 2.4 Schematic of a homemade setup used for tensile testing of graphene aerogels (GA) using gravitational force acting on a container with a liquid.

2.2.3 Durability

The durability of the GA sample was tested using mechanical stimulation. The mechanical stimulation is excited with a Teflon knob attached to an electric DC motor (Figure 2.5). The sample is attached to a Cu tape acting as a bottom and top contact and stimulated with a knob. The strain induced by a knob is roughly 10%. The durability is evaluated visually by comparing the shape of the sample before and after cycling and electrically. The electrical response of the sample is measured as a current change at a constant voltage. The signal of the compressed sample shows a slight jerking motion at the upper bound at ~ 0.45 mA due to the slip-stick motion caused by the friction between the metal contact and the rotating spindle.

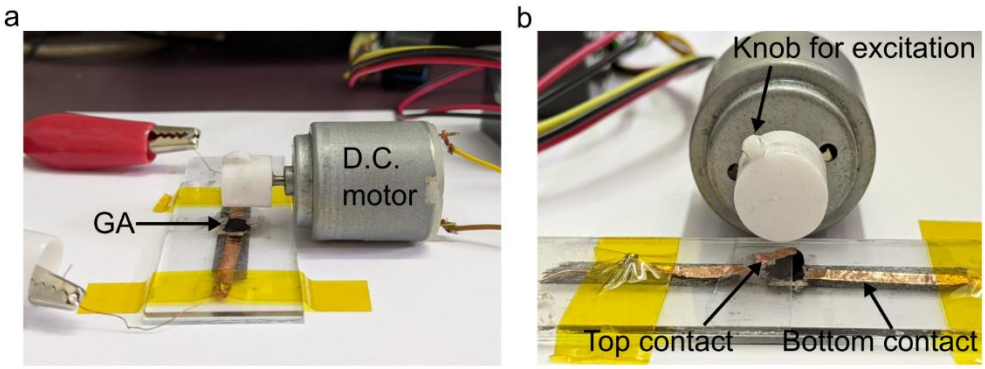

Figure 2.5 Durability testing of a graphene aerogel (GA). (a,b) The dynamic stability testing was done using an electric motor with a rotating asymmetric spindle which was delivering periodic pressure to the tested sample.

2.3 Thermal properties

2.3.1 Laser flash analysis

Laser flash analysis (LFA) is used to determine the thermal conductivity of materials based on thermal diffusivity measurements. In the LFA apparatus, the bottom of the plane-parallel sample is heated up by an energy pulse. The infrared detector measures the time dependence of temperature change on the upper surface. The obtained signal is fitted with a model to find the thermal diffusivity. The obtained thermal diffusivity (a) is used for calculating the thermal conductivity (λ):

$$\lambda = a \cdot c_P \cdot \rho,$$

where c_p is the specific heat capacity and ρ is the density. Usually, the standard (improved Cape-Lehman) model is used for common materials. This model considers that the pulse energy is totally absorbed on the front face of the sample. The assumption of total absorption on the front face of the sample does not fit the reality in the case of porous materials. This problem is solved by using a different model (penetration model), which considers the absorption of the pulse energy over a thin layer into the sample thickness. The penetration model was developed by the company NETZSCH based on McMasters work.[8]

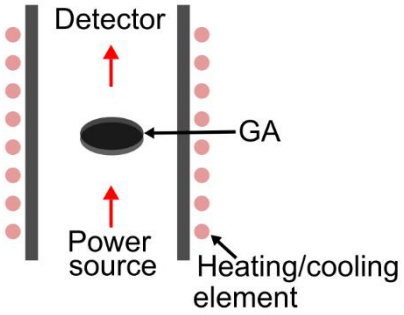

Figure 2.6 Schematic of a laser flash analysis

2.3.2 Thermal gravimetric analysis

Thermal gravimetric analysis (TGA) is used to determine the thermal stability of a material. The sample is loaded into a crucible and heated up inside the TGA machine, where a defined atmosphere is settled via a continuous flow of gases. The heating of a sample is done at a constant heating rate (usually 10 °C.min^{-1}). The mass of a sample is monitored over the whole experiment. Additionally, the products of thermal decomposition are analyzed using a mass spectrometer. The main result of this technique is usually the temperature dependence of the mass loss of the sample.

References

1. Jonkman, J. E. N., Swoger, J., Kress, H., Rohrbach, A. & Stelzer, E. H. K. [18] Resolution in optical microscopy. in *Methods in Enzymology* vol. 360 416–446 (Academic Press, 2003).
2. Haasch, R. T. X-Ray Photoelectron Spectroscopy (XPS) and Auger Electron Spectroscopy (AES). in *Practical Materials Characterization* (ed. Sardela, M.) 93–132 (Springer, 2014). doi:10.1007/978-1-4614-9281-8_3.
3. Jones, R. R., Hooper, D. C., Zhang, L., Wolverson, D. & Valev, V. K. Raman Techniques: Fundamentals and Frontiers. *Nanoscale Research Letters* **14**, 231 (2019).

4. Adya, A. K. & Canetta, E. Chapter 16 - Nanotechnology and its applications to animal biotechnology. in *Animal Biotechnology (Second Edition)* (eds. Verma, A. S. & Singh, A.) 309–326 (Academic Press, 2020). doi:10.1016/B978-0-12-811710-1.00014-8.
5. Wu, J.-B., Lin, M.-L., Cong, X., Liu, H.-N. & Tan, P.-H. Raman spectroscopy of graphene-based materials and its applications in related devices. *Chem. Soc. Rev.* **47**, 1822–1873 (2018).
6. Malard, L. M., Pimenta, M. A., Dresselhaus, G. & Dresselhaus, M. S. Raman spectroscopy in graphene. *Physics Reports* **473**, 51–87 (2009).
7. Ferrari, A. C. & Basko, D. M. Raman spectroscopy as a versatile tool for studying the properties of graphene. *Nature Nanotech* **8**, 235–246 (2013).
8. McMasters, R. L., Beck, J. V., Dinwiddie, R. B. & Wang, H. Accounting for Penetration of Laser Heating in Flash Thermal Diffusivity Experiments. *Journal of Heat Transfer* **121**, 15–21 (1999).

3 Synthesis of graphene aerogels

3.1 Introduction

3D graphene structures can be prepared by various methods, including templated or template-free synthesis.[1] In the case of the CVD method, the material is coated on a porous template (e.g., metallic foam, metal oxides, SiO_2, etc.).[2] However, graphene foam prepared by CVD methods is generally noncompressible, brittle, and non-scalable.[3] Mechanically stable graphene aerogels can be prepared using template-free methods using GO precursors.[4–7] Several synthesis methods have been developed using GO as a starting material, such as hydrothermal reduction,[7,8] chemical reduction,[9] cross-linking,[10] etc. Most of the synthesis methods of 3D graphene aerogels involve two steps: (i) self-assembly of GO flakes into the 3D structure and (ii) reduction of GO into graphene. These steps can be performed simultaneously or one after the other. The GO-based methods are simple and versatile, but there are challenges associated with them.

One of the challenges is the degradation of GO because of ageing. The ageing of GO has been recently observed after long-term storage or exposure to light.[11] As GO is functionalized with various oxygen species, mainly carboxyl, hydroxyl, and epoxy groups,[12,13] the functional groups determine the bonding between individual graphene flakes while synthesizing graphene aerogels. However, these oxygen groups might change after the interaction of GO with the environment. They degrade even faster when exposed to light.[14,15] The desorption of oxygen and the change of the ratio of individual oxygen species reduce the number of active sites in GO.[16] These changes in the composition cause the aged GO not to form a stable hydrogel in the hydrothermal synthesis of graphene aerogel. The instability is mainly caused by the binding of a large number of graphene layers through van der Waals forces.[17] This leads to the formation of agglomerates and sedimentation of the dispersed GO sheets in water, which hampers the graphene aerogel synthesis.

Another problem associated with the synthesis of graphene aerogels is defects. Some crystallographic defects are already naturally present in the starting GO material,[18] and other defects are formed during the synthesis. But the ageing causes a significant increase in their density, especially for lattice/topological and edge defects due to the loss of oxygen species.[19] It has been shown the higher the number of defects, the lower the electrical

conductivity and mechanical strength of the resulting graphene aerogel is obtained.[20] Therefore, effective mitigation strategies to prevent ageing and defects in GO are needed for synthesizing mechanically stable and electrically conductive 3D graphene structures.

In this thesis, a template-free synthesis method of covalently cross-linked GA is developed. Microporous GA is prepared using a three-step synthesis method that involves hydrothermal synthesis, freeze-drying, and high-temperature annealing. The work focuses on the study of the three-step synthesis method of GA. At each step, the structure and composition of the materials are thoroughly characterized using SEM, Raman spectroscopy, XPS, and FTIR. Plasma and heat assisted approaches for mitigating ageing and defects in GA are investigated. As a result, a standard operation procedure (SOP) of the GA synthesis is developed. The SOP is based on the optimized synthesis parameters that enable the fabrication of centimeter-sized samples of covalently cross-linked GA with exceptional mechanical and electrical properties. All the GA samples studied in the following chapters of this thesis were prepared according to this SOP. Along with the standard procedure, the solutions to the problems caused by GO ageing and defects are proposed and discussed. A practical solution is demonstrated using oxygen plasma treatment and high-temperature annealing in vacuum.

3.2 Experiments

3.2.1 Freeze-drying

Freeze-drying is a process where ice or other frozen solvents are removed from the material via sublimation. Sublimation is a phenomenon in which the substance is transferred from the solid state directly to the vapor state without passing the liquid phase. It is usually used in food processing and biological and biomedical applications. In the case of the water phase diagram, freeze-drying transforms ice (low temperature, low pressure) directly to the vapor phase (low pressure, high temperature).

In this work, the freeze-drying process was done using a homemade setup (Figure 3.1). The design of the setup is fairly simple, taking into account that the material needs to be gently heated up under a vacuum so that the liquid sublimes. It consists of a reactor and heat exchanger. The whole setup is kept under a vacuum using a rotary vane vacuum pump. The samples are frozen outside the setup in a liquid nitrogen bath and then immediately placed into the reactor. The reactor is kept at room temperature, whereas the

heat exchanger is cooled down to negative temperatures. This temperature difference creates a concentration gradient of water vapor which acts as a driving force for water removal. The cooling of the heat exchanger is done by cold gas, which is cooled by flowing through a liquid nitrogen tank. This homemade design allows for using significantly lower temperatures (below -130 °C) and pressures (0.01 mbar) than commercial setups.

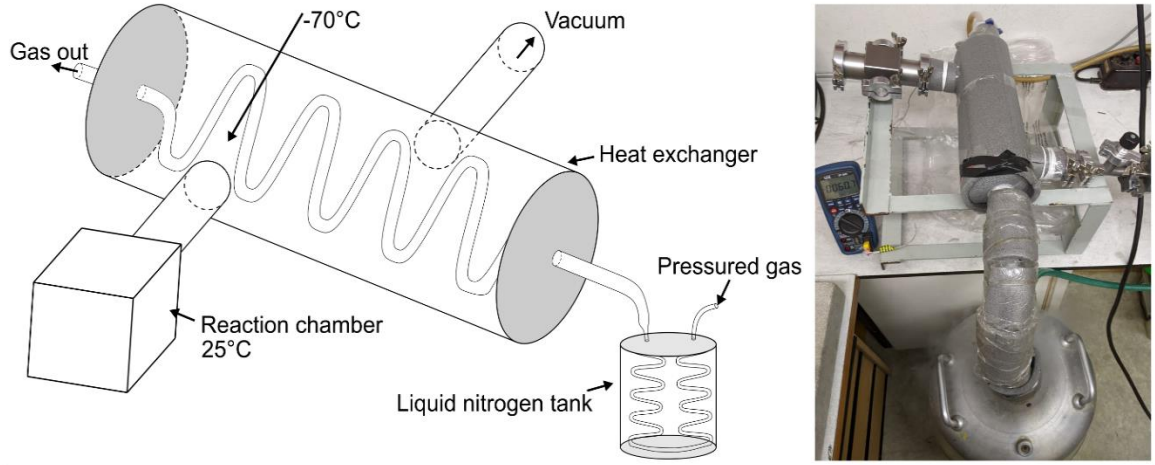

Figure 3.1 Drying technique used in graphene aerogel synthesis. Schematic and photograph of a homemade setup used for freeze-drying.

3.2.2 Furnace

One of the key steps in the GA synthesis is high-temperature annealing in a vacuum furnace. Recently, Guo et al. reported annealing of 3D graphene-based structures at extremely high temperatures of 2800 °C, which improved the through-plane thermal conductivity of the GA.[21] However, the GA sample in this work was heated up just for a few seconds by passing an electrical current through it in a quartz tube. In this thesis, another annealing approach is used. A furnace for indirect GA sample heating was built up to avoid passing current directly through the sample, as the current might damage the sample or lead to inconsistent annealing temperature when the sample conductivity varies.

The developed furnace (Figure 3.2) consists of two graphite rods (40 × 40 × 3200 mm) which are connected via a thin graphite paper (0.2 mm thick). A sample is placed in between two graphite papers or wrapped in graphite paper to maintain a homogeneous temperature. Everything is kept in a vacuum chamber. The vacuum is governed by a combination of a rotary vane vacuum pump and a turbomolecular pump, which reaches pressures in the range of 10^{-5} mBar. If required, a gas inlet was installed, which can

replace the vacuum with a different gas atmosphere (N_2 or Ar). The heating is done by passing a high electrical current through the thin graphite paper. Therefore, the high temperature is only reached on the paper and not along the whole graphite rods. Temperatures below 1500 °C were measured indirectly with a pyrometer (Optris, model CSlaser 2MH CF2). Temperatures above 1500 °C were determined from the emission spectrum of glowing graphite paper using an optical emission spectroscope equipped with an optical fiber (Ocean Optics STS-NIR). The accuracy of the temperature determined by the spectrometer was done according to the melting temperature of Mo and Pt.

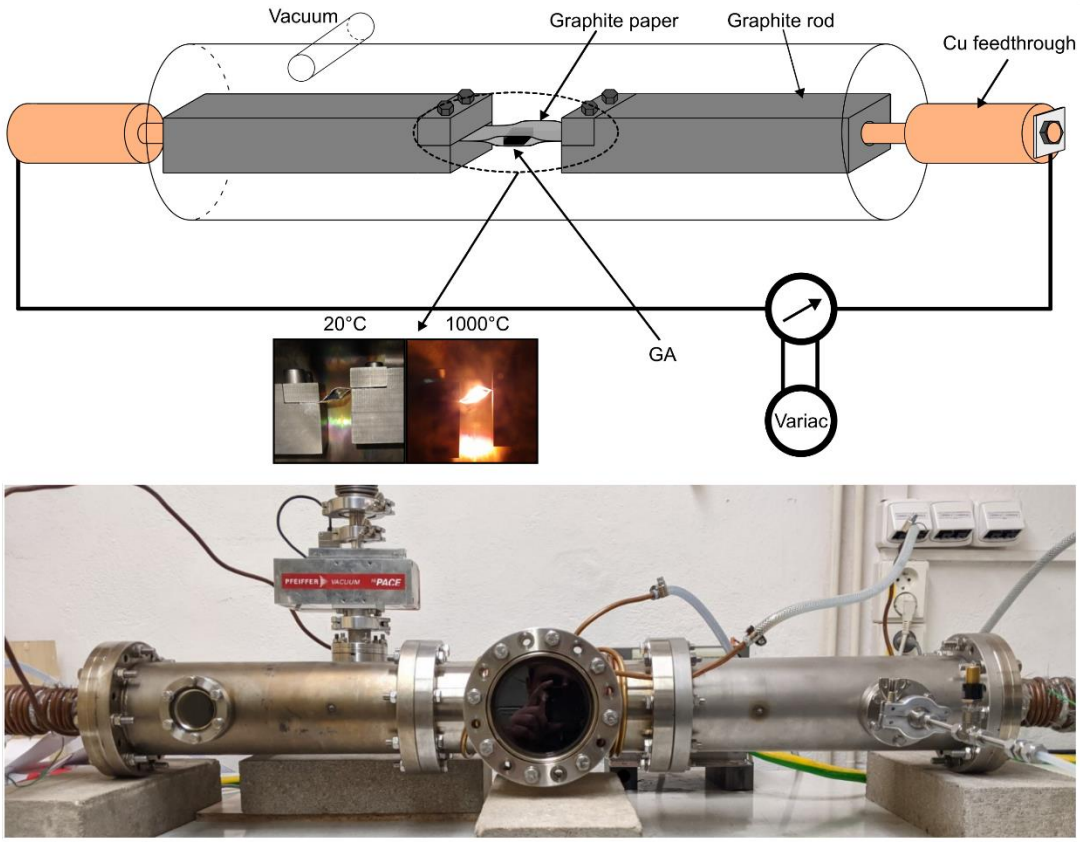

Figure 3.2 High-temperature furnace used for the annealing of graphene aerogel (GA) samples in vacuum or inert gas atmosphere.

The main advantage of the high-temperature furnace with a graphite paper heating element is the possibility of rapidly controlling the annealing temperature by regulating the current with a variable transformer, which allows adjusting the temperature with a ramping rate of 1000 °C.min^{-1}. In contrast, commercial furnaces provide a much slower ramping rate of around 10 °C.min^{-1}. Moreover, commercial furnaces cool down very slowly after the annealing due to the large mass of heating elements, even though they use active

cooling systems. On the other hand, our furnace does not require external cooling after the annealing is finished because the graphite paper heating element has a small mass. Once the passing current is stopped, the temperature of the graphite paper drops immediately below 380 °C (the limit of a pyrometer). The cooling installed on the furnace is used only for annealing at temperatures above 2000 °C to protect the stainless steel tubes and electrical feedthroughs.

3.3 Synthesis of graphene aerogels

As discussed in Chapter 1, the chosen preparation technique is hydrothermal synthesis. This approach was described already in 2010, where hydrothermal reduction of GO was followed by freeze-drying to form graphene aerogel.[7] Unfortunately, it was found that the as-prepared graphene aerogels using this method are characterized by poor mechanical and electrical properties due to a high concentration of defects and structural inhomogeneities.[22] To decrease the amount of defects and improve the physical properties of the GA, an additional high temperature annealing step was introduced.[23] In this thesis, the synthesis method of the GA is a combination of hydrothermal reduction of GO followed by freeze-drying and high temperature annealing. All the synthesis parameters were experimentally investigated to obtain the best graphene aerogel in terms of physical properties and then summarized in the SOP.

3.3.1 Standard operation procedure

The SOP fabrication method is schematically depicted in Figure 3.3. Following this SOP leads to the preparation of a GA cylinder with a diameter of 12 mm and a height of 23 mm with a density of 7 $mg.cm^{-3}$.

a) 60 mg of GO in the form of powder is weighted on the laboratory weight balance using a weighing paper to reduce the unintended electrostatic interaction of GO to the surface. GO powder is transferred into a reagent bottle. 30 ml of deionized water is measured using a graduated cylinder. The water is carefully poured into the reagent bottle to wash the GO powder which is stuck on the wall. The bottle is sealed with parafilm.

b) GO solution is delicately mixed with a hand and immersed in an ultrasonic bath. The temperature of the bath is kept in the range of 30-40 °C. The solution is sonicated for 60 minutes.
c) A Teflon-lined hydrothermal autoclave reactor with a volume of 50 ml is washed using deionized water and ethanol. 30 ml of the freshly sonicated GO solution is added to the Teflon part of the reactor and capped. The Teflon part is inserted inside a stainless steel shell and closed with a stainless steel lid. The well-tightened autoclave is placed in an oven. The oven is slowly heated up to 180 °C and kept for 6 hours at this temperature.
d) Once the timer expires, the autoclave is taken out of the oven and cooled down at room temperature. After 2-3 hours, the autoclave is sprinkled with water and in 10 minutes, the stainless steel lid is slowly opened to gradually decrease the pressure inside the autoclave. The Teflon part is taken out and opened up. The volume is filtered using a filtration apparatus. The filtration apparatus consists of a Buchner funnel with a filter paper assembled with a Buchner flask connected to a vacuum pump. The filtered sample is 3 times washed with deionized water. The as-prepared sample is a reduced graphene oxide hydrogel. The hydrogel can be stored closed in a water environment for months. After this step, the hydrogel is already a stable structure and the most suitable for mechanical cutting. Cutting is possible by hand using standard blades or a linear saw at low speed.
e) Freeze-drying is performed in a homemade free-dryer device to remove the water from the hydrogel. The hydrogel is frozen-down with liquid nitrogen for roughly 30 s. The frozen sample is inserted into the freeze-dryer and kept at a temperature ranging from -80 to -70 °C and a pressure of around 0.5 mBar for 14 hours. This drying step converts the hydrogel into a reduced graphene oxide aerogel (rGA).
f) The sample is loaded into the high-temperature furnace to remove the oxygen species from the rGA. The furnace is kept under a vacuum with a pressure of 10^{-5} mBar. The sample is annealed at the temperature of 1300 °C for 30 minutes. This final step is a key step for the fabrication of the high-quality GA, which is responsible for the significant reduction of the amount of defects in the samples.

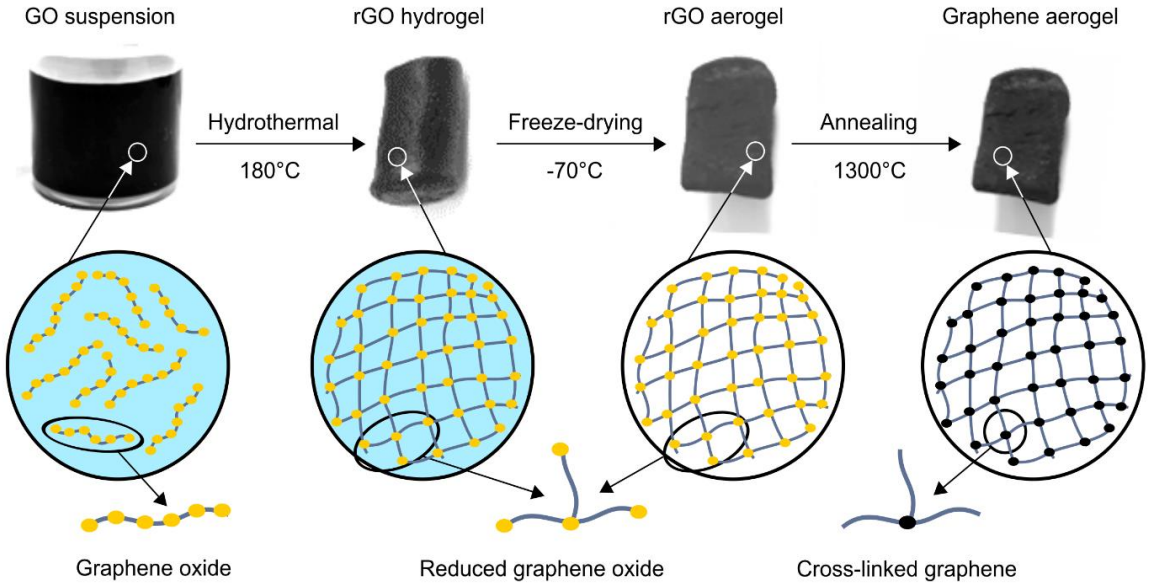

Figure 3.3 Schematic of the covalently cross-linked graphene aerogel fabrication using a three-step synthesis method.

3.3.2 Characterization of materials

GO used in the synthesis, according to the information provided by the supplier, comprises graphene flakes with an average size of a few micrometers. SEM images (Figure 3.4a) of this material depict the GO in the form of merged flakes with a size of a few micrometers. The Raman spectra (Figure 3.4b) of the GO show the presence of the D and G graphene bands with roughly the same intensities and a trace of a broad 2D band. The XPS analysis of the GO (Figure 3.4c,d) reveals the element composition contains only carbon (73%) and oxygen (23%). The FTIR absorbance spectrum of GO (Figure 3.5a) reveals several peaks. These peak are ascribed to vibration modes of carboxyl (COOH) (1615-1725 cm^{-1} including C–OH vibrations at 3,150 cm^{-1} and 995 cm^{-1}), hydroxyl (namely phenol, C–OH) (2965-3800 cm^{-1} and 1135 cm^{-1}, C–OH vibrations from COOH and H_2O), C–O–C epoxide (between 1200-1385 cm^{-1}), sp^2-hybridized C=C (1550-1650 cm^{-1}, in-plane vibrations) and ketonic species (C=O) (1725-1810 cm^{-1}).

Once the rGA is prepared via the SOP (Step d), the SEM images (Figure 3.4a) show the formation of a 3D porous structure with the average pore size in the range of 1-2 µm. Carbon and oxygen are the only elements that are measured in this structure using XPS analysis. The amount of carbon is increased to 89%, and oxygen is decreased to 11% (Figure 3.4c,d 3.5a). The decreasing total amount of the oxygen content, along with the

deep analysis of the various oxygen group content, reveals that the GO was reduced partially during the hydrothermal process, resulting in rGA. According to XPS and FTIR data, the relative content of carboxyl groups was increased two times after the hydrothermal process. The Raman spectra of the rGA (Figure 3.4b) are very similar to the GO spectra, but the intensity of the D peak is slightly reduced. The rGA is thus characterized by a formation of a porous 3D structure, reduction of the oxygen species, and slight improvement in the crystalline quality of the material. The rGA is already a 3D form consisting of graphene sheets but shows poor mechanical properties (plasticity, brittleness) when manually handled.

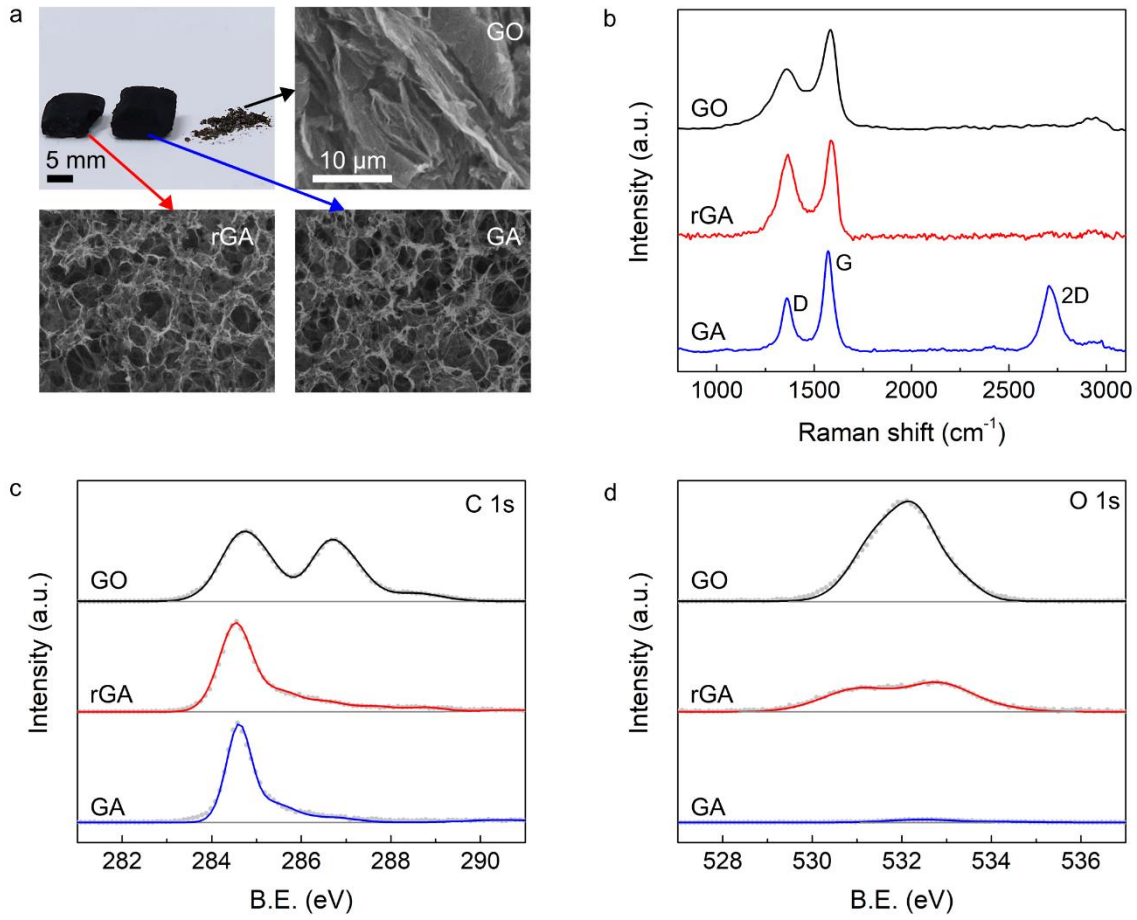

Figure 3.4 Characterization of the graphene oxide (GO), reduced graphene oxide aerogel (rGA), and graphene aerogel (GA). (a) Photographs and scanning electron microscopy images, (b) Raman spectra, (c) and (d) X-ray photoelectron spectroscopy C 1s and O 1s spectra of GO, rGA, and GA.

To further improve the properties of the rGA, high-temperature annealing at 1300 °C in vacuum is performed to produce oxygen-free GA. No change in the SEM micrograph

(Figure 3.4a) is observed after the annealing of the rGA. The XPS analysis, along with FTIR spectra (Figure 3.4c,d 3.5a) of the GA, shows almost complete removal of all the oxygen content (< 0.6% remaining) from the structure. Interestingly, there is no signal of the carboxyl species found in the GA after the peak deconvolution. The Raman spectra (Figure 3.4b) are characterized by a decrease of full width at half maxima of all peaks and intensity of the D peak and a rise of the 2D peak. The observed decrease of the D peak and sharpening of the G peak suggest a reduction of the number of defects and increasing crystallinity of the sample, which is in line with the results from XPS. As the Raman spectra were gathered from roughly a 1 μm spot, they contain information about the bulk and edges of graphene sheets. The presence of a D peak after annealing can be explained by the presence of edge defects, kinks and folds in graphene sheets.[24] The ratio of 2D to G peak intensities suggests a few-layer character of graphene sheets in the GA. The multi-layer composition is confirmed using X-ray diffraction (XRD) results (Figure 3.5b), which show a broad peak at 2θ = 26.2°, which is assigned to the (002) crystal plane of graphite. The comparison of all results from the GO, rGA, and GA samples using Raman spectroscopy and XPS is noted in Table 3.1.

Table 3.1 Evaluation of Raman spectroscopy and X-ray photoelectron spectroscopy measurements of graphene oxide (GO), reduced graphene oxide aerogel (rGA), and graphene aerogel (GA).

	Raman spectroscopy								XPS	
	Position (cm^{-1})			FWHM (cm^{-1})			$\frac{I_D}{I_G}$ (-)	$\frac{I_{2D}}{I_G}$ (-)	N_C (%)	N_O (%)
	D	G	2D	D	G	2D				
GO	1365	1580	-	162	94	-	0.58	-	73	27
rGA	1368	1587	2744	127	75	254	0.84	0.13	89	11
GA	1367	1576	2714	82	60	110	0.52	0.65	> 99.4	< 0.6

The annealing led to a significant change in the mechanical properties of the GA. The GA exhibits elasticity and strength, while the rGA is plastic. The mechanical characterization of the GA is presented in detail in Chapter 4. The change in the mechanical properties caused by the annealing is attributed to the removal of the oxygen species and, most importantly, to the increase of graphene sheets cross-linking. The removal of oxygen restores the crystallographic structure, strength and flexibility of graphene sheets. As the graphene sheets self-assembled in the hydrothermal synthesis are weakly bonded only via van der Waals forces, these bonds cannot resist high forces. Therefore, the rGA

structure is not mechanically strong and deforms plastically under mechanical strain. The high-temperature annealing breaks the C–O bonds of adsorbed oxygen species and transfers them back to the graphene-like C–C bonds. Covalent C–C bonds are also created at the overlap of two graphene sheets in the annealed GA. Experimental evidence of the formation of covalent bonds in the GA is provided in Chapter 4. The carbonization and cross-linking processes in the GA can be described similarly to the pyrolysis of carbon fibers.[25,26]

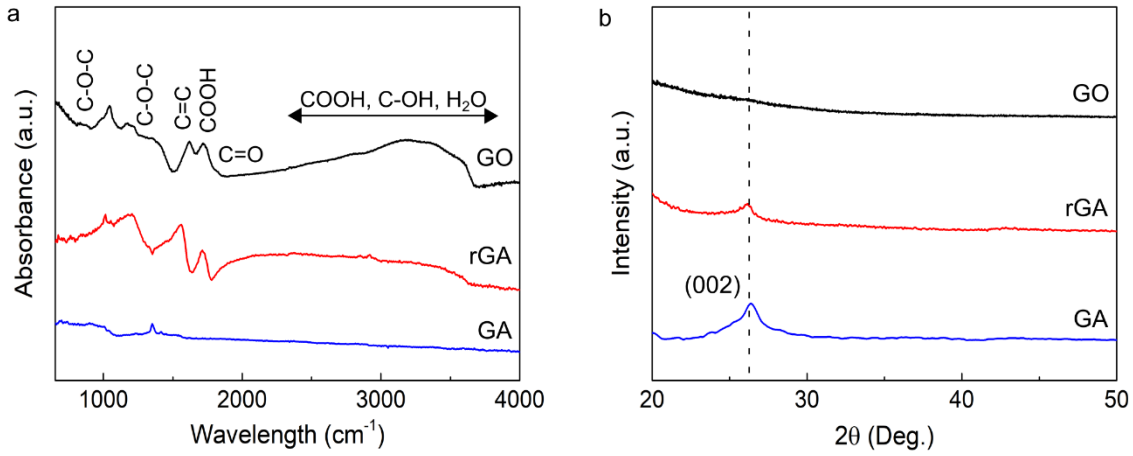

Figure 3.5 Characterization of the graphene oxide (GO), reduced graphene oxide aerogel (rGA), and graphene aerogel (GA). (a) Fourier-transform infrared spectra, and (b) X-ray diffraction of GO, rGA, and GA.

3.4 Reversing changes of ageing in graphene oxide using oxygen plasma

When producing materials, it is very important to be able to reproduce them with the most similar properties. Therefore, one of the crucial parts is always to have the same starting GO material. GO used in this study was purchased from commercial sources, which is why its properties can vary due to ageing or different batch from the supplier. A thorough examination of the structure and chemical composition of GO before and after ageing was carried out to understand and minimalize these effects in the synthesis of GA.

In the case of the GA synthesis, first it is important to obtain a compact and stable hydrogel. The freshly purchased GO enabled in most of the cases to form a stable hydrogel using hydrothermal synthesis (left image in Figure 3.6). However, GO affected

by ageing for 1 year (aGO) did not result in a stable hydrogel. Instead, distorted and broken pieces were produced using the same hydrothermal synthesis parameters (middle image in Figure 3.6). Some purchased batches of GO from the supplier have also failed to produce compact cylindrical hydrogels. O_2 plasma treatment (120 s at 50 W with 50 sccm of O_2 gas) was applied to the aGO powders to reverse the effects of ageing. The plasma treated aGO (pGO) enabled the formation of a compact and stable rGO hydrogel in the hydrothermal synthesis again (right image in Figure 3.6), similarly to the fresh GO.

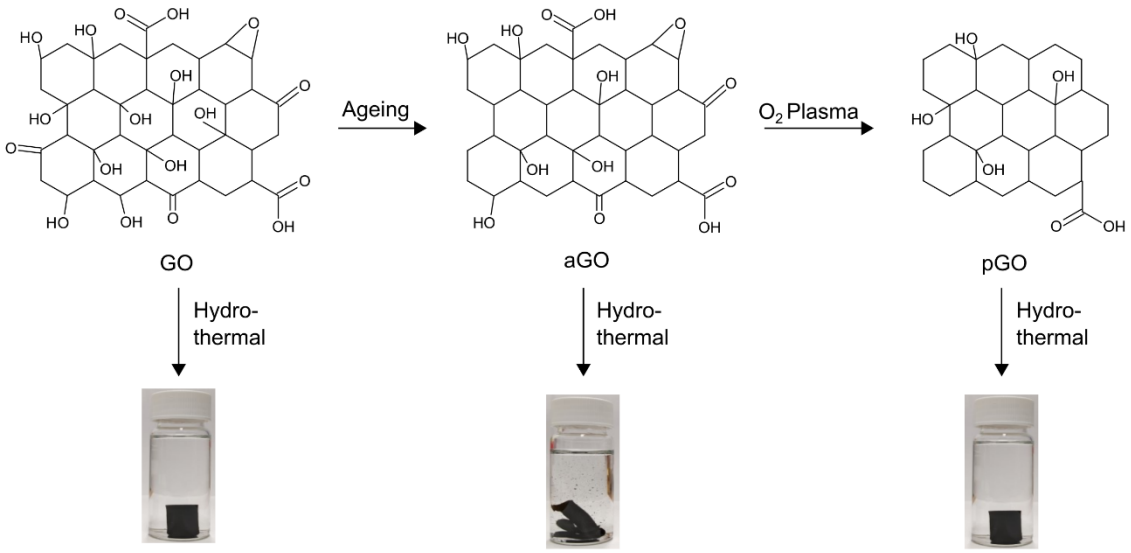

Figure 3.6 Schematic of the fabrication process of the graphene hydrogels using hydrothermal synthesis from GO, aGO and pGO starting materials.

3.4.1 The influence of ageing and plasma treatment on the composition of graphene oxide

The Raman spectrum of the GO, aGO and pGO samples depicts two major peaks at 1368 and 1598 cm^{-1} associated with the D and G bands of the GO (Figure 3.7a). The I_D/I_G ratio of the GO and aGO samples is 0.87 and 0.81, respectively. Whereas the for the pGO, the ratio slightly decreases to 0.65 and the full width at half maxima of all peaks increases. This might be due to the plasma removal of some oxygen functional groups bound to defects.[27]

The FTIR absorbance spectrum of GO (Figure 3.7b) reveals several peaks. These peak are ascribed to vibration modes of carboxyl (COOH) (1615-1725 cm^{-1} including C–OH vibrations at 3150 cm^{-1} and 995 cm^{-1}), hydroxyl (namely phenol, C–OH) (2965-3800 cm^{-1}

and 1135 cm^{-1}, C–OH vibrations from COOH and H_2O), C–O–C epoxide (between 1200-1385 cm^{-1}), sp^2-hybridized C=C (1550-1650 cm^{-1}, in-plane vibrations) and ketonic species (C=O) (1725-1810 cm^{-1}).[28,29] The main difference in the FTIR spectrum between GO and aGO is observed in the relative intensities of the peaks. This difference indicates that there is a quantitative difference between the total content of oxygen and the ratio of oxygen functional groups in the GO and aGO samples. After plasma treatment, the FTIR spectrum of pGO shows a minor change to the aGO. As all the peaks in the FTIR spectra overlap, identification of the peaks and quantitative analysis of the changes is difficult and inaccurate from FTIR.[28] It is to be noted that any concrete conclusion from the structural and vibrational analysis is challenging. Therefore, the quantitative elemental and chemical analysis of the carbon and oxygen bonds, as well as the ratio of all the species, was done using XPS.

XPS analysis of the GO, aGO and pGO samples is depicted in Figure 3.7c,d. The C 1s spectra of GO in Figure 3.7c consist of five major peaks. The peaks centered at 284.6 and 285.2 eV correspond to the carbon-carbon bonds with sp^2 and sp^3 hybridization, respectively. As the peaks of epoxide and hydroxyl groups have similar binding energies,[30] they are shown as a combination of a single peak at 286.5 eV. The carbonyl/quinone species are located at 287.1 eV and the carboxyl species at 288.5 eV.[31–33] The corresponding O 1s spectra with the deconvoluted C–O, C=O, and COOH peaks of the GO are shown in Figure 3.7d. The quantitative analysis carried out considering the area under the peaks and the relative sensitivity factor shows that the C/O ratio is ~ 2.7.

After aging, the XPS C 1s spectra (Figure 3.7c) depict two broad peaks as observed in non-aged GO. These peaks are deconvoluted the same as GO samples containing various oxygen-related groups. There is a significant decrease observed in the oxygen-functionalized carbon peak. The relative percentage of the sp^2+sp^3 carbon content increased from 51.1% to 58.4%, with oxygen functionalized carbon loss. A 23.8% decrease is observed related to epoxide/hydroxyl groups, whereas the relative content of carbonyl/quinone decreased ~ 3%. This suggests that the ageing results in the loss of oxygen-related functional groups from GO.

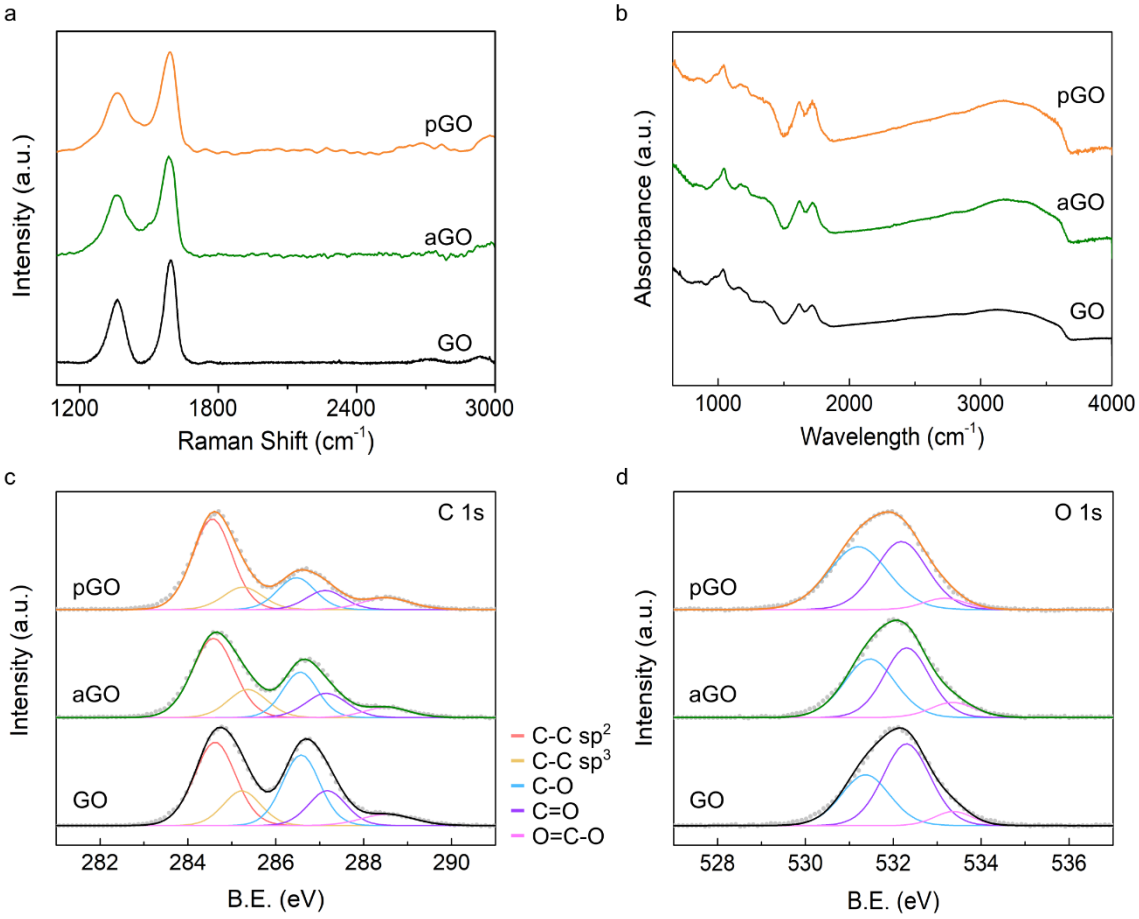

Figure 3.7 Characterization of graphene oxide (GO), aged graphene oxide (aGO), and plasma treated aged graphene oxide (pGO) using Raman, FTIR and XPS. The comparison of (a) Raman spectra, (b) Fourier-transform infrared spectra, and (c),(d) X-ray photoelectron spectroscopy C 1s and O 1s spectra of GO, aGO, and pGO.

The deconvoluted C 1s spectra of pGO denote a further decrease in the epoxide/hydroxyl groups. However, the relative content of carboxyl (–COOH) has slightly increased from 6.1 to 8.3% (see Table 3.2). With the knowledge that the stable hydrogel is prepared from pGO, it is evident that the number of the carbon-oxygen species is crucial for the formation of the stable hydrogel. It is to be noted that the –OH and –COOH functional group plays a significant role in forming a stable solution of GO with water.[34,35] Here, the plasma helped with the restructuring of the functional group contents that led to the fabrication of stable rGO hydrogels via the hydrothermal process. The corresponding O 1s spectra of GO, aGO and pGO are shown in Figure 3.7d and the quantitative analysis is given in Table 3.2.

Table 3.2 The quantitative analyses of X-ray photoelectron spectroscopy of carbon present in graphene oxide (GO), aged graphene oxide (aGO), and plasma treated aged graphene oxide (pGO).

	$N_{C(sp^2)}$ (%)	$N_{C(sp^3)}$ (%)	N_{C-O} (%)	$N_{C=O}$ (%)	$N_{O-C=O}$ (%)
GO	37.1	14.0	28.5	14.1	6.3
aGO	45.3	13.1	21.7	13.7	6.1
pGO	51.5	12.7	17.2	10.3	8.3

From the XPS analysis, the following conclusions can be derived. First, the ageing causes the loss of oxygen-related carbon species. Second, a trivial increment in the relative content of –COOH is observed after plasma treatment. The compositional analysis reveals that there are minor compositional changes occurring to GO due to the ageing and after its plasma treatment. Therefore, we further investigated the surface potential and size distribution of these samples in water using DLS. The following outcome can be found in the XPS results. The ageing of GO is exhibited by the loss of oxygen-related carbon species. The O_2 plasma restores the –OH functional groups and reverses the ratio of (C–OH+O–C=O)/C=O back to 2.5, which is comparable to the value in GO. The specific ratio of these functional groups is necessary for synthesizing stable hydrogels via the hydrothermal process.

3.4.2 Stability and size distribution in graphene oxide suspension

As the hydrothermal process is started with an aqueous solution of GO, the stability of GO suspensions in water is crucial for preparing stable 3D graphene hydrogels. Previous research has shown that the GO chemical composition can strongly affect its dispersibility in water. From a general point of view, GO is essentially a graphene sheet with phenol, hydroxyl and epoxide groups on the basal plane and carboxylic acid at the edges.[36,37] These carboxylic groups –COOH are attributed to the good dispersity of GO in water.[36,37] Whereas the basal plane consists of hydrophobic polyaromatic islands of unoxidized benzene rings.[38,39] Therefore, GO should be perceived as an amphiphile with hydrophilic edges and a sizable part of the hydrophobic basal plane. Also, the nature of GO in an aqueous solution is controlled via the content of the functional group.[40] In recent years, it has also been known that the formation of a stable GO aqueous solution should be

attributed to the electrostatic repulsion rather than just the hydrophilicity of GO, as previously presumed.[37,41] That is why the fresh and highly oxidized GO is well-soluble in water (Figure 3.8a). However, when there is a loss of oxygen caused by the ageing, the stability of aGO suspensions is lost, as shown in Figure 3.8a. This is because there is a relative increment in the hydrophobic unoxidized graphene areas on the base plane of aGO, which reduce the contact area of the aGO structures with water and lead to the agglomeration and sedimentation of the aGO flakes in water.[42]

DLS and zeta potential measurements (Figure 3.8) reveal that the flake size and the zeta potential of the GO, aGO, and pGO suspensions in water are significantly different. The DLS analysis used in this work is based on the model which considers spherical particles instead of planar structures (GO consists of graphene planes). The size of the GO in an aqueous (H_2O) solution depends upon a variety of chemical species around its environment, such as pH,[42] ionic strength,[43] graphene structures (like bending, scrambling/scrolling, and folding).[35]

The size distribution spectrum of the samples is shown in Figure 3.8b. GO sample shows a broad distribution of sizes with two peaks. The majority of GO flake sizes center at ~ 3000 nm as the relative intensity of this peak is much greater than another peak center at ~ 330 nm. It is to be noted that the dispersed solution from the GO was stable even after 7 days. The aGO sample shows two broad merged peaks (Figure 3.8b) with a small decrease in the size of the flakes compared with GO samples. However, the dispersed solution made from the aGO was not stable, and sedimentation started within a few hours. This is possibly due to a minor change in the relative content of the oxygen functional groups, as revealed by the XPS analysis.

After plasma treatment, a sharp drop in the sizes of flakes is noticed. A broad and intense peak is observed centered at ~ 590 nm and minor peaks at 110 nm and 5.5 μm (Figure 3.8b). This suggests that the plasma helped in reducing the sizes of the flakes. This effect of plasma can be understood by the fact that the plasma contains very reactive and energetic species. These species have sufficient energy to break the aGO flakes into a smaller size. A similar phenomenon has also been observed during the ultrasonication of the GO solution.[35] The plasma helped in decreasing the GO flake size, which means that a higher edge-to-area ratio was produced in pGO samples. Since the density of the functional groups is expected to be higher at the edges of the flakes,[44,45] there should be more electrostatic repulsion between the GO flakes and thus a more stable dispersed

solution in the pGO than in the aGO. It is to be noted that the pGO dispersed solution remained stable even after the 7 days, similarly to the GO solution.

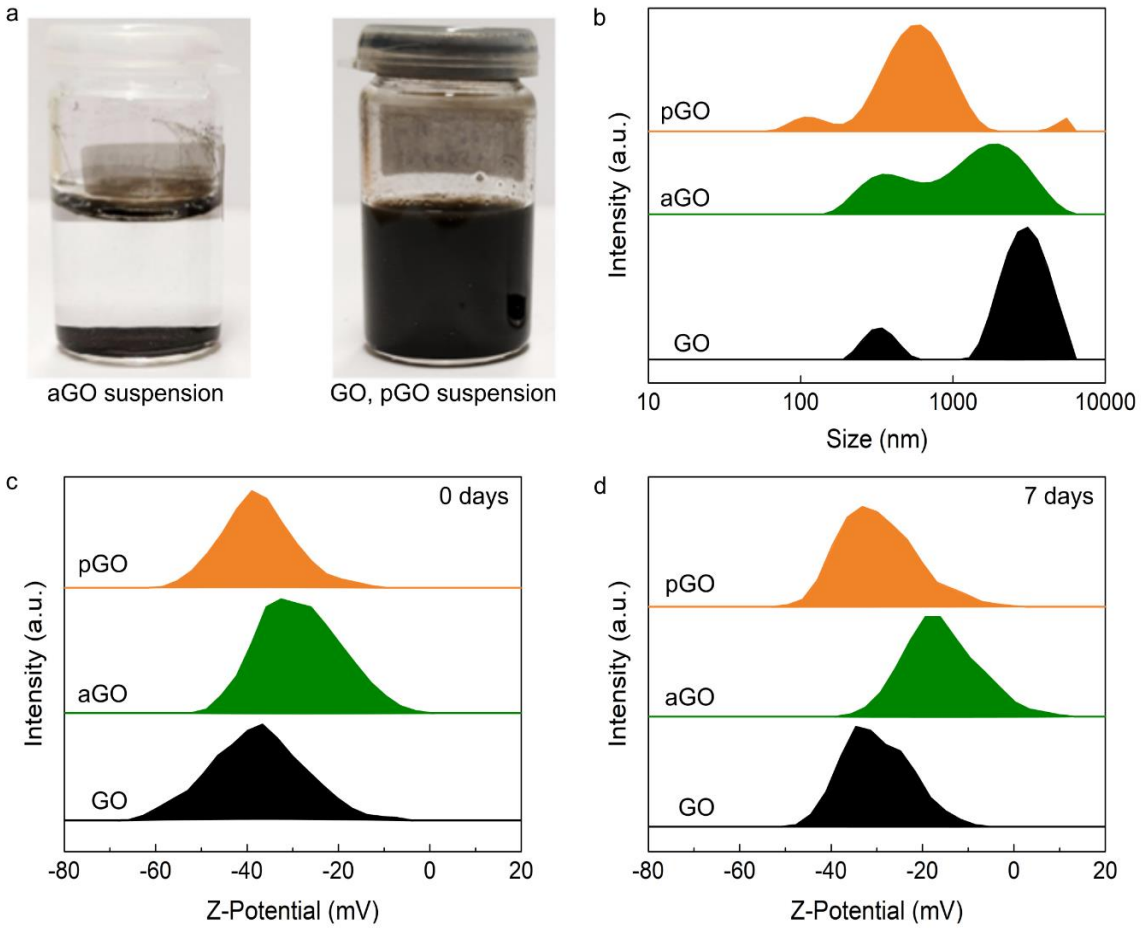

Figure 3.8 Stability and size distribution in graphene oxide suspension. Graphene oxide (GO), aged graphene oxide (aGO), and plasma treated aged graphene oxide (pGO) suspension characterization. (a) Actual photograph, (b) Flake size distribution shown in logarithmic scale, (c) and (d) Zeta potential measured immediately and after 7 days of GO, aGO, and pGO.

The zeta potential of GO solution was measured right after mixing GO with water and a week after the preparation of GO suspensions. Generally, the zeta potential smaller than -30 mV is considered sufficient for the preparation of a stable GO solution in neutral pH aqueous solutions.[37] The fresh GO solution exhibits a broad distribution of zeta potentials with peak boundaries from -66 mV to -7 mV and a center at -39 mV (Figure 3.8c). After a week, the peak center of the zeta potential of the GO shifted to -31 mV (Figure 3.8d). The

aGO solution measured right after mixing it with water also shows a broad zeta potential distribution with peak boundaries from -50 mV to -2 mV and a center at -30 mV. After keeping aGO suspension for a week, the peak center upshifted to -18 mV. It is shown that the plasma treatment was able to downshift the zeta potential peak of the pGO solution and restore it to the negative zeta potentials similar to the fresh GO solution. The pGO has peak boundaries from -58 mV to -12 mV and a center at -39 mV. After a week, the zeta potential peak center of the pGO solution again upshifted to -31 mV, demonstrating a comparable zeta potential distribution to the fresh GO suspension. This improvement in the surface charge and stability can be attributed to the smaller flake size and restoration of ratios of carboxylic and hydroxyl groups, as indicated in the XPS analysis. These functional groups help in restoring more negative zeta potential by the ionization of the oxygen-containing functional groups into negatively charged radicals.[34,35]

3.4.3 Removing defects from graphene aerogel

Defects usually worsen the physical properties of materials, especially graphene (as discussed in Chapter 1). The intrinsic defects, including lattice/topological defects and edge defects, are presented in the rGA due to the loss of oxygen functional groups.[46] The majority of the defects are inherited from the starting GO material because it contains a high density of sp^3 hybridized carbon bonds due to the adsorbed oxygen species.[47] The presence of a high number of defects in the rGA results in poor electrical conductivity, structural instability, and fragileness of the 3D structure. In this thesis, high-temperature annealing is investigated with the aim of repairing defects presented in the freshly prepared rGA (Figure 3.9). The effect of different annealing temperatures from 400 to 2700 °C is studied. The number of defects and crystallite size in the annealed samples are investigated using XPS and Raman spectroscopy.

The rGA samples were gradually annealed at 400, 750, 1000, 1300, and 2700 °C and compared with the rGA sample before annealing. The deconvolution of the XPS C 1s and O 1s spectra is shown in Figure 3.10c,d. The C 1s signal includes sp^2 and sp^3 hybridized carbon atoms peaks and peaks corresponding to various oxygen species, such as C–O, C=O, and COOH. The rGA sample is composed of 89% of carbon and 11% of oxygen. Annealing of the GA at 400 °C shows almost no change in the composition. Once the temperature of annealing is increased to 750 °C, the relative content of carbon is increased to 96%, and oxygen is decreased to 4%. When the aerogel is further annealed

at 1000 °C, the carbon and oxygen content remains almost the same as in the GA annealed at 750 °C. A significant reduction of oxygen is observed after 1300 °C annealing. The standard GA sample annealed at 1300 °C (according to the SOP) has > 99.4% of carbon and < 0.6% of oxygen content. The oxygen is completely removed from the sample when the GA is annealed at 2700 °C.

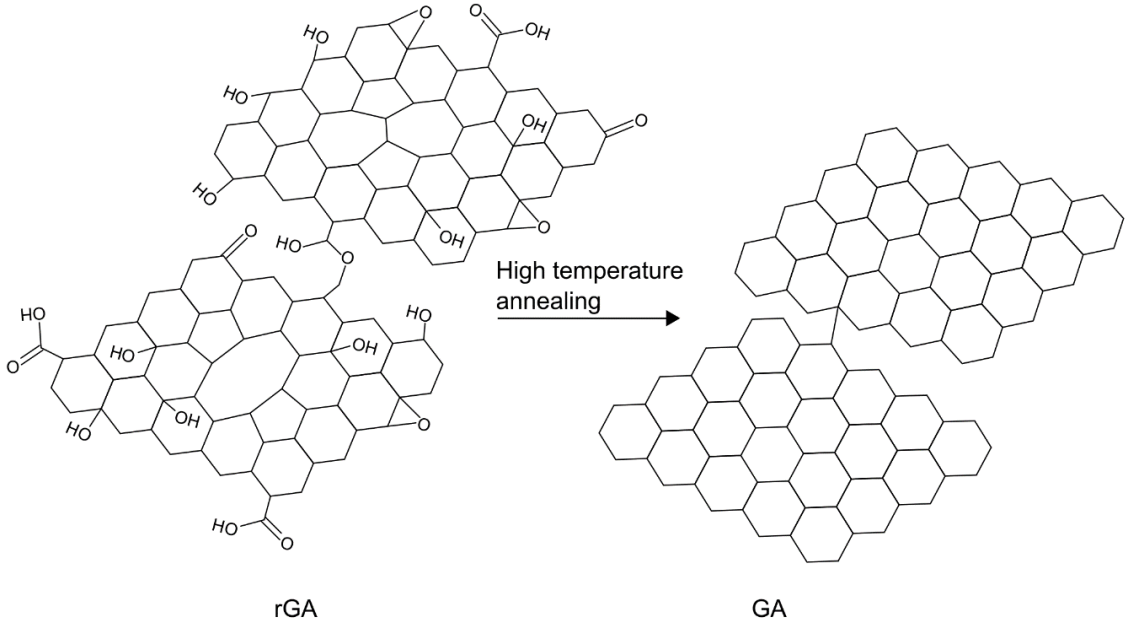

Figure 3.9 Schematic of removing residual defects from reduced graphene oxide aerogel (rGA) by high temperature annealing.

It is well known that the oxygen species bonds have different binding energy to graphene. Therefore, different oxygen species are removed from the graphene at different temperatures during annealing. A previous study of Acik et al. has reported that the theoretical binding energy for oxygen species desorption ranges from 1.5 to 8 eV.[28] Hydroxyl groups desorb at 1.5 eV, epoxide at 3.1 eV, carboxyl at 5.8 eV, and ketonic at 8.0 eV.[48] The number of particular oxygen species determined from XPS at a specific annealing temperature in the GA samples is summarized in Table 3.3. The experimentally obtained values are in line with the sequence of the theoretical binding energies. First are annealed hydroxyl groups. As a result, the GA sample annealed to 1000 °C contains mainly carboxyl and ketonic species. After 1300 °C annealing, all the oxygen species are removed from the sample.

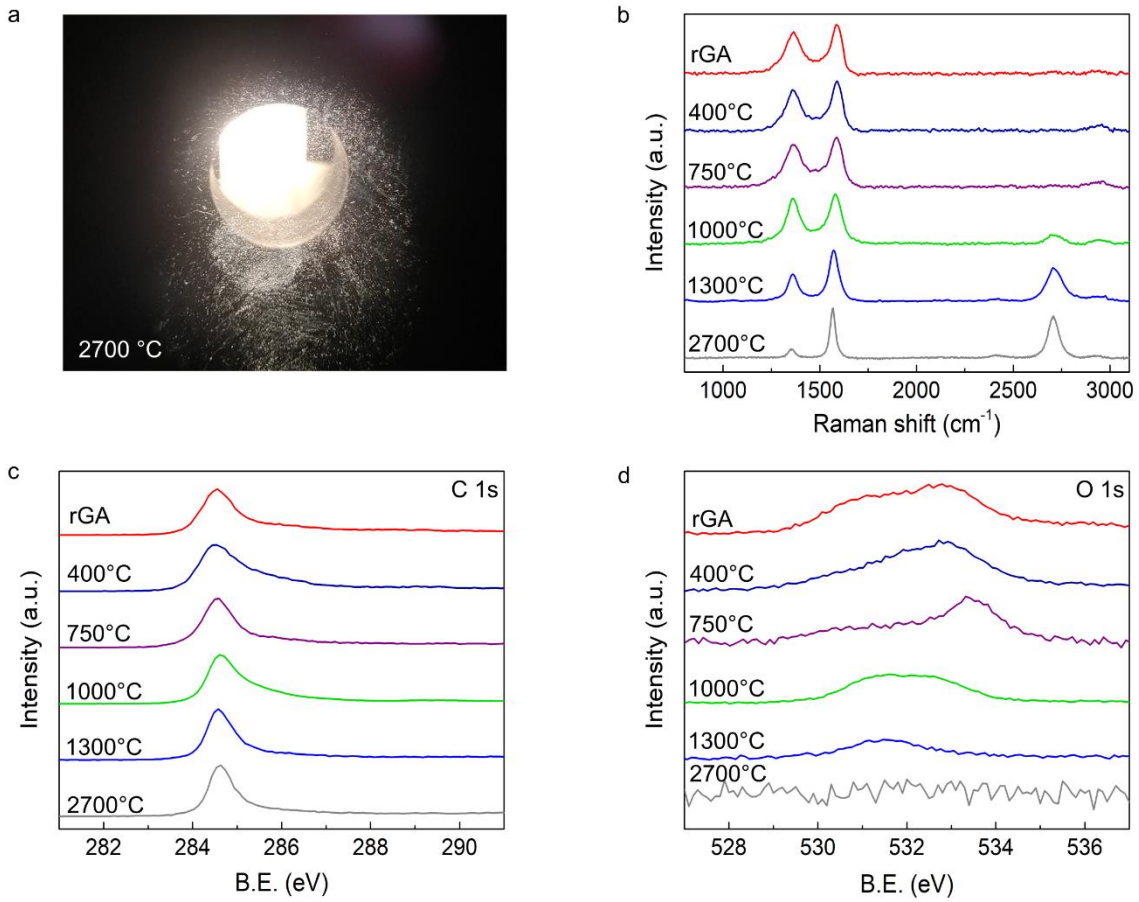

Figure 3.10 Raman and X-ray photoelectron spectroscopy analysis of the varying annealing temperature of graphene aerogels (GA) compared to the non-annealed reduced graphene oxide aerogel (rGA). (a) Photograph of the furnace heated to 2700 °C. (b) Raman spectra and X-ray photoelectron spectroscopy of (c) C 1s and (d) O 1s spectra of rGA samples annealed at 400, 750, 1000, 1300, and 2700 °C.

Simultaneously with the XPS analysis, the Raman spectra of the annealed GA samples were taken (Figure 3.10b-d). The Raman spectra show the evolution of the D, G, and 2D bands of graphene. With increasing annealing temperature, there is observed an increase in the 2D band, a decrease in the D band, and a sharpening of the G band. The GA sample annealed to 2700 °C shows the best crystal quality graphene and the lowest density of defects of all the samples. The density of defects and the crystallite size (L_a) in the samples are estimated from the ratio of the intensity of the D to G peaks using the following equation defined by Cancado et al.[49]

$$L_a = 2.4 \times 10^{-10} \lambda^4 \left(\frac{I_D}{I_G}\right),$$

where λ is the wavelength of the laser used in the Raman measurement, and I_D and I_G are the intensities of the D and G peaks, respectively. The density of defects n_d is calculated using the following equation[50]

$$n_d = \frac{2.4 \times 10^{22}}{\lambda^4}\left(\frac{I_D}{I_G}\right).$$

Table 3.3 The compositional (N_C, N_O) and quantitative ($N_{C(sp^2)}$, $N_{C(sp^3)}$, N_{C-O}, $N_{C=O}$, $N_{O-C=O}$) analyses of X-ray photoelectron spectroscopy of graphene aerogels annealed at different temperatures.

Temperature (°C)	N_C (%)	N_O (%)	$N_{C(sp^2)}$ (%)	$N_{C(sp^3)}$ (%)	N_{C-O} (%)	$N_{C=O}$ (%)	$N_{O-C=O}$ (%)
0	89	11	67	16	9	4.5	4
400	90	10	66	18	8.5	4	3.5
750	95.8	4	69	20	5.5	3.5	2
1000	96	4	69	21	4.5	3	2
1300	> 99.4	< 0.6	71	23	0.6	-	-
2700	100	0	79	21	-	-	-

Simultaneously with the XPS analysis, the Raman spectra of the annealed GA samples were taken (Figure 3.10b-d). The Raman spectra show the evolution of the D, G, and 2D bands of graphene. With increasing annealing temperature, there is observed an increase in the 2D band, a decrease in the D band, and a sharpening of the G band. The GA sample annealed to 2700 °C shows the best crystal quality graphene and the lowest density of defects of all the samples. The density of defects and the crystallite size (L_a) in the samples are estimated from the ratio of the intensity of the D to G peaks using the following equation defined by Cancado et al.[49]

$$L_a = 2.4 \times 10^{-10} \lambda^4 \left(\frac{I_D}{I_G}\right),$$

where λ is the wavelength of the laser used in the Raman measurement, and I_D and I_G are the intensities of the D and G peaks, respectively. The density of defects n_d is calculated using the following equation[50]

$$n_d = \frac{2.4 \times 10^{22}}{\lambda^4}\left(\frac{I_D}{I_G}\right).$$

For the non-annealed rGA, the crystallite size is found to be around 10 nm, and the density of defects is roughly 2.9×10^{11} cm^{-2}. The D to G peak ratio does not change when the rGO

is annealed at temperatures lower than 1000 °C. Therefore, the crystallite size and defect density remain almost constant. A slight decrease of the defect density is observed along with the broadening of the G peak after exceeding 1300 °C. This effect is most likely caused due to the removal of oxygen species and the annealing of defects and ripples in graphene flakes in the GA. In comparison with lower annealing temperatures, the standardly annealed GA sample (1300 °C) shows a significant decrease in the D peak and the D to G peak ratio. Consequently, the defect density is decreased to 2.1 × 10^{11} cm^{-2}, and the crystal size is doubled to 20 nm. The sample annealed at 2700 °C is characterized by a sharp 2D peak, which has the same intensity as the G peak, and a major reduction of the D peak. This extreme temperature annealing results in a 6 times decrease in the defect density and, at the same time, almost a 6 times increase in crystal size compared with the non-annealed rGA.

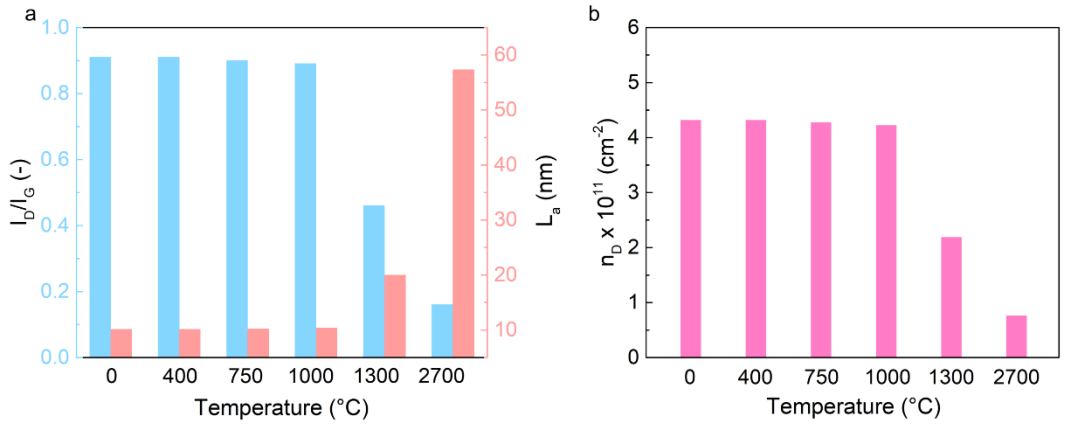

Figure 3.11 The analysis of the structural properties depending on the annealing temperature of graphene aerogels (GA). (a) Crystallite size (L_a) and (b) density of defects (n_D) determined from the Raman spectra using the method of Cancado et. al.[49]

3.5 Conclusions

A template-free synthesis method of covalently cross-linked 3D graphene aerogels has been developed using hydrothermal synthesis, freeze-drying, and high-temperature annealing. The structure and composition of the graphene materials have been carefully investigated at each step of the three-step synthesis method. The key steps for the successful synthesis have been determined. They include mainly a high-quality source GO material, preparation of stable GO suspensions in water, and high-temperature annealing > 1300 °C. The synthesis parameters have been optimized, and the SOP has

been developed. The SOP enables fabricating of centimeter-sized GA samples of high crystal quality with exceptional mechanical and electrical properties. These GA samples are used in the rest of the thesis.

Moreover, the effects of the ageing of the starting GO material of the hydrothermal synthesis have been investigated. The ageing of GO causes a change in the relative composition of oxygen functional groups. This change is responsible for decreasing the surface charge of GO and agglomeration of GO flakes in water solution. As a result of these changes, using aGO for the GA synthesis leads to the formation of unstable and crumbled-like hydrogels/aerogels. The use of O_2 plasma treatment of the aged GO samples has helped in reversing the effect of the ageing, and enabled the preparation of stable and compact hydrogels/aerogels. The main role of the plasma treatment is observed in the improved stability and dispersity of the pGO solutions due to more negative zeta potential, smaller flake sizes, and restoration of ratios of carboxylic and hydroxyl groups.

The effects of different annealing temperatures of rGA have been investigated. Low-temperature annealing under 400 °C removes only a few types of residual oxygen species from the graphene aerogels. With the rising temperature, the number of removed oxygen content is increased, and the complete removal takes place at 1300 °C. Even though all the oxygen species are removed, the graphene structure still contains a large amount of intrinsic structural defects. These defects are removed by annealing at extremely high temperatures (2700 °C). It has been found that annealing temperature > 1300 °C is necessary not only for the complete removal of oxygen species from graphene aerogels but also for the formation of the covalent cross-linking of individual graphene sheets in the aerogels.

References

1. Sun, Z., Fang, S. & Hu, Y. H. 3D Graphene Materials: From Understanding to Design and Synthesis Control. *Chem. Rev.* **120**, 10336–10453 (2020).
2. Chen, Z. *et al.* Three-dimensional flexible and conductive interconnected graphene networks grown by chemical vapour deposition. *Nature Materials* **10**, 424–428 (2011).
3. Zhu, C. *et al.* Highly compressible 3D periodic graphene aerogel microlattices. *Nature Communications* **6**, 6962 (2015).

4. Li, C. & Shi, G. Three-dimensional graphene architectures. *Nanoscale* **4**, 5549–5563 (2012).
5. Xu, Y., Shi, G. & Duan, X. Self-Assembled Three-Dimensional Graphene Macrostructures: Synthesis and Applications in Supercapacitors. *Acc. Chem. Res.* **48**, 1666–1675 (2015).
6. Chen, Z., Jin, L., Hao, W., Ren, W. & Cheng, H.-M. Synthesis and applications of three-dimensional graphene network structures. *Materials Today Nano* **5**, 100027 (2019).
7. Xu, Y., Sheng, K., Li, C. & Shi, G. Self-Assembled Graphene Hydrogel via a One-Step Hydrothermal Process. *ACS Nano* **4**, 4324–4330 (2010).
8. Bi, H. *et al.* Low Temperature Casting of Graphene with High Compressive Strength. *Advanced Materials* **24**, 5124–5129 (2012).
9. Sun, H., Xu, Z. & Gao, C. Multifunctional, Ultra-Flyweight, Synergistically Assembled Carbon Aerogels. *Advanced Materials* **25**, 2554–2560 (2013).
10. Worsley, M. A. *et al.* High Surface Area, sp2-Cross-Linked Three-Dimensional Graphene Monoliths. *J. Phys. Chem. Lett.* **2**, 921–925 (2011).
11. Hou, W.-C. *et al.* Photochemical Transformation of Graphene Oxide in Sunlight. *Environ. Sci. Technol.* **49**, 3435–3443 (2015).
12. Acik, M. *et al.* The Role of Oxygen during Thermal Reduction of Graphene Oxide Studied by Infrared Absorption Spectroscopy. *J. Phys. Chem. C* **115**, 19761–19781 (2011).
13. Zhang, W., Luo, Q., Duan, X., Zhou, Y. & Pei, C. Nitrated graphene oxide and its catalytic activity in thermal decomposition of ammonium perchlorate. *Materials Research Bulletin* **50**, 73–78 (2014).
14. Shams, M. *et al.* Influence of functional groups on the degradation of graphene oxide nanomaterials. *Environ. Sci.: Nano* **6**, 2203–2214 (2019).
15. Bai, H. *et al.* Insight into the Mechanism of Graphene Oxide Degradation via the Photo-Fenton Reaction. *J. Phys. Chem. C* **118**, 10519–10529 (2014).
16. Holt, B. D., Arnold, A. M. & Sydlik, S. A. In It for the Long Haul: The Cytocompatibility of Aged Graphene Oxide and Its Degradation Products. *Advanced Healthcare Materials* **5**, 3056–3066 (2016).
17. Jiang, L. & Fan, Z. Design of advanced porous graphene materials: from graphene nanomesh to 3D architectures. *Nanoscale* **6**, 1922–1945 (2014).
18. Pei, S. & Cheng, H.-M. The reduction of graphene oxide. *Carbon* **50**, 3210–3228 (2012).

19. Banhart, F., Kotakoski, J. & Krasheninnikov, A. V. Structural Defects in Graphene. *ACS Nano* **5**, 26–41 (2011).
20. Cheng, Y. *et al.* Enhanced mechanical, thermal, and electric properties of graphene aerogels via supercritical ethanol drying and high-temperature thermal reduction. *Sci Rep* **7**, 1439 (2017).
21. Guo, X. *et al.* Free-standing graphene aerogel with improved through-plane thermal conductivity after being annealed at high temperature. *Journal of Colloid and Interface Science* **608**, 2407–2413 (2022).
22. Chen, W. & Yan, L. In situ self-assembly of mild chemical reduction graphene for three-dimensional architectures. *Nanoscale* **3**, 3132–3137 (2011).
23. Zhang, X. *et al.* Mechanically strong and highly conductive graphene aerogel and its use as electrodes for electrochemical power sources. *J. Mater. Chem.* **21**, 6494–6497 (2011).
24. Ferrari, A. C. Raman spectroscopy of graphene and graphite: Disorder, electron–phonon coupling, doping and nonadiabatic effects. *Solid State Communications* **143**, 47–57 (2007).
25. Xiang, C. *et al.* Graphene Nanoribbons as an Advanced Precursor for Making Carbon Fiber. *ACS Nano* **7**, 1628–1637 (2013).
26. Gao, Z. *et al.* Graphene reinforced carbon fibers. *Science Advances* **6**, eaaz4191 (2020).
27. El-Hossary, F. M., Ghitas, A., El-Rahman, A. M. A., Shahat, M. A. & Fawey, M. H. The effective reduction of graphene oxide films using RF oxygen plasma treatment. *Vacuum* **188**, 110158 (2021).
28. Acik, M. *et al.* Unusual infrared-absorption mechanism in thermally reduced graphene oxide. *Nature Materials* **9**, 840–845 (2010).
29. Acik, M. *et al.* The Role of Oxygen during Thermal Reduction of Graphene Oxide Studied by Infrared Absorption Spectroscopy. *The Journal of Physical Chemistry C* **115**, 19761–19781 (2011).
30. Huang, H.-H., De Silva, K. K. H., Kumara, G. R. A. & Yoshimura, M. Structural Evolution of Hydrothermally Derived Reduced Graphene Oxide. *Scientific Reports* **8**, 6849 (2018).
31. García-Bordejé, E., Víctor-Román, S., Sanahuja-Parejo, O., Benito, A. M. & Maser, W. K. Control of the microstructure and surface chemistry of graphene aerogels via pH and time manipulation by a hydrothermal method. *Nanoscale* **10**, 3526–3539 (2018).

32. Li, C. *et al.* Effect of long-term ageing on graphene oxide: structure and thermal decomposition. *Royal Society Open Science* **8**, (2021).
33. Kim, H. G. *et al.* Analysis of Defect Recovery in Reduced Graphene Oxide and Its Application as a Heater for Self-Healing Polymers. *ACS Applied Materials & Interfaces* **11**, 16804–16814 (2019).
34. Li, M. *et al.* The evolution of surface charge on graphene oxide during the reduction and its application in electroanalysis. *Carbon* **66**, 302–311 (2014).
35. Gonçalves, G. *et al.* Breakdown into nanoscale of graphene oxide: Confined hot spot atomic reduction and fragmentation. *Scientific Reports* **4**, 6735 (2015).
36. Lerf, A., He, H., Forster, M. & Klinowski, J. Structure of Graphite Oxide Revisited. *The Journal of Physical Chemistry B* **102**, 4477–4482 (1998).
37. Li, D., Müller, M. B., Gilje, S., Kaner, R. B. & Wallace, G. G. Processable aqueous dispersions of graphene nanosheets. *Nature Nanotechnology* **3**, 101–105 (2008).
38. Nakajima, T. & Matsuo, Y. Formation process and structure of graphite oxide. *Carbon* **32**, 469–475 (1994).
39. Cai, W. *et al.* Synthesis and Solid-State NMR Structural Characterization of 13 C-Labeled Graphite Oxide. *Science* **321**, 1815–1817 (2008).
40. Kim, J. *et al.* Graphene Oxide Sheets at Interfaces. *Journal of the American Chemical Society* **132**, 8180–8186 (2010).
41. Stankovich, S. *et al.* Synthesis of graphene-based nanosheets via chemical reduction of exfoliated graphite oxide. *Carbon* **45**, 1558–1565 (2007).
42. Whitby, R. L. D. *et al.* pH-driven physicochemical conformational changes of single-layer graphene oxide. *Chemical Communications* **47**, 9645 (2011).
43. Zangmeister, C. D., Ma, X. & Zachariah, M. R. Restructuring of Graphene Oxide Sheets into Monodisperse Nanospheres. *Chemistry of Materials* **24**, 2554–2557 (2012).
44. Luo, J. *et al.* Graphene Oxide Nanocolloids. *Journal of the American Chemical Society* **132**, 17667–17669 (2010).
45. Szabo, T., Maroni, P. & Szilagyi, I. Size-dependent aggregation of graphene oxide. *Carbon* **160**, 145–155 (2020).
46. Banhart, F., Kotakoski, J. & Krasheninnikov, A. V. Structural Defects in Graphene. *ACS Nano* **5**, 26–41 (2011).
47. Pei, S. & Cheng, H.-M. The reduction of graphene oxide. *Carbon* **50**, 3210–3228 (2012).

48. Acik, M. *et al.* Unusual infrared-absorption mechanism in thermally reduced graphene oxide. *Nature Mater* **9**, 840–845 (2010).
49. Balandin, A. A. *et al.* Superior Thermal Conductivity of Single-Layer Graphene. *Nano Lett.* **8**, 902–907 (2008).
50. Sharma, R., Chadha, N. & Saini, P. Determination of defect density, crystallite size and number of graphene layers in graphene analogues using X-ray diffraction and Raman spectroscopy. *IJPAP Vol.55(09) [September 2017]* (2017).

4 Mechanical properties of graphene aerogels

4.1 Introduction

Elasticity is the ability of a material to recover its original size and shape when the material is no longer under the influence of deformation forces. Materials that can withstand significant elastic strains and prevent permanent deformation under load have a significant impact on daily life. They have a wide range of applications in the construction industry, automotive, biotechnology, electronics, and aerospace industries. These materials open the possibility of the fabrication of tension/pressure-bearing components, advanced springs, sensors, flexible electronic devices, and wear-resistant applications. Researchers have been looking for more durable elastic materials that can withstand heavier mechanical loads with little plastic deformation as part of their ongoing search for better materials.[1,2] However, a large elastic modulus typically tends to decrease the compressibility and extensibility of a material[3]. Different techniques for adjusting the atomic level and microstructure of elastic materials have been thoroughly studied to improve the resilience of materials.[4–7] Recent progress has demonstrated that superelasticity and intriguing mechanical properties can be obtained from the structure of porous and cellular materials,[1,8] offering a practical means of extending the elastic strain range in compression beyond the small deformation limit. However, the tensile strength and modulus of the porous materials reported so far have significantly degraded.[9] On the other hand, highly elastic materials made of silicone and polymeric rubbers have low yield strengths under compression.[10] Although biological materials exhibit such a mechanical behavior, high strength materials that could withstand both large elastic deformation in compression and tension have not yet been developed.[3] This necessitates the development of intelligent materials that combine high-strength, variable density, large-strain elasticity, and high porosity in a single material.

Here, the large compressive and tensile elasticity is exhibited by the GA even without significant degradation in the specific strength of the material. Additionally, the largest range of superelasticity and specific compressive yield strength is seen in a material so far are demonstrated by the GA. It is further demonstrated that the superelastic behavior

of the GA is allowed due to the high bending flexibility of individual graphene sheets in the pore walls of the GA, which buckle similarly to origami. As a result, when gradually deformed, the GA exhibits variable density, electrical conductivity, and stiffness. More surprisingly, the GA displays unique vibration damping properties, which allow superfast damping within nanoseconds.

4.2 Experiments

The static compression experiments were performed using two different approaches. The mechanical press was used for experiments where the applied pressure did not exceed 20 MPa using GA samples with sizes in the mm range. On the other hand, the diamond anvil cell was used for compression under pressures exceeding 1 GPa. The GA samples in a diamond anvil cell are maximally 200 × 200 μm with a thickness of 50 μm. In both approaches, the strain was determined using an optical microscope.

The static tensile test was done with samples mm big (shoulders 4 × 4 × 3 mm and a thin part 1 × 1 × 2 mm) and specifically shaped. The sample follows the shape (reduced volume in the center) of standard samples used for usual macroscopic tensile testing of common materials, for example, steel.[11]

The dynamic mechanical response of the GA upon the fast mechanical impact was measured using the optical and electrical approaches. The optical approach visualizes the millimeters GA sample hit by a falling metal ball from 30 cm height, where the ball has a mass of 0.02 g and a radius of 1 mm. To visualize the fast movement of the ball as well as the vibrations of the GA, a high-speed camera (Photron Fastcam Mini UX100) with a 40 mm objective at the resulting magnification of 0.7 and framerate of 10000 fps was used.

The electrical approach is based on monitoring the change in voltage of a sample with an oscilloscope (Tektronix TDS 620B). The GA sample with dimensions of 2 × 2 × 2 mm has two electrical contacts at the top and bottom and an insulated metal rod is touching the top contact. The constant current of 0.1-0.3 A (Agilent E3631A) is applied to the GA sample and the change of voltage is induced by the mechanical impact through the vibration of the metal rod.

4.3 Mechanical testing

The mechanical properties of the GA are shown in Figure 4.2c as a function of compressive and tensile strain. Plus and minus signs at the strain values are used to differentiate between elongation and compression. In terms of stress values, the negativity indicates the opposite direction of applied pressure (i.e. compression is positive and elongation is negative). The stress-strain data measurements are a summary of 20 samples measured in the uniaxial compression, 3 samples in the diamond anvil cell, and 2 samples in the uniaxial tension tests. Each of the measured points in the figures represents an average value of 10 load-unload cycles except for the last two points at the breakpoint.

4.3.1 Tensile testing

Almost 100 GA samples were subjected to tensile testing. However, only a small percent of the measurements enabled us to determine the real tensile strength of the covalently cross-linked GAs. The statistics of the outcomes are shown in Table 4.1 and the most typical causes of failure are visualized in Figure 4.1. The most usual failure was due to cracks at the interface of glue and one of the shoulders, which appeared under 10% of strain. Choosing the right glue for attaching millimeters of the GA parts to withstand high pressure is very difficult. The common failure was also the presence of inner cracks showing under 8% of strain. These inner cracks in the GA are naturally presented due to the type of synthesis or induced at the mechanical shaping of the sample. There was also one case when the glue started stretching at 27% of the GA strain. In 6 cases, the surface cleavage cracks played a role when the sample cracked at the transition between the shoulder and thin part.

Table 4.1 Statistics of the performed tensile tests of different graphene aerogel (GA) specimens.

Sample name	Number of tests	Cause of failure	Max. strain (%)
GA contacts	47	Edge of glue	0-10
GA inner cracks	39	Inner cracks	0-8
GA epoxy	1	Glue stretching	27
GA surface cracks	6	Surface cracks	10-40
GA	2	Graphene aerogel	65-67

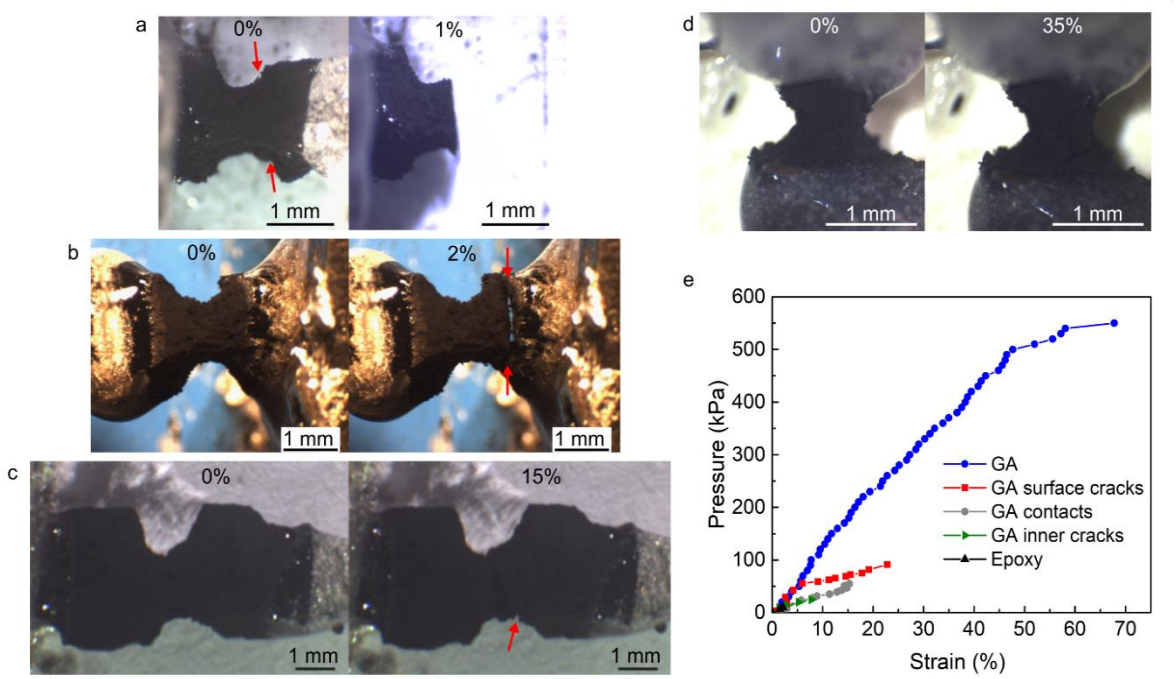

Figure 4.1 Optical images of graphene aerogel (GA) specimens under tensile tests demonstrating failure caused by (a) inner defects/cracks, (b) edges of the epoxy glue, (c) surface cleavage cracks, and (d) ultimate strength of the material. (e) Tensile stress-strain curves of GA specimens which failed due to (a-d).

4.3.2 Mechanical properties

The stress-strain curve of the GA subjected to the compression-tension test shows a complex nonlinear behavior with a steep rise at high pressures (< −60% strain). The elasticity of the GA behavior is observed in a wide range of strain deformation with limits of -92% in compression and 68% in tension. Once the load is removed, the GA completely and instantly recovers the sample size and shape. The maximum elastic yield strength in compression and tension is 4.5 GPa and 0.6 MPa. These maximum values of stress in compression and tensile were assessed from the reversible shift of the G peak in the Raman spectrum and from usual optical observation (see Figure 4.2d). The shift of the G peak position gives an opportunity to estimate the number of layers in the GA by comparing it with previous Raman measurements of strained graphene.[12] The comparison is shown in Table 4.2, where the shift of the G peak position with pressure in the GA is between the peak shifts of the bi and few-layer graphene. On the base of this observation, the GA is composed of an average of 4 layers.

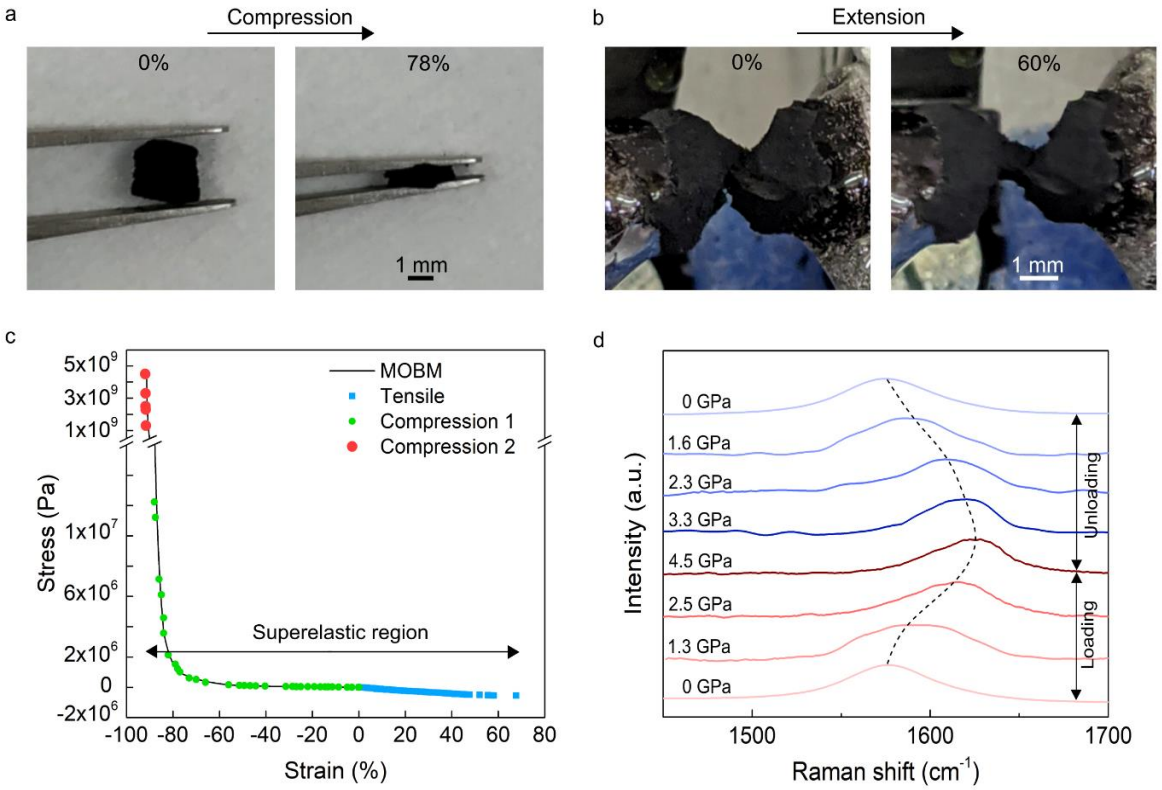

Figure 4.2 Mechanical properties of the graphene aerogel (GA). (a),(b) Optical images of the GA subjected to compressive (a) and tensile (b) stress. (c) The stress-strain curve for compressive and tensile mechanical deformation of the GA. (d) Raman spectra of the GA show the reversible shift of the G peak with applied compressive stress up to 4.5 GPa. properties of graphene aerogel.

Table 4.2 Analysis of the Raman G band of different free-standing graphene materials under high pressure.

Sample	Raman G peak position (cm^{-1})						Ref
	0 Pa	1.3 GPa	2.3 GPa	2.5 GPa	3.3 GPa	4.5 GPa	
GA	1576	1596	1610	1611	1617	1621	**This work**
Monolayer graphene	1583	1610	1624	1625	1634	-	[12]
Bilayer graphene	1582	1603	1617	1620	1630	-	[12]
Few-layer graphene	1582	1593	1601	1602	1606	-	[12]
Graphite	1581	1586	1590	1587	1592	-	[12]

Calculating the area under the stress-strain curve gives the modulus of resilience. The modulus of resilience of the GA is 2.3×10^7 J.m^{-3} in tension and 3.2×10^9 J.m^{-3} in compression. Relating the maximum yield strengths to the density of GA brings the specific strength of 770 GPa.cm^3.g^{-1} in compression and 0.1 GPa.cm^3.g^{-1} in tension. The graph comparing specific strength in compression and tension of the GA with other materials is shown in Chapter 1 in Figure 1.3. The graph compares the usual materials such as steel, polymers, rubbers, diamond, carbon nanotubes, and graphene to the best GA materials reported in the literature.[13–16] It is found that the specific strength in compression of the presented GA is several orders of magnitude larger than for conventional construction materials and other carbon allotropes. The observed strength of the GA is comparable to graphene and exceeds the maximum values for highly compressible graphene aerogels reported so far.[13] Additionally, the range of elasticity of the GA in tension is much greater than previously reported graphene aerogels.[13] The specific strength in tension is similar to the values for steel, but the GA has an order of magnitude larger elastic strain. The elasticity of the GA remained unchanged after applying more than 5000 compressive loading cycles. This stability test is further described in Chapter 5.

The incredible mechanical properties of the GA raise a question about the type of interconnection between graphene sheets. In Chapter 3, while describing the GA, the hypothesis of the covalent cross-linking of graphene sheets in the GA was mentioned. Here this hypothesis is experimentally proved by the measurement of the high tensile strength of the GA.[16,17] If the GA was not covalently bonded the extremely low sliding resistance of individual flakes stacked one on top of each other would lead to permanent deformation of the GA even at relatively small loads, therefore the GA would not be able to bear such high pressures.[18] The same explanation is used for the highly compressed sample because it is almost impossible that weakly bonded flakes would restore their original position after applying 4.5 GPa. Thus, covalent bonds between graphene flakes must be present in the GA to demonstrate such incredible mechanical properties.

The number of the covalent bonds in the GA responsible for the graphene cross-linking can be estimated from the tensile strength. Due to the high annealing temperature, most likely, the cross-linking is carried out by single (C−C) or double (C=C) carbon-carbon covalent bonds. By assuming the typical rupture force (F_i) of a C−C (or C=C) bond with the length of 1.54 nm (1.33 nm) under stretching 4.1 nN (7.3 nN) and the tensile strength (σ_T) of the GA with a surface area of 0.45 mm^2 (S), the amount of the carbon cross-linking

$n_{\mathrm{C-C}} = \frac{\sigma_{\mathrm{T}} \times S}{F_{\mathrm{i}}}$ in the GA is approximately 1.5 × 10^8 per mm^2 ($n_{\mathrm{C=C}}$ = 3.7 × 10^7 per mm^2).[19] Concerning the total number of carbon atoms in the particular GA flake (5.4 × 10^8 atoms) the number of cross-linking is only 0.3% (0.07%). In reality, there will be a mixture of single and double covalent bonds. Therefore, the real number of cross-links is in the range of 0.07-0.3%. In the ideal case, GA is completely cross-linked and the tensile specific strength approaches the tensile specific strength of graphene (573 GPa.cm^3.g^{-1}).[20] It is also expected that a higher amount of covalent cross-linking in the aerogels could diminish the occurrence of defects in the porous structure.[21]

4.4 Analytical model of compression

4.4.1 Introduction

To understand the unusual mechanical behavior of the GA under compression, a theoretical model of GA compression is necessary. There are currently a few models of graphene aerogel compression available in the literature,[2] but none of them is suitable for the presented GA. The models, such as the density scaling model, are based on the power scaling of the elastic modulus and yield strength with specific density.[13] However, these models fail at the nonlinear part of the GA stress-strain curve. The nonlinearity in the stress-strain curves in the GA is believed to be due to the covalent cross-linking of graphene in the material.

Before trying other possible known approaches, the deformation of individual pores in the GA is studied experimentally using *in-situ* SEM (Figure 4.3a). It was found during the compression that the pores get gradually deformed until a point (~ 50% strain) when they undergo a collapse and bend into two pores (Figure 4.3a). This observation is used in a Modular Origami Bending model (MOBM), which was developed to describe the measured stress-strain curves of the GA under compression (Figure 4.2c). The MOBM solves the nonlinear stress-strain behavior via approximation of the structure with an array of interconnected spherical springs, which elastically bend and undergo multiple buckle folds as the pressure is increasing (Figure 4.4b). The MOBM can be expressed as

$$\sigma = \sigma_{\mathrm{lin}} + \sigma_{\mathrm{non-lin}} = \frac{l}{A}(k_{\mathrm{lin}} + k_{\mathrm{non-lin}})\varepsilon,$$

where the stress (σ) strain (ε) behavior follows a linear relationship (σ_{lin}) according to Hooke´s law in the first linear region, and a nonlinear relationship ($\sigma_{\mathrm{non-lin}}$) in the second region due to the multiple buckle folding of pores.

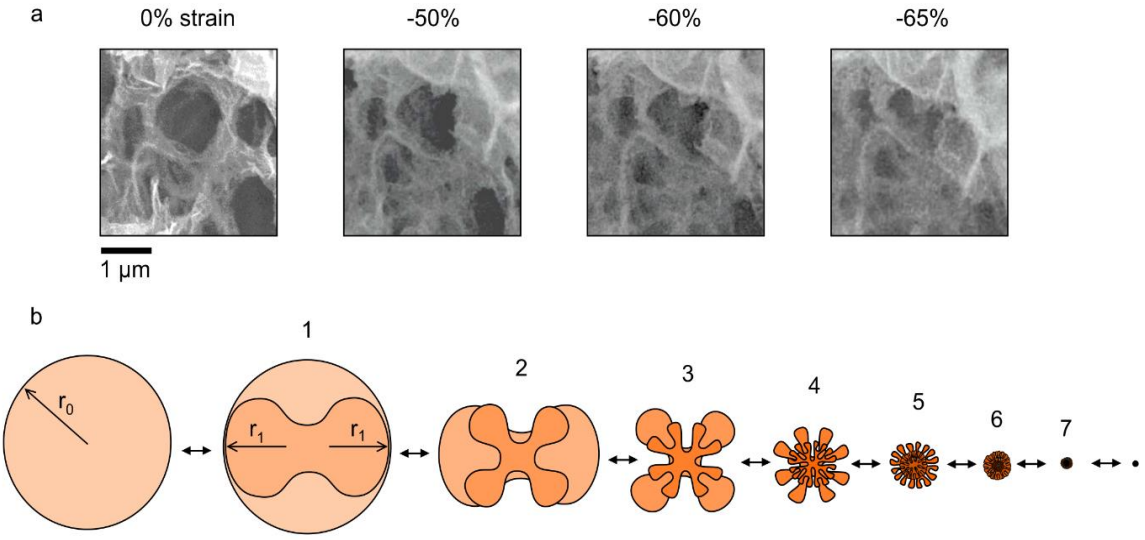

Figure 4.3 Buckling of pores in graphene aerogel (GA). (a) In situ Scanning electron micrographs of GA pores under compression at different strain. (b) Schematic illustration of multiple pore collapse of the GA pores.

4.4.2 Derivation of the Modular Origami Bending model

Hooke´s law in the tensor form is used for the general description of stress-strain

$$\mathbf{F} = \mathbf{KX}$$

Where **F** is a force vector, **K** is a second-order stiffness tensor, and **X** is the displacement vector. As the GA samples are anisotropic with the pressure applied uniaxially (only from one direction), the linear Hooke´s law can be used in linear form

$$F = kx$$

where *k* is a spring constant and x is a uniaxial displacement. Stress σ is defined as the force applied to a cross-sectional area *A* of a material

$$\sigma = \frac{F}{A}$$

Strain ε is the deformation or displacement of material caused by an applied stress

$$\varepsilon = \frac{\Delta l}{l}$$

where *l* is the original length and *Δl* is a change in the length of the material. The elastic modulus *E* of an object can be defined, for relatively small stresses, as the slope of the stress-strain curve

$$E = \frac{\sigma}{\varepsilon} = \frac{Fl}{A\Delta l} = \frac{lk\Delta l}{A\Delta l} = \frac{kl}{A}$$

$$\sigma = \frac{kl}{A}\varepsilon$$

The stress-strain behavior of the GA is divided into two regions in the stress-strain curve: (i) linear and (ii) nonlinear regions described using linear and nonlinear spring constants.

$$\sigma = \frac{l}{A}(k_{\text{lin}} + k_{\text{non-lin}})\varepsilon$$

$$\sigma_{\text{lin}} = \frac{l}{A}(k_{\text{lin}})\varepsilon, \qquad \sigma_{\text{non-lin}} = \frac{l}{A}(k_{\text{non-lin}})\varepsilon$$

A. Structure

As examined in the previous sections, the GA is a 3D structure formed by micrometer pores made of thin graphene layers. These pores behave similarly to elastic springs. For simplicity, the structure is approximated with a 3D lattice of interconnected spherical springs (Figure 4.4b). A single pore is described as a spherical shell with a radius *R*, a thickness *h*, a spring constant *k*, and Poisson´s ratio γ (Figure 4.4a). The pores are interconnected to each other in parallel and series. Regarding these assumptions and approximations, the spring constant of the interconnected springs can be expressed as

In parallel

$$k = \sum_{\text{i}=1}^{N} k_{0\text{i}} = Nk_0$$

In series

$$\frac{1}{k} = \sum_{\text{j}=1}^{M} \frac{1}{k_{0\text{j}}} = \frac{M}{k_0}$$

As an example, the total spring constant *K* of a simple cubic lattice with interconnected pores is

$$k_8 = k_1 + k_2 + k_3 = 3k$$

$$k_9 = k_8 + k_4 + k_5 = 5k$$

$$\frac{1}{K} = \frac{1}{k_9} + \frac{1}{k_6} + \frac{1}{k_7}$$

$$K = \frac{k_9 k_6 k_7}{k_6 k_7 + k_9 k_7 + k_9 k_6} = \frac{5k^3}{11k^2} = \frac{5}{11}k \qquad 3.1$$

From now the GA is considered to consist of the interconnected spherical springs arranged into a simple cubic lattice. A different lattice arrangement leads to a change only in a constant before *k* in equation 3.1.

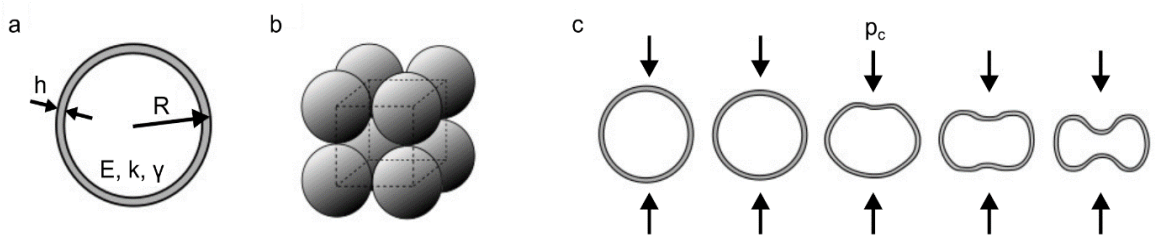

Figure 4.4 Schematic illustration of the graphene aerogel structure based on a thin spherical shell (a) interconnected into a 3D lattice of interconnected springs (b), in which each pore undergoes a buckling collapse at the critical pressure p_c (c).

B. Linear region

The simple Hooke's law is used for the description of the linear region. The GA can be visualized as a block of the elastic material precisely as a linear spring. Its stress (σ) is linearly proportional to its strain (ε) by the spring constant (k_{lin}) as:

$$\sigma_{\text{lin}} = \frac{l}{A}(k_{\text{lin}})\varepsilon$$

If the GA is not fully homogeneous, the linear stress-strain region might consist of more than a single spring constant within the elastic range. This is in line with the experimental observations at the low strain in Figure 4.6a, where the stress-strain curve is composed of two linear segments. These segments are believed to originate either from (i) the internal strain caused by synthesis at high pressure and temperature, or (ii) inhomogeneity of the sample, predominantly due to the internal cracks in the sample, where each part of the sample has a slightly different spring constant.

Let us suppose the pores undergo only small deformations (linear region), the spring constant of a thin wall spherical shell can be expressed analytically as[22]

$$k_0 = \frac{2E}{\sqrt{3(1-\gamma^2)}}\frac{h^2}{R}$$

The total spring constant for all interconnected pores is

$$k_{\mathrm{lin}} = \frac{N_{\mathrm{x}}N_{\mathrm{y}}}{N_{\mathrm{z}}}k_0$$

*w*here $N_{\mathrm{x}}, N_{\mathrm{y}}, N_{\mathrm{z}}$ are the numbers of pores in the x, y, and z-axis.

The final formula for the stress-strain curve in the linear region is

$$\sigma_{\mathrm{lin}} = \frac{l}{A}k_{\mathrm{lin}}\varepsilon = \frac{5}{11}\frac{N_{\mathrm{x}}N_{\mathrm{y}}}{N_{\mathrm{z}}}\frac{2En}{\sqrt{3(1-\gamma^2)}}\frac{h^2}{R}\frac{l}{A}\varepsilon$$

where *n* is a relative Young´s modulus constant in respect to Young´s modulus of few-layer graphene (0.5 TPa). The GA is not formed only by single-layer flakes but there are also few-layered flakes, therefore, the parameter *n* is introduced to take care of an inhomogeneous number of graphene layers. The *n* is less than 1 because *Young´*s modulus of multilayer graphene is lower than a single layer.[23]

C. Nonlinear region

The nonlinear stress-strain behavior of GA starts to take place above the so-called critical pressure (p_c) at which pores start to buckle and fold like origami (Figure 4.3b, 4.4c). The experimental value of p_c is determined from the SEM observation (pressure corresponding to ~ 55% of strain). At this pressure, each pore starts to buckle and fold, creating a number of smaller pores.

The buckling of a spherical shell has been studied since the beginning of the 20th century. The first theory has been proposed by Zoelly,[24] and the first application of this theory has been presented by Koiter.[24,25] Koiter´s theory has been used as the basis for all derived theories by Pogorelov.[26]

D. Buckling

The transformation of pores needs to satisfy mass conservation, once buckling and folding of pores occur. The sum of surface areas of new pores is equaled to the surface area of the original pore

$$S = 2S_1 = 4S_2 = 8S_3 = \cdots = 2^H S_H$$

$$S = 4\pi R^2 = 4\pi R_1^2 m^2 = 4\pi R_2^2 m^4 = 4\pi R_3^2 m^6 = \cdots = 4\pi R_H^2 m^{2H}$$

where R_H is defined as the minimum elastic bending radius of graphene (~ 1 nm for monolayer graphene),[27] and *m* denotes the number of created new pores after buckling. Here, the *m* is considered constant for simplicity. The R_H defines the maximum number of buckling, which for a pore with a 1 μm radius is equaled to 10 (considering the extreme situation of buckling into exactly 2 pores). The number of buckled pores of thin spherical shells has been found experimentally to vary between 2 and 3.[28] The MOBM assumes that *m* represents the average number of buckling within the GA.

E. Critical pressure

The threshold pressure above which the pores lose their convex spherical shape and transform to a concave cup-like shape is called the critical pressure. It is reached as the work done by the external pressure equals the deformation energy.[29]

$$W = \iint_G p h_{\mathrm{n}} \,\mathrm{d}S,$$

where *W* is work, *p* is external pressure, h_{n} is a component of the bending field perpendicular to the surface of the sphere and G is the deformation area.[29]

Deformation energy

$$U = \int_\alpha \frac{E\delta^2 h_{\perp\perp}}{R\sqrt{3(1-\gamma^2)}} \mathrm{d}l,$$

where *U* is deformation energy, α is a meridian curve along the area of deformation and $h_\perp$ = component of the bending field perpendicular to α on the surface.

Geometrical equality

$$V = \iint_G h_n \,\mathrm{d}S = \frac{R}{2}\int_\alpha h_\perp \,\mathrm{d}l$$

We finally obtain the critical pressure of buckling [30]

$$p_{\mathrm{C}} = \frac{2E}{\sqrt{3(1-\gamma^2)}}\frac{h^2}{R^2}$$

The curvature factor *C* is included in the critical pressure formula to take into account the impact of natural curvature and rippling of graphene flakes and the inhomogeneous number of layers [31,32]

$$p_{\mathrm{C}} = \frac{2E}{\sqrt{3(1-\gamma^2)}}\frac{h^2}{R^2}\mathrm{C}$$

At each critical pressure for buckling $p_{\mathrm{C}}, p_{\mathrm{C1}}, p_{\mathrm{C2}}, \ldots, p_{\mathrm{C}(H-1)}$ a „new“ spring constant k_{c} is introduced. The buckling and folding create a larger number of new smaller pores caused and simultaneously increase the density of the GA

$$p_{\mathrm{C}} = \frac{2E}{\sqrt{3(1-\gamma^2)}}\frac{h^2}{R^2}C$$

$$\sigma = \frac{l}{A}\frac{1}{N_{\mathrm{z}}}\frac{2En}{\sqrt{3(1-\gamma^2)}}\frac{h^2}{R_1}mN_{\mathrm{x}}N_{\mathrm{y}}\varepsilon$$

$$p_{\mathrm{C1}} = \frac{2E}{\sqrt{3(1-\gamma^2)}}\frac{h^2}{R_1^2}C$$

$$\sigma = \frac{l}{A}\frac{1}{N_{\mathrm{z}}}\frac{2En}{\sqrt{3(1-\gamma^2)}}\frac{h^2}{R_2}m^2N_{\mathrm{x}}N_{\mathrm{y}}\varepsilon$$

$$p_{\mathrm{C2}} = \frac{2E}{\sqrt{3(1-\gamma^2)}}\frac{h^2}{R_2^2}C$$

$$\sigma = \frac{l}{A}\frac{1}{N_{\mathrm{z}}}\frac{2En}{\sqrt{3(1-\gamma^2)}}\frac{h^2}{R_3}m^3N_{\mathrm{x}}N_{\mathrm{y}}\varepsilon$$

$$p_{\mathrm{C}(H-1)} = \frac{2E}{\sqrt{3(1-\gamma^2)}}\frac{h^2}{R_{H-1}^2}C$$

$$\sigma = \frac{l}{A}\frac{1}{N_{\mathrm{z}}}\frac{2En}{\sqrt{3(1-\gamma^2)}}\frac{h^2}{R_H}m^HN_{\mathrm{x}}N_{\mathrm{y}}\varepsilon$$

The final equation for the origami-like nonlinear stress-strain behavior of the multiple buckled array of spherical springs can be expressed as:

$$\sigma_{\text{non-lin}} = \frac{l}{A} k_{\text{non-lin}} \varepsilon = \frac{l}{A} (\varphi_1(\sigma) k_1 + \varphi_2(\sigma) k_2 + \cdots + \varphi_{H-1}(\sigma) k_{H-1}) \varepsilon =$$

$$= \frac{l}{A} \frac{5}{11} \frac{N_x N_y}{N_z} \frac{2En}{\sqrt{3(1-\gamma^2)}} h^2 (\varphi_1(\sigma) * \frac{1}{R_1} m^2 + \varphi_2(\sigma) * \frac{1}{R_2} m^4 + \cdots$$

$$+ \varphi_{H-1}(\sigma) * \frac{1}{R_{H-1}} m^{2\text{H}}) \varepsilon,$$

where $R_1 \ldots R_{H-1}$ at each collapse $\varphi_1 \ldots \varphi_{\text{H}-1}$ decreases with increasing strain as

$$\varphi_0(\sigma) = \begin{cases} 0 & else \\ 1 & 0 < \sigma \leq p_{\text{c1}} \end{cases}$$

$$\varphi_1(\sigma) = \begin{cases} 0 & else \\ 1 & p_{\text{c1}} < \sigma \leq p_{\text{c2}} \end{cases}$$

$$\varphi_2(\sigma) = \begin{cases} 0 & else \\ 1 & p_{\text{c2}} < \sigma \leq p_{\text{c3}} \end{cases}$$

$$\varphi_3(\sigma) = \begin{cases} 0 & else \\ 1 & p_{\text{c3}} < \sigma \leq p_{\text{c4}} \end{cases}$$

$$\varphi_{\text{H}-1}(\sigma) = \begin{cases} 0 & else \\ 1 & p_{\text{c(H}-1)} < \sigma \end{cases}$$

F. Fitting of the experimental data

To use the MOBM for the fitting of the experimental data, it can be simplified into the following equation:

$$\sigma = \sigma_{\text{lin}} + \sigma_{\text{non-lin}} = \frac{5}{11} \frac{N_x N_y}{N_z} \frac{2En}{\sqrt{3(1-\gamma^2)}} \frac{h^2}{R} \frac{l}{A} \varepsilon + \sigma_1 + \sigma_2 + \sigma_3 + \ldots + \sigma_{\text{H}-1}$$

where

$$\sigma_1 = \frac{5}{11} \frac{N_x N_y}{N_z} \frac{2En}{\sqrt{3(1-\gamma^2)}} \frac{lh^2}{A} \frac{m_1}{R_1} \varepsilon = T \frac{m_1}{R_1} \varepsilon$$

$$\sigma_2 = T m_1 \frac{m_2}{R_2} \varepsilon$$

$$\sigma_3 = T m_1 m_2 \frac{m_3}{R_3} \varepsilon$$

$$\sigma_4 = T m_1 m_2 m_3 \frac{m_4}{R_4} \varepsilon$$

$$\sigma_5 = Tm_1m_2m_3m_4\frac{m_5}{R_5}\varepsilon$$

$$\sigma_6 = Tm_1m_2m_3m_4m_5\frac{m_6}{R_6}\varepsilon$$

$$\sigma_7 = Tm_1m_2m_3m_4m_5m_6\frac{m_7}{R_7}\varepsilon$$

...

The MOBM is applied to the measured stress-strain data of covalently cross-linked GA in compression. A 5.6 mm long GA sample with a surface area of 35 mm^2 was experimentally characterized using SEM and optical measurements to find the input values into MOBM. The GA is having average pore radius of 1 μm (SEM images), a wall thickness of 1.5 nm (corresponding to a few layers of graphene), the Poisson´s ratio of 0.03 (determined from optical measurements), and the number of pores in x, y and z-direction (3500, 2500 and 2800 from SEM images).

The results of fitting the experimental stress-strain and density-pressure data using the MOBM are shown in Figure 4.5a,b, and corresponding fitting parameters along with all input data in Table 4.3.

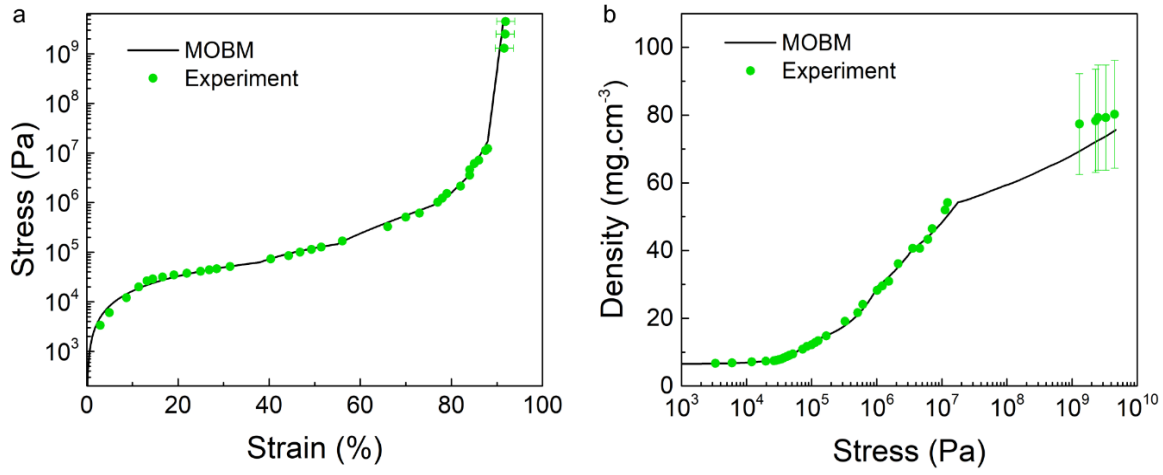

Figure 4.5 Fits of experimental compressive stress-strain data (a) and a density change with pressure (b) of graphene aerogels using the buckling model.

The fitting parameter *m* is close to 2 and there are 7 buckling collapses in the fully compressed GA resulting in the bending radius of 12 nm at 4.5 GPa. This bending radius

is still far from the theoretical limit defined by monolayer graphene (1 nm).[27] The MOBM determines the critical buckling limit of the first collapse to 53% strain, which is in line with the experimental observations (~ 55% strain).

Table 4.3 Parameters used for fitting in Figure 4.5.

Input	Value	Fitting parameters	Value
R	1 μm	m_1	2.05
H	1.5 nm	m_2	2.02
Γ	0.03	m_3	2.13
Nx	3500	m_4	2.17
Ny	2500	m_5	2.2
Nz	2800	m_6	2.25
E	1 TPa	m_7	2.29
L	5.6 mm	*n*	0.81
A	35 mm^2	Adj. R-Square	0.95

4.5 Energy dissipation

4.5.1 Hysteresis

One cycle of loading and unloading in the linear part of the stress-strain curve demonstrates almost no energy dissipation (~ 3%), which is exhibited by a negligible hysteresis, as shown in Figure 4.6a. However, once the buckling occurs (> 53% strain) the two paths of stress-strain curves diverge (Figure 4.6b). The significant hysteresis after 4 buckling collapses (equal to 88% strain) is presented, and the energy loss is calculated from the difference between the areas under loading and unloading curves which is 42%. This difference in the energy losses between the linear and buckling parts suggests that additional energy is required to restore the buckled pores. This energy is stored chiefly in the system in the form of strain energy, as confirmed by a rapid response of the GA upon the dynamic loading. The hysteresis of the presented GA compressed up to 88% of strain is significantly smaller in comparison with previous reports on graphene aerogels,[14,16] which is attributed to the reduced oxygen content in the presented GA.

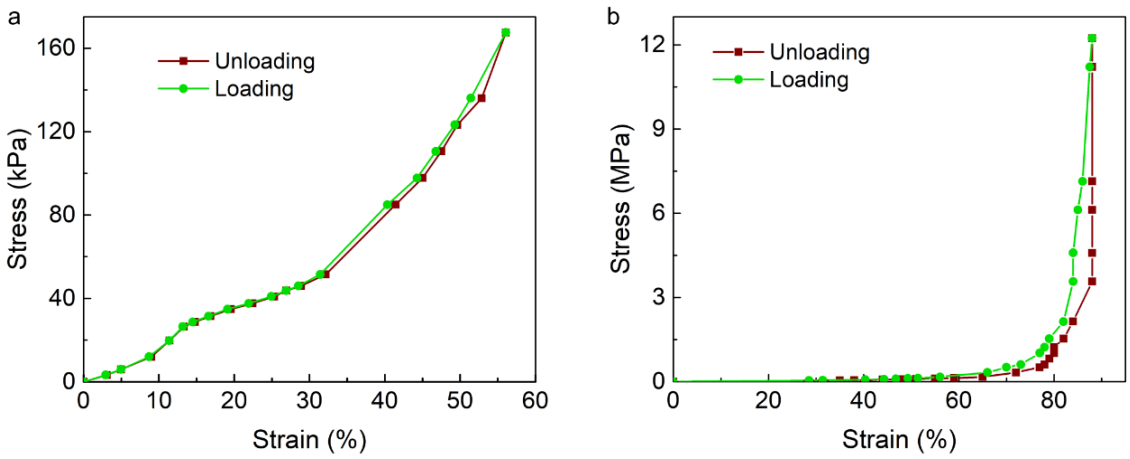

Figure 4.6 Reversibility of the graphene aerogel compression tests. (a),(b) The stress-strain curve up to 56% (a) and 88% (b) of strain.

4.5.2 Damping

The ball bouncing experiments are used to study the dynamic deformation of the GA block via a high-speed camera (Figure 4.7a). The GA demonstrates an extremely fast reaction to the falling ball. The GA immediately responded to the impact, and copied the movement of the bouncing ball (within the framerate 10000 fps). The impact of the ball on the GA lasts only for 2 ms. This is faster than the previously reported graphene aerogel reaction to a bouncing ball, which has lasted for 15 ms.[1] Interestingly, the GA returned to the original shape after the collision without any vibration. This observation is different from the dynamic response of common elastic (stainless steel spring) and plastic (polymeric foam) materials on the falling ball (Figure 4.7a). A steel spring as an elastic material followed the movement of the bouncing ball, but once the ball lost contact with a spring, it started vibrating. The typical plastic response of a polymeric foam is observed after the impact of the falling ball as an incomplete recovery and long-term shrinkage. As the optical approach to the dynamic deformation (> 50% strain) of GA does not result in any vibration due to the limitations of the fast camera, the response to the impact is measured via an electrical approach.

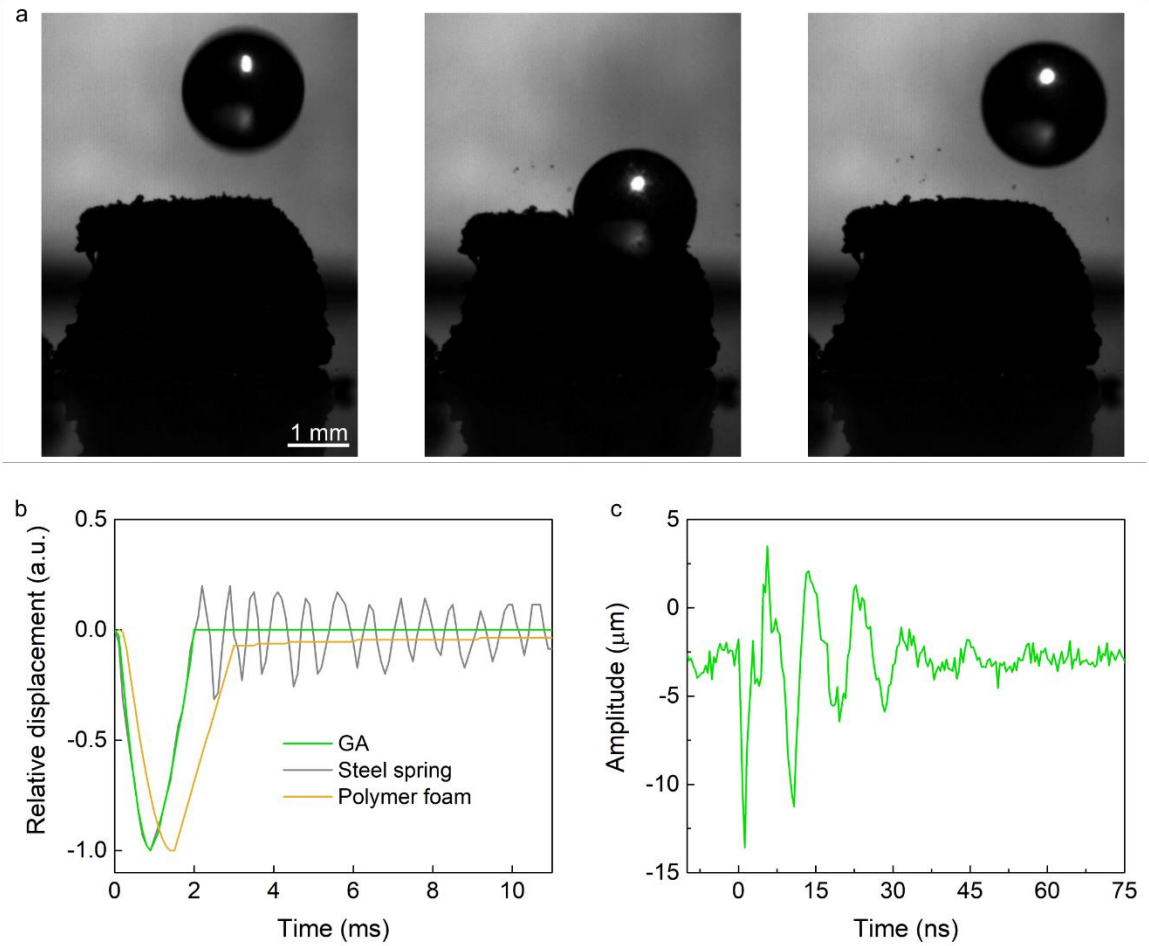

Figure 4.7 The response of the graphene aerogel (GA) to mechanical stimulation. (a) Optical images of a ball bouncing experiment with the GA. (b) Comparison of responses of the GA, elastic, and plastic materials on the impact of a bouncing ball determined using the high-speed camera. (c) The natural resonance of the GA on the mechanical stimulation is determined from the electrical response.

The electrical approach is based on passing the constant current through the GA and checking the voltage change using an oscilloscope which works down to a nanosecond regime. The GA sample is millimeter-sized and the mechanical oscillations induced by a metal rod are damped below 1 μm within 50-250 ns. 54 GA samples were electrically tested to find the damping properties and the inhomogeneities of GA samples cause the variation in damping. The induced oscillations of GA are underdamped with a resonance frequency (f_R) in the range of 20-150 MHz and damping ratio (ζ) ranging from 0.2 to 2.3× 10^7 (Figure 4.7b,4.9, and Table 4.4). The statistics of performed tests comparing their period, damping time, and ratio are shown in Table 4.4 and in Figure 4.8. Damping within

the ns regime has not been determined in any macroscopic elastic material before. For comparison, the few-layer free-standing graphene membrane-based resonator with micrometer dimensions showed a significantly slower damping time of ~ 20 µs.[33]

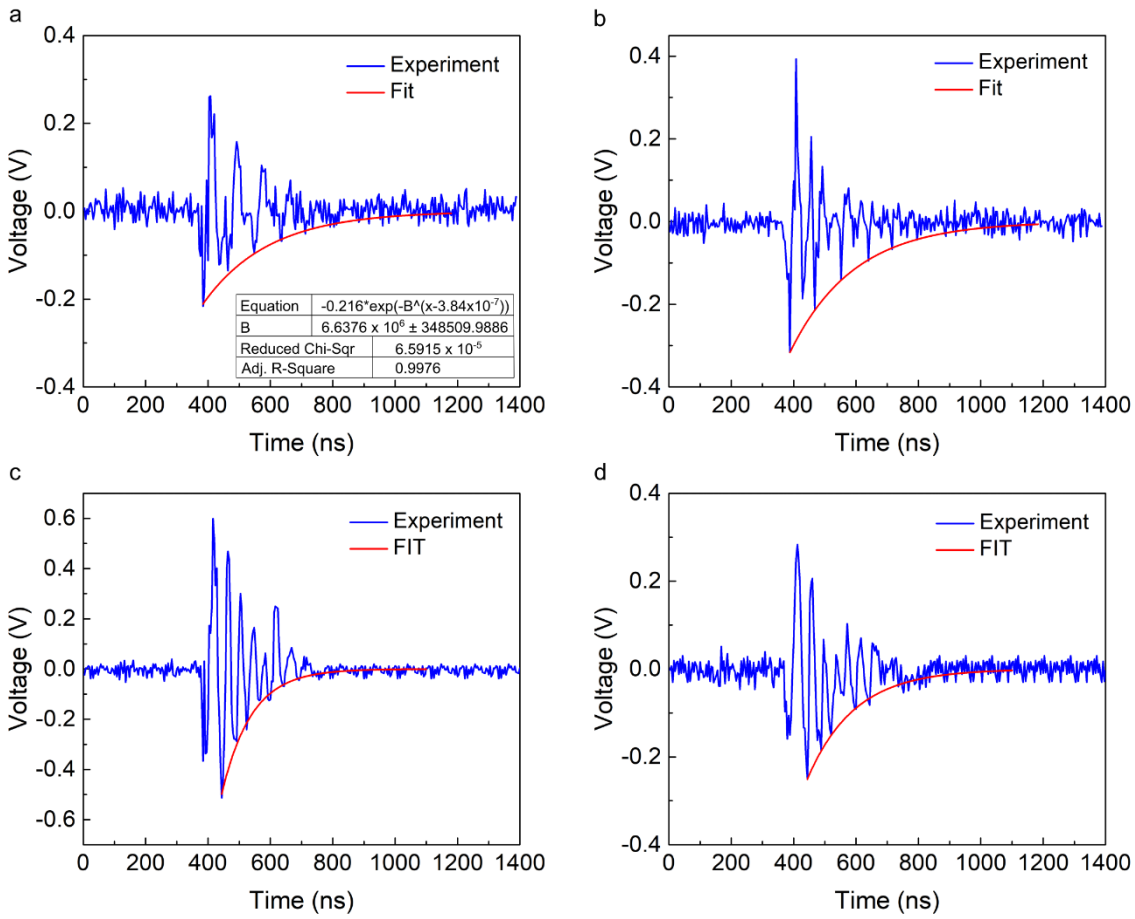

Figure 4.8 Change in voltage of different graphene aerogel specimens at different experimental conditions measured as a constant current of 0.1 A. The voltage change demonstrates the mechanical vibration of graphene aerogel specimens at resonance as a function of the varying pressure of 0.2 mbar (a) and 0.0002 mBar (b) and different cross-sectional areas of the specimens of 1 mm^2 (c) and 2 mm^2 (d). The specimen for the pressure measurements had dimensions of 2 × 2 × 2 mm. The cross-sectional area dependence was measured at a constant sample thickness of 2 mm and under atmospheric pressure. The fit to the experimental data shows the determined damping ratio (B).

Table 4.4 Statistics of the performed dynamic mechanical response tests (Figure 4.8) on different graphene aerogel specimens.

Number of tests	Period (ns)	Damping time (ns)	Damping ratio
8	9	50	3×10^7
6	10	100	5×10^7
11	24	200	2×10^7
29	40	400	5×10^6

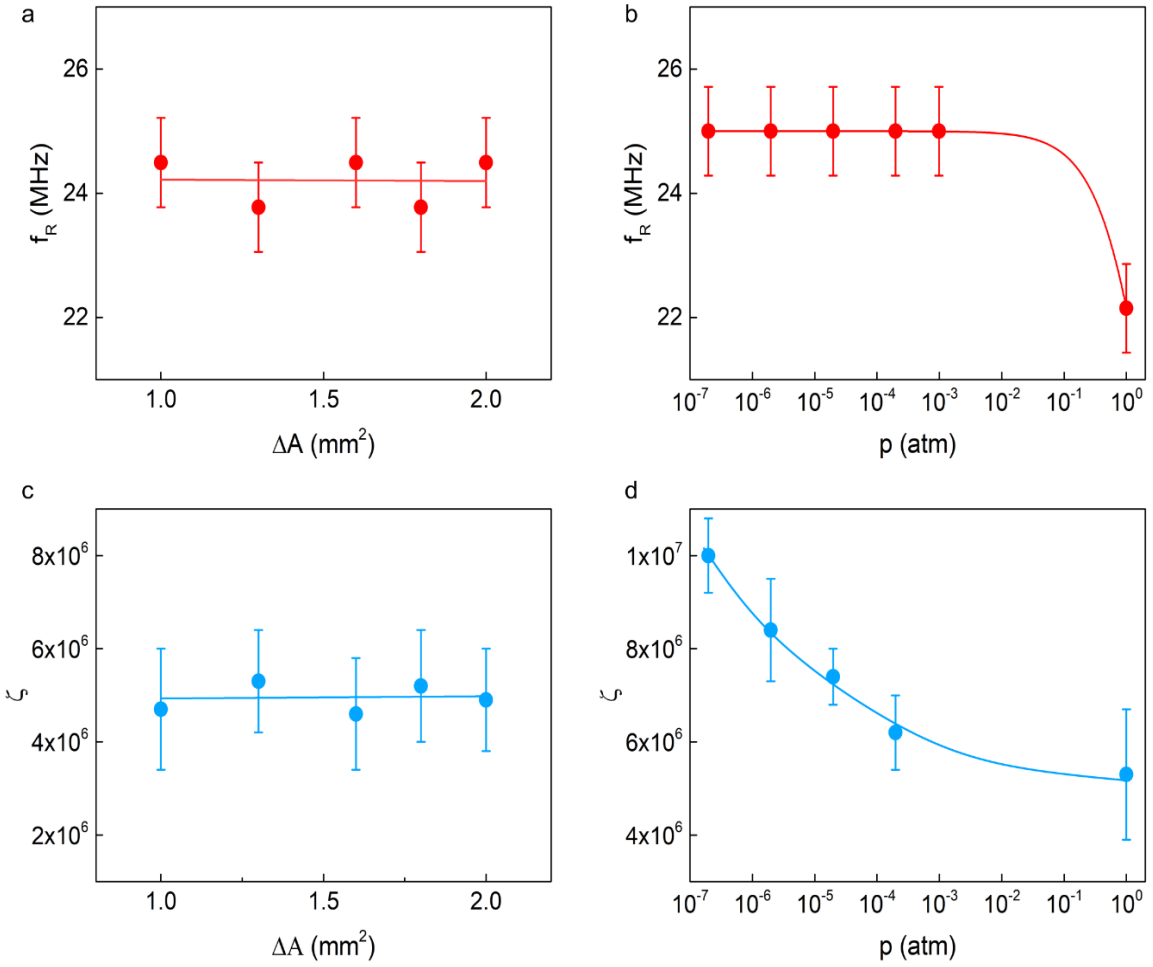

Figure 4.9 Dynamic mechanical response of the graphene aerogel (GA) block with the constant thickness of 2 mm. (a),(b) Resonant frequency (f_R) as the function of different cross-section area (ΔA) (a) and pressure (b). (e), (f) Damping ratio (ζ) as the function of different cross-section area (ΔA) (c) and pressure (d).

To get more insight into the nanosecond mechanical damping in the GA, the change of the resonant frequency and damping ratio was studied as a function of the dimension of

the sample and external applied pressure (Figure 4.9). By decreasing the pressure, the resonant frequency of the GA increases. This is in accordance with the usual diminishing of the drag force applied by the gasses on the moving sample in a vacuum. However, the GA vibrations are damped faster at lower external pressures, which is manifested as a higher damping ratio in a vacuum. The GA has additionally shown no recognizable change in the resonance frequency and damping ratio when the cross-section of the GA (ΔA) was decreased while the thickness is kept the same. The Hookean underdamped harmonic oscillator exhibits a completely different behavior than the one observed at GA. The resonance frequency and damping ratio in the Hookean oscillator ought to remarkably differ with the change of the GA´s cross-sectional area because it is related to the spring constant. Under a vacuum, the Hookean oscillator´s quality factor and damping should be increased and decreased, respectively.

The observed anomalous damping mechanism in the GA can be explained using an elastic scattering phenomenon similar to Thomson scattering.[34] In this case, however, the diffractive diffusion of waves is done by the mechanical wave scattering on the amorphous porous structure of the GA. The mechanism is based on the elastic distribution of the kinetic energy from the mechanical impact into vibrations of individual pores of the GA. This process is very fast and does not depend on frequency. The mechanical waves elastically propagate within the material by means of pore oscillation of interconnected cellular springs and the dynamic rippling of free-standing graphene walls,[33,35] resulting in inelastic diminishing via phonons and plasmons damping on the longer time scales.[36,37] As the mechanical waves spread in all directions, the longitudinal waves parallel to the direction of the impact decrease in amplitude when propagating through the pores of the sample. This results in fast diffusion and damping of the whole sample vibrations. The scattering process is not influenced by the difference in the cross-sectional area of the sample as soon as the area of the pore is significantly smaller than the cross-section of the sample. The observed increase in the speed and efficiency of the elastic scattering damping process under lower external pressure is also expected due to the lower air drag and lower amount of absorbed molecules on the surface of the GA in vacuum, which further improve the elasticity of the GA sample.

4.6 Conclusions

The GA was subjected to mechanical testing with a focus on the elasticity in tension and compression and response to a mechanical impuls. The GA exhibited an incredible elastic limit in compression (4.5 GPa) and tension (0.6 MPa), which is along with a minimal hysteresis completely different elastic behavior than conventional elastic bulk materials. Additionally, the achieved compressive and tensile yield strength observed in the GA are the highest from reported 3D graphene structures so far.The anomalous compressive behavior is explained with an analytical model based on the high bending flexibility of graphene sheets, which allows buckling of pore walls in the GA. The observed unique properties qualify the GA as a superelastic material. The superelastic behavior of the GA confirmed the formation of covalent cross-linking of graphene sheets, which enables the rapid elastic compressing and stretching over an incredibly wide range of stress and strain.

The fast mechanical response of the GA along with damping in the nanosecond range demonstrate almost perfect elastic collisions and the propagation of mechanical waves in the macroscopic material. These results ensure new possibilities for designing new strong and flexible ultralight materials, vibration dampers, sensors, and wearable electronics.

References

1. Gao, H.-L. *et al.* Super-elastic and fatigue resistant carbon material with lamellar multi-arch microstructure. *Nature Communications* **7**, 12920 (2016).
2. Zhao, K. *et al.* Super-elasticity of three-dimensionally cross-linked graphene materials all the way to deep cryogenic temperatures. *Science Advances* **5**, eaav2589 (2019).
3. Vatankhah-Varnosfaderani, M. *et al.* Mimicking biological stress–strain behaviour with synthetic elastomers. *Nature* **549**, 497–501 (2017).
4. Buehler, M. J. Materials by design—A perspective from atoms to structures. *MRS Bulletin* **38**, 169–176 (2013).
5. Qiu, L. *et al.* Extremely Low Density and Super-Compressible Graphene Cellular Materials. *Advanced Materials* **29**, 1701553 (2017).
6. Walsh, J. B., Brace, W. F. & England, A. W. Effect of Porosity on Compressibility of Glass. *Journal of the American Ceramic Society* **48**, 605–608 (1965).
7. Darling, K. A. *et al.* Nanocrystalline material with anomalous modulus of resilience and springback effect. *Scripta Materialia* **141**, 36–40 (2017).

8. Groβ, J. & Fricke, J. Scaling of elastic properties in highly porous nanostructured aerogels. *Nanostructured Materials* **6**, 905–908 (1995).
9. Liu, D. *et al.* Towards understanding the influence of porosity on mechanical and fracture behaviour of quasi-brittle materials: experiments and modelling. *Int J Fract* **205**, 57–72 (2017).
10. Zhang, W. *et al.* Preparation and properties of silicone rubber materials with foam/solid alternating multilayered structures. *Polymer Journal* **53**, 619–631 (2021).
11. Faridmehr, I. *et al.* Correlation between Engineering Stress-Strain and True Stress-Strain Curve. *American Journal of Civil Engineering and Architecture* **2**, 53–59 (2014).
12. Proctor, J. E. *et al.* High-pressure Raman spectroscopy of graphene. *Phys. Rev. B* **80**, 073408 (2009).
13. Kashani, H., Ito, Y., Han, J., Liu, P. & Chen, M. Extraordinary tensile strength and ductility of scalable nanoporous graphene. *Science Advances* **5**, eaat6951 (2019).
14. Li, C., Ding, M., Zhang, B., Qiao, X. & Liu, C.-Y. Graphene aerogels that withstand extreme compressive stress and strain. *Nanoscale* **10**, 18291–18299 (2018).
15. Guo, F. *et al.* Highly stretchable carbon aerogels. *Nature Communications* **9**, 881 (2018).
16. Worsley, M. A. *et al.* Mechanically robust 3D graphene macroassembly with high surface area. *Chem. Commun.* **48**, 8428–8430 (2012).
17. Worsley, M. A. *et al.* High Surface Area, sp2-Cross-Linked Three-Dimensional Graphene Monoliths. *J. Phys. Chem. Lett.* **2**, 921–925 (2011).
18. Crisafulli, A., Khodayari, A., Mohammadnejad, S. & Fasano, M. Sliding Dynamics of Parallel Graphene Sheets: Effect of Geometry and Van Der Waals Interactions on Nano-Spring Behavior. *Crystals* **8**, 149 (2018).
19. Grandbois, M., Beyer, M., Rief, M., Clausen-Schaumann, H. & Gaub, H. E. How Strong Is a Covalent Bond? *Science* **283**, 1727–1730 (1999).
20. Cao, K. *et al.* Elastic straining of free-standing monolayer graphene. *Nature Communications* **11**, 284 (2020).
21. Ubbelohde, A. R. Hole and Claw Defects in Graphite. *Nature* **180**, 380–380 (1957).
22. Zoldesi, C. I., Ivanovska, I. L., Quilliet, C., Wuite, G. J. L. & Imhof, A. Elastic properties of hollow colloidal particles. *Phys. Rev. E* **78**, 051401 (2008).
23. Frank, I. W., Tanenbaum, D. M., van der Zande, A. M. & McEuen, P. L. Mechanical properties of suspended graphene sheets. *Journal of Vacuum Science & Technology*

B: Microelectronics and Nanometer Structures Processing, Measurement, and Phenomena **25**, 2558–2561 (2007).

24. Zoelly, R. Ueber ein Knickungsproblem an der Kugelschale, Thesis, Zurich, 1915.
25. Koiter, W. T.The nonlinear buckling problem of a complete spherical shell under uniform external pressure, Parts I, II, III & IV. Proc. Kon. Ned. Ak. Wet. B72, 40-123.
26. Pogorelov, A. V. Bendings of surfaces and stability of shells. *American Mathematical Society*, Providence, 1988, Vol. 72.
27. Lu, Q., Arroyo, M. & Huang, R. Elastic bending modulus of monolayer graphene. *J. Phys. D: Appl. Phys.* **42**, 102002 (2009).
28. Gomez, M., Moulton, D. E. & Vella, D. The shallow shell approach to Pogorelov's problem and the breakdown of 'mirror buckling'. *Proceedings of the Royal Society A: Mathematical, Physical and Engineering Sciences* **472**, 20150732 (2016).
29. Gao, C., Donath, E., Moya, S., Dudnik, V. & Möhwald, H. Elasticity of hollow polyelectrolyte capsules prepared by the layer-by-layer technique. *Eur. Phys. J. E* **5**, 21–27 (2001).
30. Hutchinson, J. W. Buckling of spherical shells revisited. *Proceedings of the Royal Society A: Mathematical, Physical and Engineering Sciences* **472**, 20160577 (2016).
31. Meyer, J. C. *et al.* The structure of suspended graphene sheets. *Nature* **446**, 60–63 (2007).
32. Martinez-Asencio, J., Ruestes, C. J., Bringa, E. M. & Caturla, M. J. Controlled rippling of graphene via irradiation and applied strain modify its mechanical properties: a nanoindentation simulation study. *Phys. Chem. Chem. Phys.* **18**, 13897–13903 (2016).
33. He, Y. Z. *et al.* Dynamic ripples in single layer graphene. *Appl. Phys. Lett.* **98**, 063101 (2011).
34. Thomson, J. J. On Electrical Oscillations and the effects produced by the motion of an Electrified Sphere. *Proceedings of the London Mathematical Society* **s1-15**, 197–219 (1883).
35. Keşkekler, A. *et al.* Tuning nonlinear damping in graphene nanoresonators by parametric–direct internal resonance. *Nature Communications* **12**, 1099 (2021).
36. Buljan, H., Jablan, M. & Soljačić, M. Damping of plasmons in graphene. *Nature Photonics* **7**, 346–348 (2013).
37. Yan, H. *et al.* Damping pathways of mid-infrared plasmons in graphene nanostructures. *Nature Photonics* **7**, 394–399 (2013).

5 Electro-mechanical properties

5.1 Introduction

In recent years, porous 3D graphene based materials have been widely investigated for tactile sensors, biomedical and robotics applications.[1–3] The main advantage of using these materials lies in the variety of incredible physical properties, such as elasticity, compressibility, fast response, high electrical conductivity, and most importantly, piezoresistivity under applied pressure.[4] Recently, 3D graphene based strain sensors have been demonstrated to provide fast response and incredible sensitivity in compression. However, the current 3D graphene based sensors still suffer from high hysteresis and limited tensile elasticity, which need to be improved.[1,4–6] Also, there has not been reported a 3D graphene based electro-mechanical sensor which could operate both in compression and tensile sensing with a tensile strain higher than 20%.[7] These limitations significantly restrict the range of applicability of 3D graphene based sensors and pose the main obstacle to their practical use in wearable electronics and human-machine interface applications.[7,8] These issues originate mainly from the insufficient elasticity range of the GA materials, which is caused by the weak coupling between the graphene sheets in the 3D structure.[9]

There have been several attempts to overcome the challenges associated with the use of 3D graphene in tactile sensors.[4,7] Researchers have used various additives, such as flexible polymers, carbon nanotubes, etc.,[3,4] to make 3D graphene materials more flexible and overcome the weak coupling problem between graphene layers. The addition of even a small amount of additives enabled increasing the stretchability range of the sensor materials, but it was at the cost of decreased compressibility, strength, and electrical properties of the materials.[10] The size of the detection range of tactile sensors can also be significantly affected by the mechanism of the sensing. However, the most commonly used sensing mechanism based on bulk piezo resistivity is limited only to a narrow range of elastic deformations and pressures.[1,5,11] Other reported piezoresistive sensing mechanisms, such as tunneling effect,[12] crack propagation,[13] and overlapping-disconnecting resistivity,[4] also provide a narrow strain range of detection. Therefore, multiple tactile sensors must be used for broad-range strain and stress detection.

This chapter demonstrates the use of the covalently cross-linked GA for fast and broad-range electrical tactile sensors. The GA sensor utilizes a novel sensing mechanism based on the change of the electrical contact resistance under applied uniaxial tensile and compressive stress. The sensor performance is characterized based on the measurement of the response time, gauge factor, sensitivity, and repeatability. The results show that the sensor is highly sensitive, superfast, and can operate over a large range of strain and pressure in compression and tension. Additionally, the sensor is tested in practical applications for the detection of human body motion, such as human heart rate and hand object manipulation.

5.2 Methods

The construction of the GA sensor is very simple (Figure 5.1). It has a piece of the GA sensing element electrically connected to a power supply, which changes its electrical resistance when deformed. For a detailed description of the electrical response measurement of the GA under tension and compression, see the Mechanical testing part in the Methods of Chapter 2. The critical part of the sensing element is the connection of the GA with a Cu tape. This connection has to be mechanically robust, electrically conductive, and most importantly, highly elastic. Silver epoxy glue (MG Chemicals) was found to meet all the requirements mentioned above, and additionally, it did not penetrate deep inside the GA. Therefore, the GA sensing element was attached to the Cu electrical leads using silver epoxy glue.

The electrical measurements were done using a Keithley source measure unit (Model 236 and 237). The electrical resistance changes, as well as I-V characteristics, were measured using either a constant voltage (0.01 V) or constant current (0.1-0.5 A) mode. The response time of sensors was measured by applying a constant current of 0.5 A with a current source unit (Agilent E3631A). The human pulse was measured by attaching a sensor directly above the human skin at the wrist with a flexible tape and measured at a constant voltage (0.01 V). The change in the output voltage in the GA sensors was monitored with an oscilloscope (Tektronix TDS 620B) in the falling ball experiments. For this purpose, a small steel ball (0.1 g) was thrown on the sensor from a height of ~ 75 cm. The resulting graphs from the electrical sensor characterization are a summary of 5 different samples. Each point in the figures is an average of 10 load-unload cycles.

5.3 Graphene aerogel sensor

5.3.1 Electro-mechanical properties of sensors

Figure 5.1 shows the response of the GA sensor under tension and compression using a two-probe method. The electrical resistance demonstrates a nonlinear behavior as the mechanical stress-strain increases in compression and tension. The total resistance of the sensor increases and decreases when tension and compression is applied to the sensor, respectively. The sensor is able to detect a change in the resistance of two orders of magnitude over the whole measured strain range of 78% in compression and 68% in tension. These results show that the electro-mechanical properties of the GA sensor are highly suitable for tactile sensor applications. The measured strain range covers the whole range of deformations observed in biology, opening a possibility for detecting mechanical strain of all biological materials.[3,29]

In a real application, a sensor must retain its properties in a different environment, especially at changing temperatures. The temperature range of -60 to 100 °C was used to find the dependence of the GA sensor response at 0% and 20% compressive strain. The sensor proved to be temperature independent. Additionally, the GA sample was tested independently using the four-probe method to assure temperature independence. This temperature independence of the GA sensor properties is brilliant for real applications where the correct functioning is ensured even at extreme temperatures. The temperature dependence, usually observed in sensors with bulk material mechanisms, might cause undesired fluctuations of a false signal.[14,15]

The relation between electrical response as a function of compressive or tensile stress of the GA sensor can be measured as a relative change in resistance, voltage, or current at a constant current or voltage, respectively. The response of the GA sensor in terms of the electrical resistance change as a function of mechanical loading is shown in Figure 5.1b in the range of 0-1.18 MPa and 0-0.55 MPa for compression and tensile stress. Over this whole range of fully stretched (~ 68% strain) to fully compressed state (~ 78% strain), the resistance of the GA sensor exhibits a 230% increase. The demonstrated mechanical range of the sensor is significantly larger than in any other reported graphene-based and other electro-mechanical sensors in the literature so far (Table 1.2). These results demonstrate that the GA-based devices can be used as strain sensors, which can cover the whole broad range of human bodily actions, including gentle and high-force movements.[16]

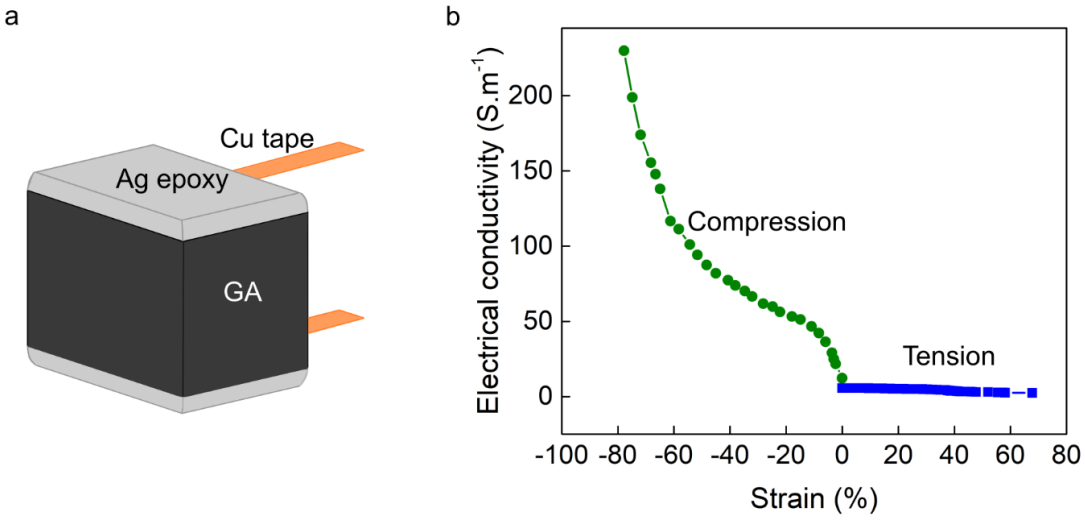

Figure 5.1 Schematic and response of the graphene aerogel (GA) sensor. (a) Schematic of the GA sensor. (b) The electrical response of the GA sensor measured by two-probe configuration under compressive and tensile strain. and response of the graphene aerogel sensor.

Figure 5.2a,d illustrates the response of the GA sensor to compressive and tensile strain in terms of resistance and current. The response of the GA sensor at a constant voltage of 0.01 V is obtained as a relative change in the current and resistance. Both resistance/current-strain curves show similar bilinear dependence consisting of two regions with a constant gauge factor (*GF*) and sensitivity (*S*). The gauge factor here is defined as the ratio of relative electrical resistance change ($\Delta R/R_0$) to mechanical strain (ε). The sensitivity is the ratio of relative current change ($\Delta I/I_0$) to applied pressure difference (ΔP). The first linear region in compression is around 0-6% of strain. This detection region of the GA sensor is highly sensitive to applied pressure. The corresponding values of *GF* and *S* are 11.6 and 53.5 MPa^{-1} (Figure 5.2b,c). This value of the gauge factor is, in comparison with other previously reported sensors based on 3D graphene and conventional metal alloy,[17] several times higher. The second linear region in region 6-78% of strain has the gauge factor (0.38) and sensitivity (12.2 MPa^{-1}) roughly 30 and 4.4 times lower than the first region. In compression, the sensor reaches a much higher pressure regime than other graphene aerogel-based sensors reported so far.[4]

The tensile strain response in Figure 5.2e,f also consists of two linear regions separated at 30% of strain. The region of tensile strain below 30% is described with a gauge factor of 0.6 and sensitivity of 0.39 MPa^{-1}. The gauge factor and sensitivity are significantly

increased to 3.4 and 1.85 MPa^{-1} in the region above 30% strain. In tension, the sensor surpasses all previous graphene aerogel-based sensors reported so far (Table 1.2).

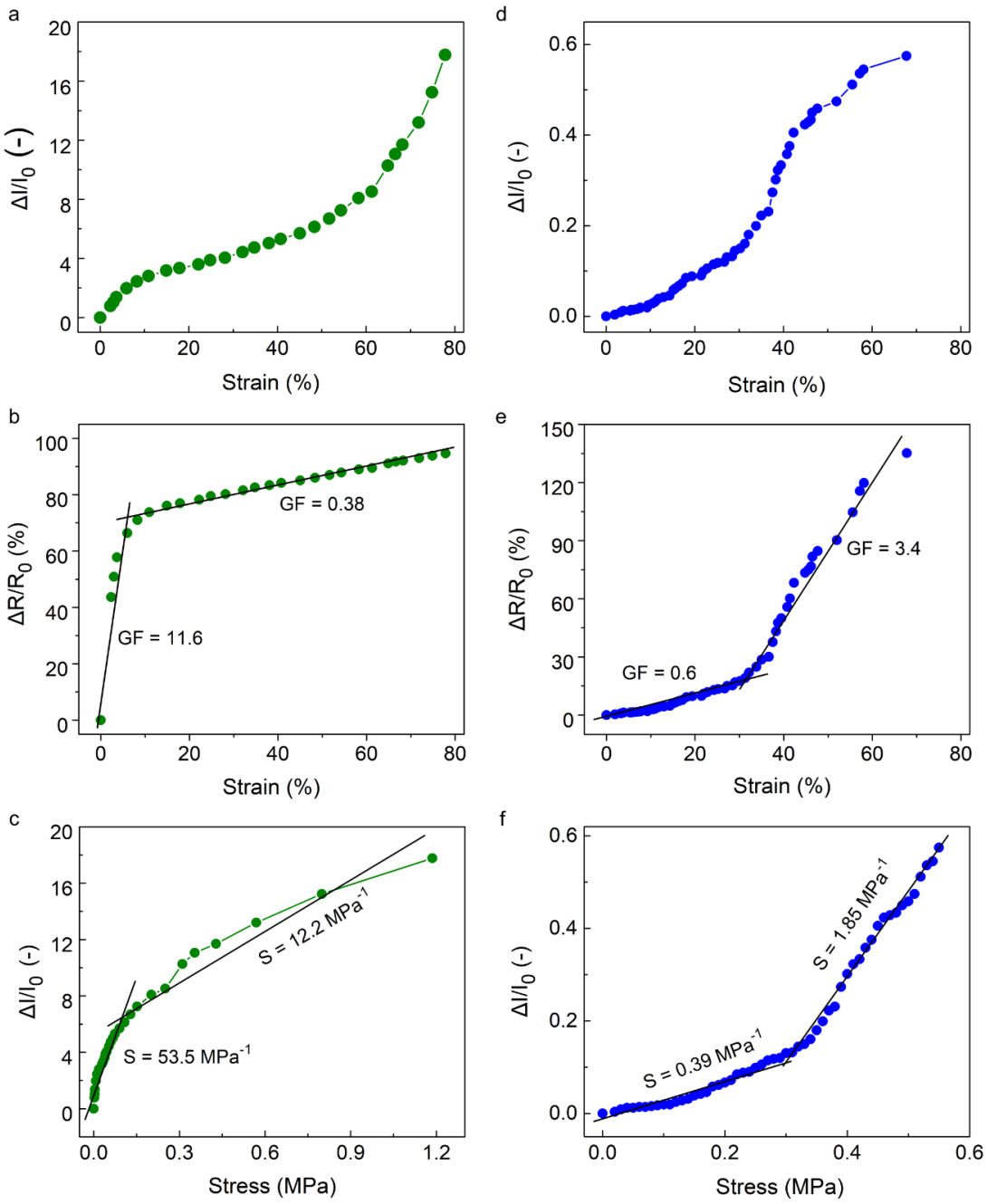

Figure 5.2 Electrical response of GA strain sensors under compression (left) and tension (right). (a, d) Current ($\Delta I/I_0$) response and (b, e) relative resistance change ($\Delta R/R_0$) of GA sensors with applied compressive and tensile stress, respectively. (c, f) The current response of the GA sensors as a function of compressive and tensile stress shows two sensitivity regimes. The slope of the curves was used to calculate the gauge factor (GF = $(\Delta R/R_0)/\varepsilon N$) and sensitivity ($S = (\Delta I/I_0)/\Delta P$) of the sensors.

5.3.2 Sensing mechanism

To gain more insight into the sensing mechanism, the structural changes of the GA sensor under compression were measured using in-situ using Raman spectroscopy and XRD. The results of the Raman spectroscopy and XRD are shown in Figure 5.3. There is no major change presented neither in Raman nor in XRD spectra under compression up to 70% strain. These results prove that the elastic behavior of the GA, described in the Mechanical section in Chapter 4 of this thesis, does not affect the crystal structure and chemical bonding in the GA samples. Therefore, it can be concluded that the structural changes in the compression are not the reason for the exceptional sensor response. Thus, the other suspect is the electrical contacts in the GA sensor.

A two-probe and four-point probe measurements were performed to separate the effect of the contact resistance from the total resistance of the sensor in Figure 5.4a. The two-probe measurements in top-bottom and bottom contact configurations show both a huge change of resistance over the applied strain range (Figure 5.4b). The course of the curve is very similar for both configurations. This means that the position of the contacts does not affect the response of the sensor. The independence of the position of the contacts in the two-probe measurement suggests that there is no change in the structure of the GA, which is in line with the observation from Raman and XRD spectra. However, this observation is in strong contradiction to the traditional piezoelectric sensors, where the electrical contacts need to be placed on the opposite sites of the sample to capture the deformation occurring in the bulk of the material.

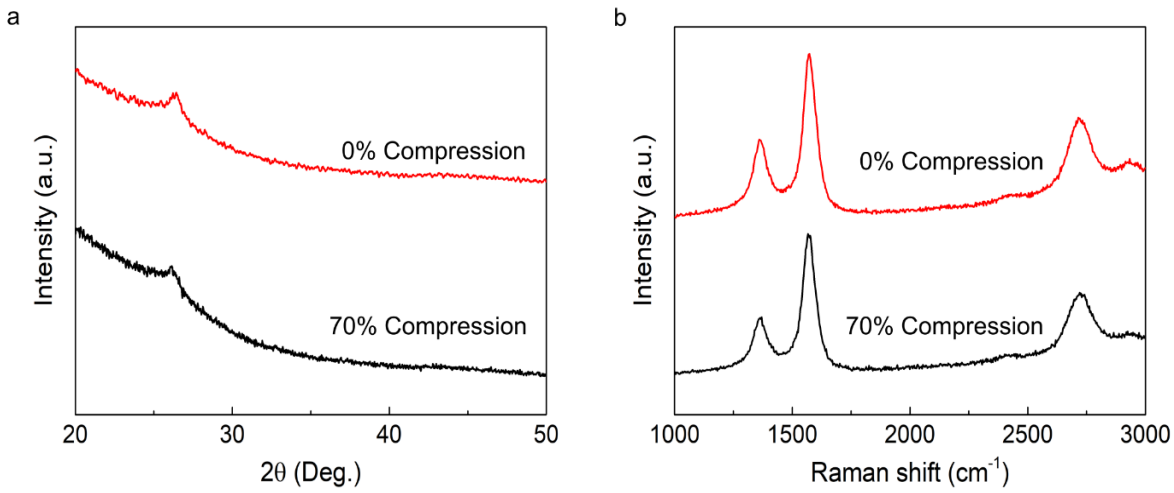

Figure 5.3 The graphene aerogel (GA) characterization under 70% compression. (a) X-ray diffractograms (b) Raman spectra of an unstrained and 70% compressed GA.

In Figure 5.4b, a four-probe measurement was performed to measure the actual resistance of the GA element by excluding the contact resistance. The measured electrical resistivity of the GA element is 0.02 Ω.m and does not vary much with the strain. This confirms that the sensing mechanism originates predominantly from the variation of the contact resistance of the interface between the porous GA and silver epoxy electrical contacts and not from the change of the internal resistance of the GA material.

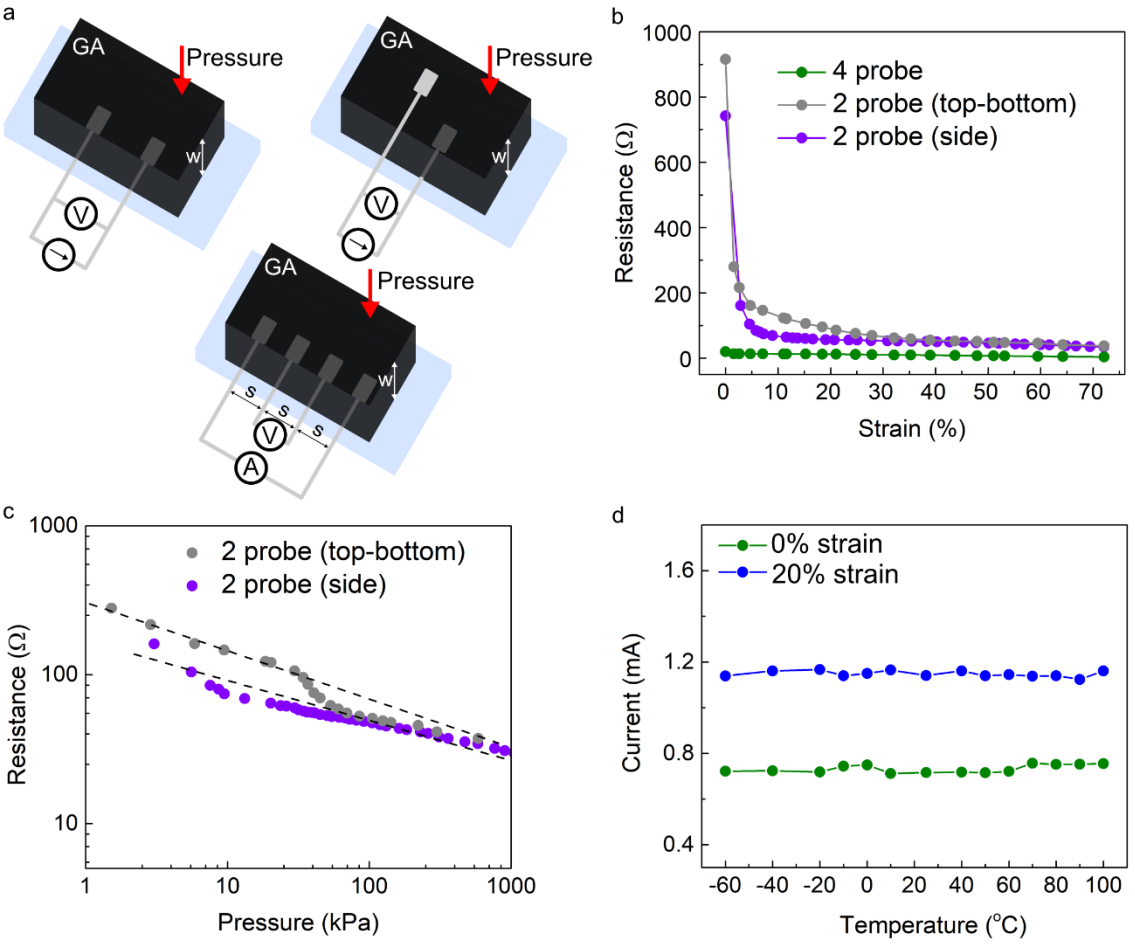

Figure 5.4 Effects of contact resistance on the graphene aerogel (GA) sensors under applied pressure. (a) Experimental setups for contact resistance measurements: two-probe configurations (top-bottom and bottom-bottom), and four-probe configuration. (b) The electrical resistance of the GA sensor was measured using the configuration shown in (a). (c) The relation between resistance and pressure of the GA sensor is measured in two-probe configurations. (d) Temperature dependence of the GA sensor response.

The contact resistance mechanism in the GA device is also confirmed in a resistance-pressure plot in Figure 5.4c. The plot shows an inverse linear log(*R*) and log(*P*)

relationship, which is a typical characteristic of the contact resistance dominated sensing mechanism.[18–21] The log-log plot in the contrary to the plot in Figure 5.2b is not bilinear but possesses a single power-law dependence of resistance with pressure with nonnegative exponents. The linear dependence in the log-log plot spans over 3 orders of magnitude of a pressure, which is very unique. This means that the observed bilinear behavior shown in Figure 5.2 is simply a linear log-log asymptote of the contact resistance response.

Based on the two and four-probe measurements, it can be concluded that the observed resistance change in the GA sensors with compressive and tensile stress originates from a varying electrical contact between the graphene sheets/struts with the silver epoxy glue. These findings also reveal that there is a simple power-law variation of the contact resistance with pressure in the GA sensors, which can be used for the quantitative determination of the stress and strain.

Figure 5.5 shows the schematics of the mechanically variable contact resistance based sensing mechanism of the GA sensor. The sensing is based on the mechanical variation of the interface between the graphene sheets and the silver epoxy glue which results in a change of the total resistance of the sensor in two-probe resistance measurement. The total resistance of the GA sensor, R_T, can be expressed as the summation of the resistances of all its components

$$R_T = R_C + R_{GA},$$

where R_C is the contact resistance and R_{GA} is the resistance of the GA. The relation of changes in the R_C vs. pressure (P) is described as

$$R_C(P) = P^m,$$

where c is a constant and m is the slope of the linear curve in the log-log graph. One of the requirements for using contact resistance as the sensing mechanism is

$$R_C \gg R_{GA}.$$

If the condition is not satisfied, for example, the R_{GA} is higher than R_C, then the signal-to-noise ratio will be small and the change in the output current cannot be easily distinguished. This condition is well fulfilled in the GA sensor. This condition also suggests that the lower the resistance of the GA, the greater the sensor's sensitivity and lower current is needed for detection. This means that the electrical contact based sensing mechanism is inherently economically efficient and can operate at low power.

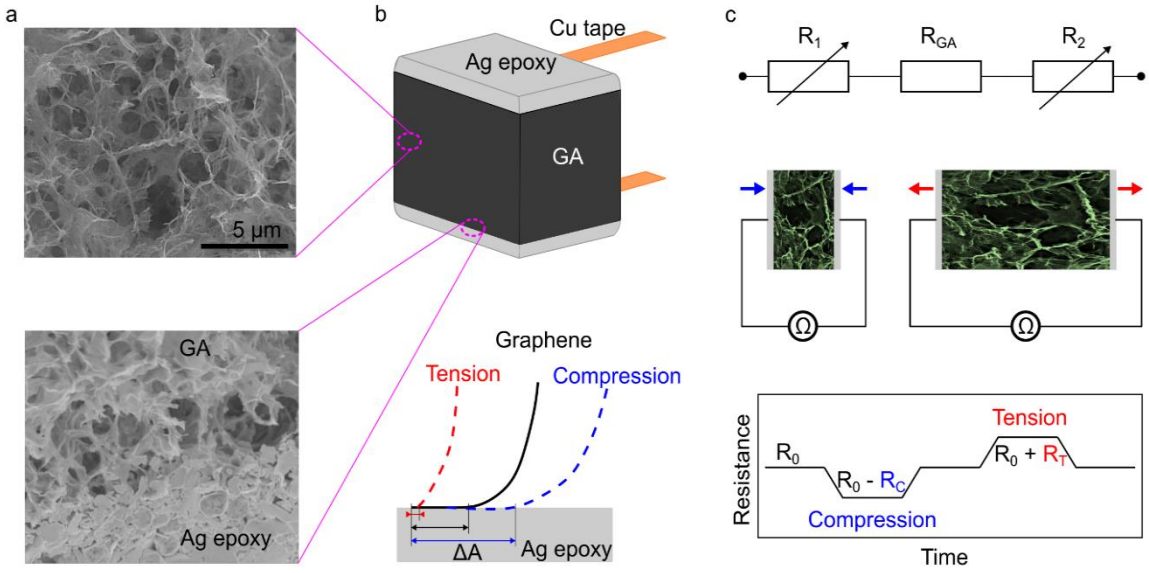

Figure 5.5 Contact resistance based sensing mechanism of the GA sensor. (a) Scanning electron micrographs of the GA showing the overall structure and the interface between the GA and silver epoxy glue. (b) Schematic of the GA sensor and the detail of the contact area (ΔA) between the graphene walls and the glue. The contact of the graphene and glue is changed according to the deformation. (c) Illustrations of the resistance change with deformation, where R_1, and R_2 denote the variable resistance of contacts related to the contacts, as shown in (b).

The contact based sensing mechanism in the GA sensor is highly reversible due to the high flexibility of the graphene flakes and their covalent cross-linking in the GA. The cross-linking of the graphene flakes provides an even distribution of the applied pressure and the deformation across the contact area of the silver glue and electrode. The description of the compression mechanism, including displacement, buckling, and bending of graphene pores described in Chapter 4 can be used as the explanation of the contact resistance changes at the interface of the GA and the silver epoxy. Under pressure, the deformation of pores increases the contact area of graphene flakes and thus the number of electrical paths between the GA and metal contacts (Figure 5.5b). Therefore, there is a decrease in the total resistance with pressure. At small deformations, minimal displacement is required for small pores and close vicinity of graphene struts to come together or close enough for tunneling. Additionally, there is also an increase in the electrical pathways due to the increased contact area at the edges of the pores. At large strain (high pressure) there is an increase in wall-to-wall contact area due to bending and buckling of all pore sizes resulting in a lowering of the contact resistance. The operation

range of the contact resistance is the result of incredible mechanical properties of the GA respectively graphene layers which provide the ohmic contact with rigid electrodes.

The sensing mechanism based on the variable contact resistance has not been observed in any electro-mechanical 3D graphene based sensors.[1,4–6] However, it has already been demonstrated in other materials.[18–21] The previously reported mechanisms proposed for 3D graphene based sensors have been based mainly on the change of the bulk resistivity.[1,4–6] Unlike the usual bulk resistivity mechanisms, the variable contact resistance mechanism opens up the possibility of creating conceptually new sensors, as it relies mainly on the GA-contact interface. These sensors can be easily up or downscaled because the thickness of the GA does not affect the change in the contact resistance. Moreover, these sensors demonstrate fundamentally new features in comparison with standard ones because the contacts can be placed on the GA arbitrarily and independently of the applied force. If the right combination of the GA and contacts is chosen, the contact resistance exhibits temperature independence.

5.3.3 Dynamic response

The dynamic response of the GA sensor is shown in Figure 5.6. The GA sensor´s electrical response demonstrates an excellent recovery without any significant hysteresis when the load is released, similarly as observed in the mechanical testing in Chapter 4. It means the GA sensor can be used as a pressure and strain sensor simultaneously. The electrical current measurements were also used to determine the minimum force which can be detected with the GA sensor. The minimal detection limit of ~ 326 μN is demonstrated in Figure 5.6c. For the determination of the sensor´s response time, a small steel ball (0.1 g) was dropped on the sensor from a height of ~ 75 cm. The sample was powered with a fixed current (0.5 A) and the induced change in voltage of the sensor was measured using an oscilloscope. The rise time, defined as the time necessary for the increase of the output voltage from 10% to 90% of its maximum value, is calculated as 5.2×10^{-4} s. The fall time calculated as 6.1×10^{-4} s is the time required to drop the voltage from 90% to 10% of its maximum value (Figure 5.6d). The response time of the GA sensor is several orders of magnitude faster compared to the response time of previously reported GA sensors,[2,22,23] composited of,[24–27] metal nanoparticles,[28–32] porous sponges,[33,34] and graphene transferred on polymer.[35–37] The GA sensors can operate at a wider range of pressures, ranging from 1.18 MPa in compression to 0.55 MPa in tension. The comparison of the GA sensor with previously reported sensors can be seen in Figure 1.4 in Chapter 1.

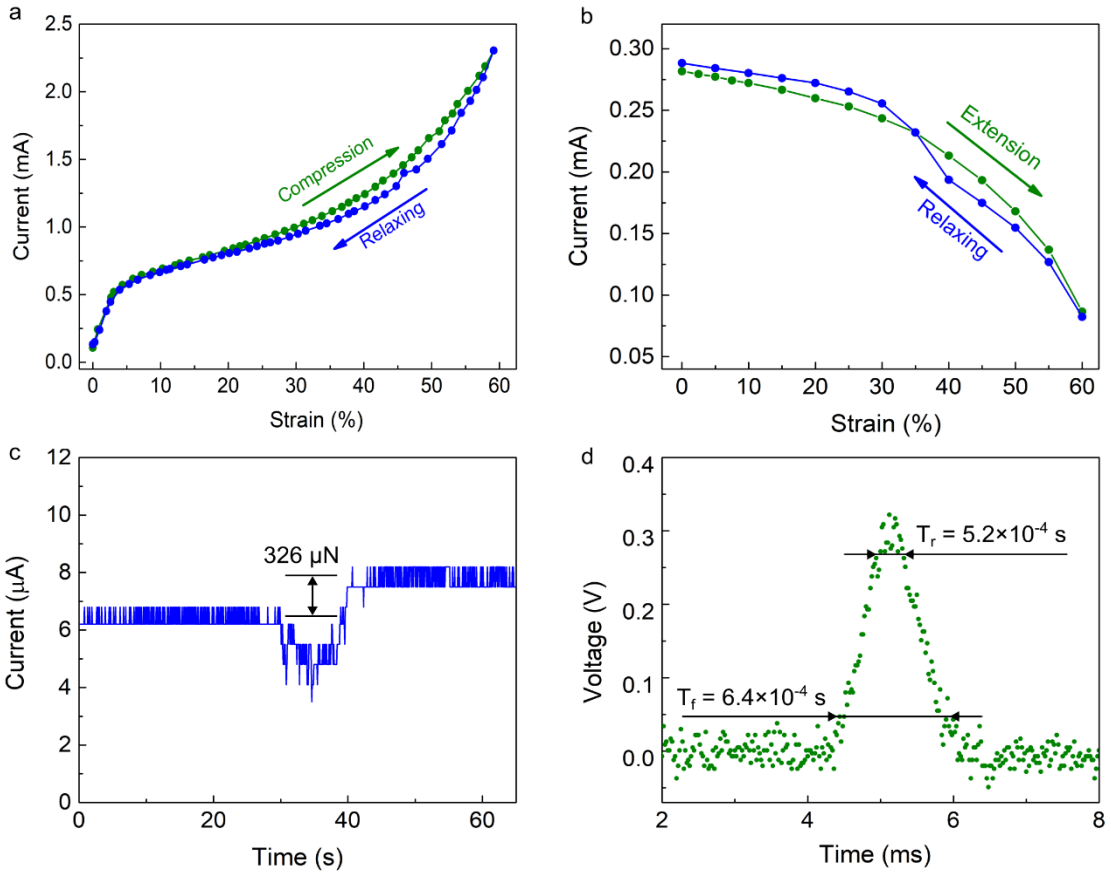

Figure 5.6 The sensitivity and response time of the GA sensors. (a) and (b) Hysteresis curve of the GA sensor subjected to compressive (a) and tensile (b) stress. (c) The voltage response of the GA sensor shows the response time characteristics (T_r is rise time, T_f is fall time). (d) Ultralow force is detected by the current response of the GA sensor.

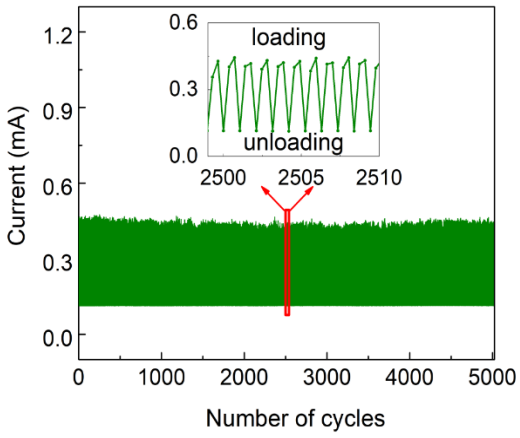

Figure 5.7 The durability test of the graphene aerogel sensor. The sensor was subjected to repeated compression.

The durability and reliability of the GA sensor under dynamic pressure conditions were also tested as a result of the stability of the sensor´s response over more than 5000 cycles of loading and unloading (Figure 5.7f).

5.3.4 Applications

The GA-based sensor demonstrates a unique set of properties as a broad operation range, fast response, temperature independence, and high sensitivity, which are essential for several applications. In compression mode, the sensor operates in the pressure range of 10^0-10^6 Pa, which allows it to be used in real-time and quantitative measurements of human bodily actions from the skin.[16] In Figure 5.8, the simple and ultrasensitive haptic sensor platform based on the GA was used for different applications of human body actions characterized by small or large pressure.

To confirm the high sensitivity of the GA sensor in a real application, the heartbeat was determined from the movement of the artery on the wrist (Figure 5.8a,b). The sensor conformally covered the skin above the artery and reacted to the micrometer deformations of the skin caused by the pulsing of the artery. The GA sensor recorded the regular radial artery pulse waveform of a healthy person, and the heartbeat was determined from this signal (~ 72 BPM). With a detailed look at the recorded signal, there are three distinguishable peaks presented, which represent the pulse waveform of the incident forward wave (P1), reflected waveforms of the late systolic wave (P2), and the early diastolic wave (P3). The pulse waveform data can be used for calculating blood pressure. Thus, the GA sensor can provide real-time monitoring of blood pressure and pulse simultaneously.[38,39]

The GA sensor was attached to a finger of a hand to demonstrate the wide range of operation and tactile sensing. The sensor attached to the index finger was subjected to a deformation caused by force used to hold and lift an object between the index finger and thumb (Figure 5.8c,d). The objects used in this experiment had variable weights (0.37-515 g), such as foam, a magnet, and a bottle with a liquid. The electrical response of the GA sensor shows the increase of electrical current with a load. As the sensor is calibrated against a known weight, it is possible to find out the mass of the lifted objects with high accuracy. This particular example of tactile operation can be used in robotic applications to estimate the right force necessary for grasping the object.[40] To further dig into the human-machine interface ability of the sensor, the GA sensor was mounted on the top of

the index finger, which was gradually bent. Figure 5.8e shows the response of the sensor to the bending of the finger. The sensor can detect the varying angle of the finger. These experimentally proved applications qualify the GA sensor for artificial skin and wearable sensor applications.

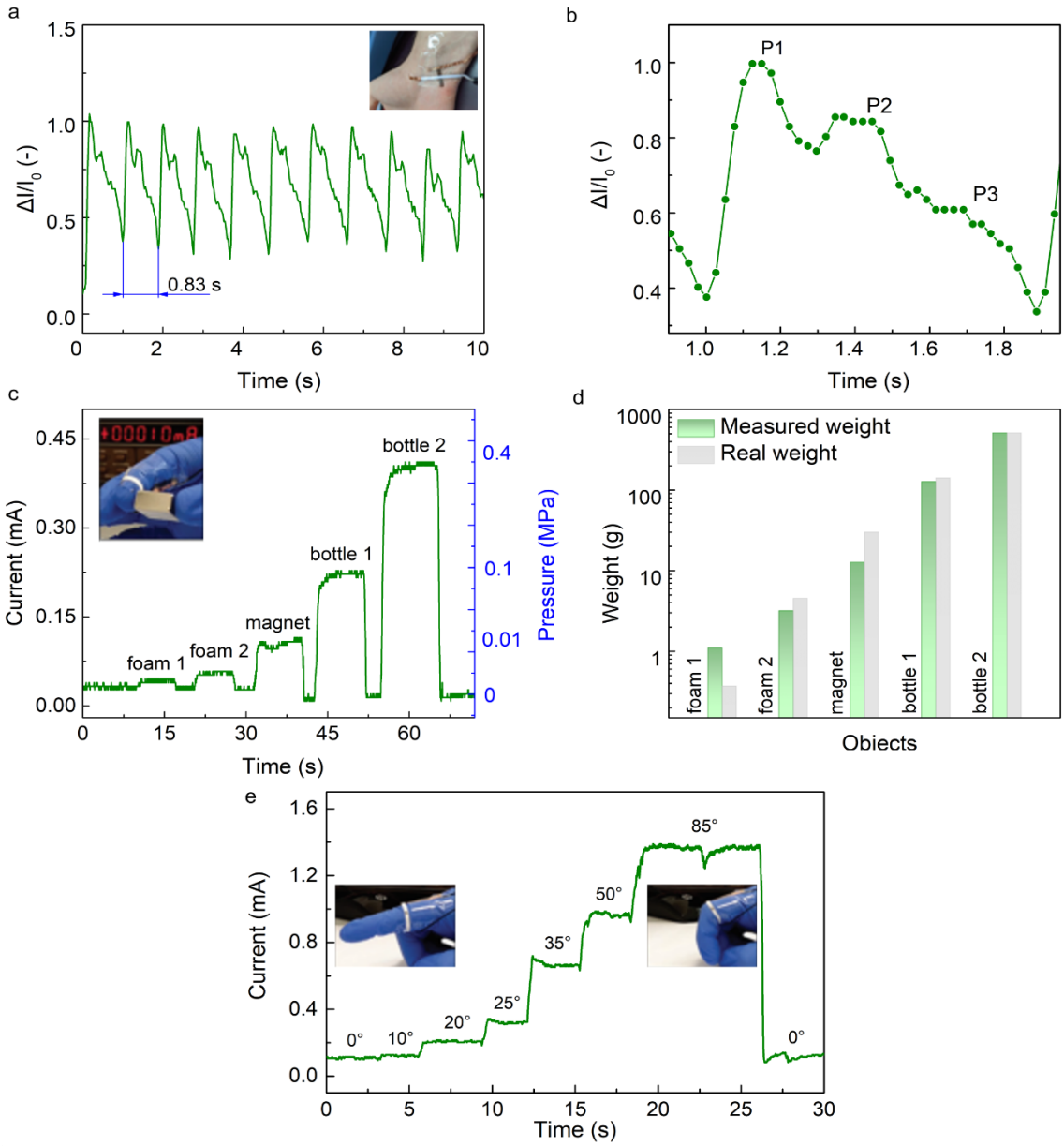

Figure 5.8 Tactile sensing using GA sensors. (a) The current response of a GA sensor detects the movement of the artery on the wrist as a function of time. (b) A detail of a single peak from (a) showing three characteristic waveforms (P1, P2, and P3) of a human heart rate. (c) The response of the GA sensor (attached to the index finger) on grasping objects of variable weight with the thumb and index finger. (d) Comparison of the real and measured weight of different objects by the GA sensor in (c). (e) Monitoring the response of the GA sensor attached to the index finger to finger-bending motions.

5.4 Conclusions

In conclusion, the electro-mechanical properties of the GA were studied in regards to their application in tactile sensors. A fast, ultrasensitive, and wide-range pressure and strain covalently cross-linked GA sensor was prepared and characterized. The sensor worked in an incredibly broad range of pressures in tensile (0-0.55 MPa) as well as in compression (0-1.18 MPa). This wide working range enabled to sense all human bodily actions within a single sensor. Additionally, the sensor demonstrated negligible hysteresis, which can be used for simultaneous strain and pressure measurement. Moreover, the sensor showed a fast response time of 5.2×10^{-4} s and high sensitivity characterized by a gauge factor of 11.6 in the compression and 3.4 in the tensile mode. The long-term stability and repeatability of the sensor were proved over 5000 compressing cycles. These unique properties of the sensor originate from a new sensing mechanism based on the variation of the contact resistance between the GA and metal contact with deformation.

The GA sensor was successfully used in several practical applications. The sensor was capable of monitoring the human heart rate and pulse waveform from the wrist. It also enabled determination of the weight of the grasped objects and monitoring finger bending. These real examples prove the possibility of using the GA sensor for biomedical as well as robotic applications. Considering the simple fabrication of the sensor and its incredible mechanical and electro-mechanical properties, it has a high potential for real applications in biomedicine, wearable electronics, and tactile robotic applications.

References

1. Lou, Z., Wang, L. & Shen, G. Recent Advances in Smart Wearable Sensing Systems. *Advanced Materials Technologies* **3**, 1800444 (2018).
2. Qiu, L. *et al.* Ultrafast Dynamic Piezoresistive Response of Graphene-Based Cellular Elastomers. *Advanced Materials* **28**, 194–200 (2016).
3. Jeong, Y. R. *et al.* Highly Stretchable and Sensitive Strain Sensors Using Fragmentized Graphene Foam. *Advanced Functional Materials* **25**, 4228–4236 (2015).
4. Luo, S., Samad, Y. A., Chan, V. & Liao, K. Cellular Graphene: Fabrication, Mechanical Properties, and Strain-Sensing Applications. *Matter* **1**, 1148–1202 (2019).

5. Wang, C., Dong, L., Peng, D. & Pan, C. Tactile Sensors for Advanced Intelligent Systems. *Advanced Intelligent Systems* **1**, 1900090 (2019).
6. Yu, J., Zhang, K. & Deng, Y. Recent progress in pressure and temperature tactile sensors: principle, classification, integration and outlook. *Soft Science* **1**, 6 (2021).
7. Kashani, H., Ito, Y., Han, J., Liu, P. & Chen, M. Extraordinary tensile strength and ductility of scalable nanoporous graphene. *Science Advances* **5**, eaat6951 (2019).
8. Vatankhah-Varnosfaderani, M. *et al.* Mimicking biological stress–strain behaviour with synthetic elastomers. *Nature* **549**, 497–501 (2017).
9. Sun, H., Xu, Z. & Gao, C. Multifunctional, Ultra-Flyweight, Synergistically Assembled Carbon Aerogels. *Advanced Materials* **25**, 2554–2560 (2013).
10. Papageorgiou, D. G., Kinloch, I. A. & Young, R. J. Graphene/elastomer nanocomposites. *Carbon* **95**, 460–484 (2015).
11. Tiwana, M. I., Redmond, S. J. & Lovell, N. H. A review of tactile sensing technologies with applications in biomedical engineering. *Sensors and Actuators A: Physical* **179**, 17–31 (2012).
12. Zhao, H. & Bai, J. Highly Sensitive Piezo-Resistive Graphite Nanoplatelet–Carbon Nanotube Hybrids/Polydimethylsilicone Composites with Improved Conductive Network Construction. *ACS Appl. Mater. Interfaces* **7**, 9652–9659 (2015).
13. Li, X. *et al.* Stretchable and highly sensitive graphene-on-polymer strain sensors. *Sci Rep* **2**, 870 (2012).
14. Traina, M., Pegoretti, A. & Penati, A. Time–temperature dependence of the electrical resistivity of high-density polyethylene/carbon black composites. *Journal of Applied Polymer Science* **106**, 2065–2074 (2007).
15. Jiang, M.-J., Dang, Z.-M. & Xu, H.-P. Significant temperature and pressure sensitivities of electrical properties in chemically modified multiwall carbon nanotube/methylvinyl silicone rubber nanocomposites. *Appl. Phys. Lett.* **89**, 182902 (2006).
16. Kenry, Yeo, J. C. & Lim, C. T. Emerging flexible and wearable physical sensing platforms for healthcare and biomedical applications. *Microsyst Nanoeng* **2**, 1–19 (2016).
17. Jansen, K. M. B. Effect of pressure on electrical resistance strain gages. *Experimental Mechanics* **37**, 245–249 (1997).
18. Pan, L. *et al.* An ultra-sensitive resistive pressure sensor based on hollow-sphere microstructure induced elasticity in conducting polymer film. *Nat Commun* **5**, 3002 (2014).

19. Timsit, S. Electrical contact resistance: properties of stationary interfaces. *Electrical Contacts - 1998. Proceedings of the Forty-Fourth IEEE Holm Conference on Electrical Contacts (Cat. No.98CB36238)* (1998) doi:10.1109/6144.759357.
20. Holm, R. The relation between contact load and resistance, particularly at moderate and high load. in *Electric Contacts* 40–48 (Springer Berlin Heidelberg, 1967).
21. Electrical Contact Resistance: Fundamental Principles. in *Electrical Contacts: Principles and Applications* (ed. Slade, P. G.) (CRC Press, 2014). doi:10.1201/b15640.
22. Pang, Y. *et al.* Flexible, Highly Sensitive, and Wearable Pressure and Strain Sensors with Graphene Porous Network Structure. *ACS Appl Mater Interfaces* **8**, 26458–26462 (2016).
23. Hu, K., Szkopek, T. & Cerruti, M. Tuning the aggregation of graphene oxide dispersions to synthesize elastic, low density graphene aerogels. *J. Mater. Chem. A* **5**, 23123–23130 (2017).
24. Wang, X., Gu, Y., Xiong, Z., Cui, Z. & Zhang, T. Silk-Molded Flexible, Ultrasensitive, and Highly Stable Electronic Skin for Monitoring Human Physiological Signals. *Advanced Materials* **26**, 1336–1342 (2014).
25. Park, J. *et al.* Giant Tunneling Piezoresistance of Composite Elastomers with Interlocked Microdome Arrays for Ultrasensitive and Multimodal Electronic Skins. *ACS Nano* **8**, 4689–4697 (2014).
26. Liu, M. *et al.* Large-Area All-Textile Pressure Sensors for Monitoring Human Motion and Physiological Signals. *Advanced Materials* **29**, 1703700 (2017).
27. Li, J., Orrego, S., Pan, J., He, P. & Kang, S. H. Ultrasensitive, flexible, and low-cost nanoporous piezoresistive composites for tactile pressure sensing. *Nanoscale* **11**, 2779–2786 (2019).
28. Lee, J. *et al.* Conductive Fiber-Based Ultrasensitive Textile Pressure Sensor for Wearable Electronics. *Advanced Materials* **27**, 2433–2439 (2015).
29. Zhang, H. *et al.* Cohesive thermoplastic-assisted patterning and assembly of a textile-supported piezoresistive sensor for monitoring human vital signs. *Smart Mater. Struct.* **27**, 105027 (2018).
30. Wei, Y., Chen, S., Lin, Y., Yang, Z. & Liu, L. Cu–Ag core–shell nanowires for electronic skin with a petal molded microstructure. *J. Mater. Chem. C* **3**, 9594–9602 (2015).

31. Wu, Y. *et al.* Channel Crack-Designed Gold@PU Sponge for Highly Elastic Piezoresistive Sensor with Excellent Detectability. *ACS Appl. Mater. Interfaces* **9**, 20098–20105 (2017).
32. He, W. *et al.* Polypyrrole/Silver Coaxial Nanowire Aero-Sponges for Temperature-Independent Stress Sensing and Stress-Triggered Joule Heating. *ACS Nano* **9**, 4244–4251 (2015).
33. Dong, X. *et al.* A linear and large-range pressure sensor based on a graphene/silver nanowires nanobiocomposites network and a hierarchical structural sponge. *Composites Science and Technology* **155**, 108–116 (2018).
34. Luo, Y., Xiao, Q. & Li, B. Highly compressible graphene/polyurethane sponge with linear and dynamic piezoresistive behavior. *RSC Adv.* **7**, 34939–34944 (2017).
35. Pang, Y. *et al.* Epidermis Microstructure Inspired Graphene Pressure Sensor with Random Distributed Spinosum for High Sensitivity and Large Linearity. *ACS Nano* **12**, 2346–2354 (2018).
36. Liu, W. *et al.* Piezoresistive Pressure Sensor Based on Synergistical Innerconnect Polyvinyl Alcohol Nanowires/Wrinkled Graphene Film. *Small* **14**, 1704149 (2018).
37. Xia, K., Wang, C., Jian, M., Wang, Q. & Zhang, Y. CVD growth of fingerprint-like patterned 3D graphene film for an ultrasensitive pressure sensor. *Nano Res.* **11**, 1124–1134 (2018).
38. Nichols, W. W. Clinical measurement of arterial stiffness obtained from noninvasive pressure waveforms. *American Journal of Hypertension* **18**, 3S-10S (2005).
39. O'Rourke, M. F., Pauca, A. & Jiang, X.-J. Pulse wave analysis. *British Journal of Clinical Pharmacology* **51**, 507–522 (2001).
40. Sundaram, S. *et al.* Learning the signatures of the human grasp using a scalable tactile glove. *Nature* **569**, 698–702 (2019).

6 Fire resistance of graphene aerogels

6.1 Introduction

Fire causes enormous damage, injuries, and loss of life worldwide. Protecting materials from fire damage is vital to many industrial, academic, and life safety applications. Although a handful of inherently flame-retardant materials exist, they are often expensive, difficult to be prepared in a large quantity, or do not have suitable physical properties for the applications.[1] Therefore, there is a great demand for the development of new materials or chemical treatments that can prevent fire and protect materials and skin from burn damage or injury. In recent years, there has been increased interest in using various surface treatments to localize flame-retardant protection at the exterior of a material, where combustion occurs. These treatments have included surface modifications, sol-gel treatments, layer-by-layer coatings, and intumescent polyelectrolyte complexes.[2–4] The application of flame-retardant treatments has been effective in reducing the flammability at the interface where an ignition source meets a flammable material,[5] but it could not change the inherent flammability of the material.

Carbon-based flame-retardant treatments provide environmentally responsible and effective flame protection. Over the years, numerous carbon-based flame-retardant treatments have been extensively investigated on different organic substances, such as fabric, wood, and polymers.[6–9] Most of them included the addition of fire-retardant agents in the materials to promote carbonization and the creation of a heat-resistant char layer on their surface.[10] These treatments employed a gas-phase flame-retardant mechanism or a condensed-phase flame-retardant mechanism.[11,12] The former refers to a mechanism in which the flame retardant produces non-flammable gasses in the combustion process to dilute oxygen and combustible gas or block free radicals to participate in the combustion chain reaction.[1] The latter one is based on the formation of a fire protecting carbon-rich char layer, which creates a passive barrier on the sample surface with self-extinguishing behavior during flame exposure.[13] Char is a porous lightweight black carbon material with a high specific surface.[14] Char layers are typically produced by a pyrolytic process by heating organic matter in the absence of oxygen. In this process, carbon residues are solidified through cross-linking and condensation reactions, creating a durable, low-thermal-conductivity char shell on the surface of a flammable material.[15] The resulting char

layer protects the underlying material from the action of the heat flux or the flame. It acts as a physical barrier that delays the transfer of heat and blocks the release of combustible gas in the pyrolysis of the material. Various methods of char preparation have been reported over the last two decades.[15–17] Researchers have fabricated char layers containing diverse mixtures of sp^2-sp^3 hybridized carbon. Recent studies have demonstrated that higher graphitization of char resulting in honeycomb-like cross-linked carbon can better resist fire,[18,19] providing a promising route to enhance flame-retardancy. This raises an intriguing question about the role of sp^2-bonded carbon and defects in the fire resistance mechanism of carbon-based flame-retardant materials.

Graphene has recently demonstrated excellent fire-resistant properties.[20–22] Graphene has been shown to efficiently prevent the incorporation of oxygen into materials, acting as an anticorrosion and flame-retardant layer.[23] In recent years, graphene additives and coatings have been extensively investigated in the development of fire-resistant materials.[24,25] Adding graphene as an additive in materials has been shown to enhance not only their resistance to flame but also many other properties of the composite materials.[26] Although graphene possesses high thermal stability in vacuum, the flame retardancy of pure graphene has not been found satisfactory in air.[27,28] This is because single-layer graphene has relatively low-temperature stability in air of approximately 500 °C before it starts to oxidize.[29] The oxidation stability of graphene can be further enhanced by increasing the number of layers up to a temperature of 705 and 870 °C for few-layer graphene and graphite, respectively.[30] Nevertheless, multilayer graphene materials assembled in a layer-by-layer manner have too high thermal conductivity to provide a sufficient thermal barrier to protect the material from fire/high temperature.[31,32] Therefore, graphene layers have rather been used as seed layers for the formation of char layers on organic materials in fire-retardant applications.[33] Interestingly, arranging graphene in a 3D porous structure can combine both the important virtues of 2D graphene and low thermal conductivity in a single material. 3D graphene structures in the form of foams, sponges, and aerogels have demonstrated oxidation stability between 500-705 °C,[34] yet extremely low thermal conductivity.[35] Although there have been a few attempts that involved fire resistance testing of graphene aerogels,[36–38] little is known about the actual fire-retardant ability and fire resistance of high-quality 3D graphene.

In this chapter, the experimental observation of high-temperature fire resistance of GA with self-extinguishing behavior during flame exposure is reported. Structural and chemical changes of high-quality covalently cross-linked GA are systematically

investigated at different temperatures in air when exposed to propane, hydrogen, candle, and isopropyl alcohol (IPA) flames. The behavior of the GA is compared to graphene layers on a silicon dioxide substrate. The flammability and combustion rates of graphene are strongly influenced by the arrangement of graphene flakes in the material. In particular, the results reveal that the GA exhibits 1000 °C higher fire resistance than graphene on a substrate. Upon evaluating the structural and chemical changes of different graphene aerogels, the conditions at which the GA is fire resistant and exhibits self-extinguishing behavior to flame are determined, providing important guidelines for designing carbon-based flame resistant and retardant materials.

6.2 Methods

Thermal diffusivity was measured using LFA apparatuses Netzsch LFA 467 (temperatures under 20 °C) and LFA 467 HT (temperatures above 20 °C). The penetration model, provided by the Netzsch company, was used for fitting the measured data. Recalculation of the thermal conductivity was done considering the specific heat capacity of graphite 707 $J.kg.K^{-1}$ for the GA [39]. This assumption can be made because the specific heat capacity of graphene aerogels is similar to graphite [35]. The samples measured by the LFA were shaped into discs with a diameter of 6 mm and a thickness of 1 mm. Each sample was measured 3 times in the LFA apparatus. The thermal conductivity was evaluated as the average of 5 different samples.

The burning experiments were done using 4 different types of flame. The GA sample (4× 3 × 3 mm) was attached to a non-flammable substrate and exposed to a flame. The burning process of GA specimens was recorded on a camera. The key parameter, the temperature of the flame, was determined with a thermocouple placed in contact with the sample. The temperature of flame mentioned in the results section describes the surface temperature of the GA in contact to the flame. The flames used for burning of graphene and GA were hydrogen (1500 °C), propane (1200 °C), candle (800 °C), and IPA (550 °C) flames. Each burning experiment was repeated 10 times and the graphs are the average of all results.

Thermogravimetric analysis (TGA) was performed using a simultaneous thermal analyzer (Setaram Themys 2400) and mass spectrometer (Pfeiffer GSD 320 O3 OmniStar). The GA sample with a mass of 0.2-0.4 mg was heated in a platinum crucible with a heating rate of 10 $°C.min^{-1}$. To perform the combustion thermal analysis of the GA samples in the

conditions similar to the normal air atmosphere, a homemade TGA setup was assembled (Figure 6.1). The homemade TGA consists of a tungsten boat, in which the GA sample (3× 2 × 1 mm) was heated up via a passing current regulated with a variable transformer. The temperature was measured using a pyrometer. The tungsten boat was covered with a glass lid to control the atmosphere around the sample. The atmosphere was controlled by flowing a mixture of CO_2 and air under the glass lid. Here as opposed to the standard TGA, the volume loss was observed from a video taken through the glass lid.

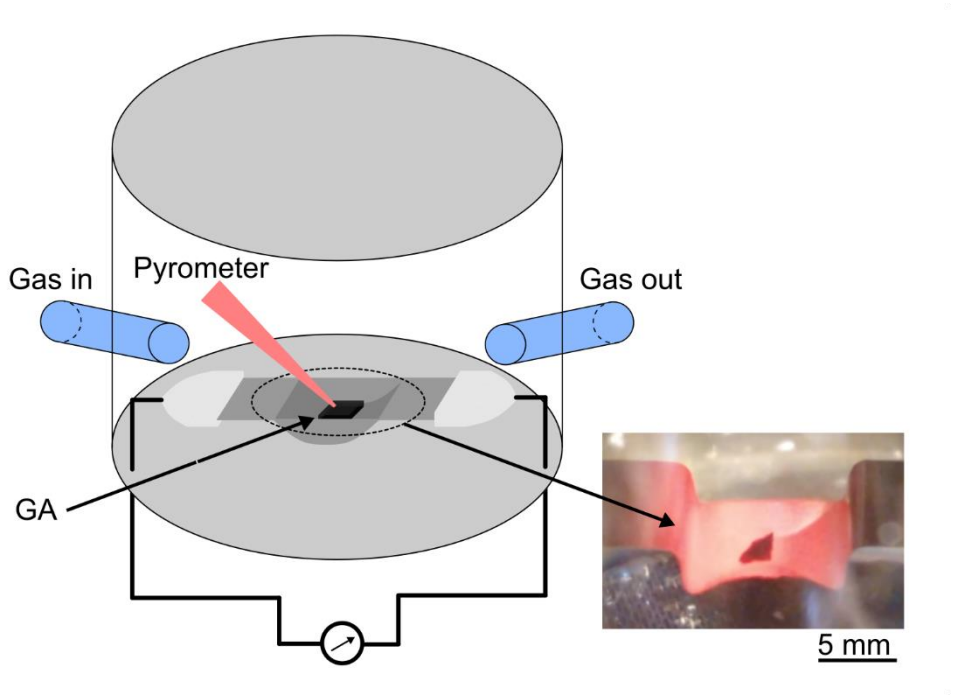

Figure 6.1 Schematic of a homemade setup used for heat resistance testing of GA specimens using a heated tungsten boat in air mixed with CO_2. The optical image on the right shows a glowing boat with a GA sample heated to 650 °C.

6.3 Thermal conductivity of graphene aerogel

The thermal conductivity of the GA was measured using LFA. Even though graphene is one of the best thermally conductive materials with thermal conductivity of around 4000 $W.m^{-1}.K^{-1}$,[40] the thermal conductivity of the GA was found to be 0.026 $W.m^{-1}.K^{-1}$ at room temperature. The comparison of the thermal conductivity measured in this work with different low thermally conductive materials is shown in Figure 6.2a. The temperature dependence of the thermal conductivity measured by LFA is shown in Figure 6.2b. The thermal conductivity demonstrates a steady growth from 0.019 $W.m^{-1}.K^{-1}$ at 180 K to

0.068 $W.m^{-1}.K^{-1}$ at 1300 K. In the temperature range of 300-1300 K, the thermal conductivity increased only 2.5 times, demonstrating very low thermal conductivity both at low and high temperatures.

Heat transfer through porous materials can be considered as a combination of solid, gaseous, and radiant thermal conductivity mechanisms.[41] The GA, due to its extremely low density and perfect opacity, depresses all of these three types of heat flow mechanisms.[42–44] Therefore the GA exhibits the thermal conductivity in the range of air and other highly insulating materials such as cork, styrofoam, and other reported graphene aerogels.[34,35,44,45,46,47,48] The lowest reported thermal conductive solid-state material at room temperature has also been graphene aerogel with thermal conductivity of 0.005 $W.m^{-1}.K^{-1}$.[35] However, the thermal conductivity of this sample was measured at a low pressure of 6.7×10^{-4} mBar, which means that the thermal conductivity at the atmospheric pressure must have been slightly higher.

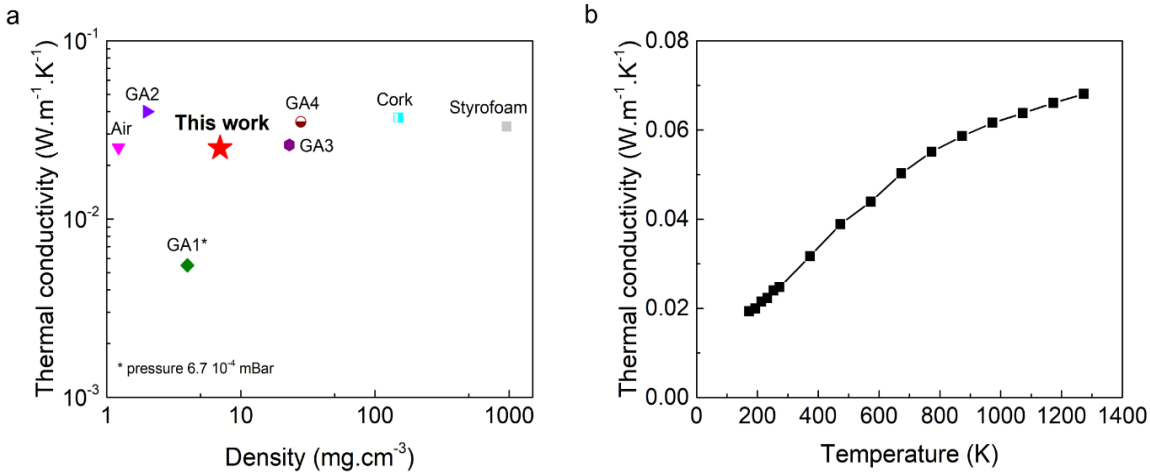

Figure 6.2 Thermal conductivity determination. (a) Comparison of thermal conductivity of graphene aerogels (GA1-4),[34,35,44,45] cork,[46] styrofoam,[47] and air [48] as a function of density. (b) Temperature dependence of thermal conductivity of the GA.

6.4 Fire resistance of graphene aerogel

6.4.1 Flame resistance of graphene and graphene aerogel in propane flame

In Figure 6.3, the fire resistance of monolayer graphene on SiO_2 is compared with the GA upon flame exposure in air. Monolayer graphene was grown by CVD on copper and

transferred on a 90 nm SiO_2 layer on silicon.[49] The monolayer graphene had a polycrystalline character with the size of crystallites of the order of 10 µm. Flame resistance testing using propane flame exposure to the samples at a fixed distance in combination with scanning electron and optical microscopy and Raman spectroscopy analysis were carried out.

The flame resistance tests revealed significantly different behavior for graphene aerogels to monolayer graphene on SiO_2 (Figure 6.3). SEM imaging showed the graphene aerogels to resist the propane flame for 50 s (Figure 6.3b). No modification of the graphene sheets in the GA structure was observed after the flame exposure at a temperature of 1200 °C, even in the high-resolution SEM images. The macroscopic mechanical properties of the aerogels were unaffected by the flame as well, demonstrating superelastic behavior both before and after the flame exposure. In contrast, monolayer graphene on a SiO_2 subjected to a propane burner started to burn immediately after the flame exposure and disappeared completely within 5 s (Figure 6.3c). Although previous studies of graphene aerogels have shown their ability to partially resist flames at 500 °C,[34] such a long and high-temperature resistance of graphene aerogels to flame has not been observed yet. The observed high flame resistance of our graphene aerogel is attributed to its high crystallinity, low amount of oxygen defects and other effects as discussed in detail below.

Raman spectroscopy of monolayer graphene revealed significant changes to the graphene Raman bands for the sample exposed to the flame (Figure 6.3f). After 1 s, a prominent D band evolved in the sample, and the G and 2D bands widened, providing evidence of defect formation in the graphene lattice. The monolayer graphene completely burned down in a few seconds. No graphene-like bands were observed in the Raman spectra after 5 s of flame exposure. This is considerably different from the Raman investigation of graphene aerogels exposed to the flame in Figure 6.3e. The G and 2D bands of the graphene aerogel were not affected by the propane flame even after 50 s exposure, despite its crystal structure is not as good as the monolayer graphene. There was only observed a minor rise of the D band, most probably due to the saturation of defects by oxygen at the edges of graphene flakes in the aerogel. The results show distinctly different flame resistance behaviors of the graphene on a substrate and the graphene aerogel, highlighting the critical role of the arrangement of graphene flakes in the flame resistance of graphene. While free-standing graphene flakes in the graphene aerogel are non-flammable, graphene on a substrate is prone to rapid combustion in the flame.

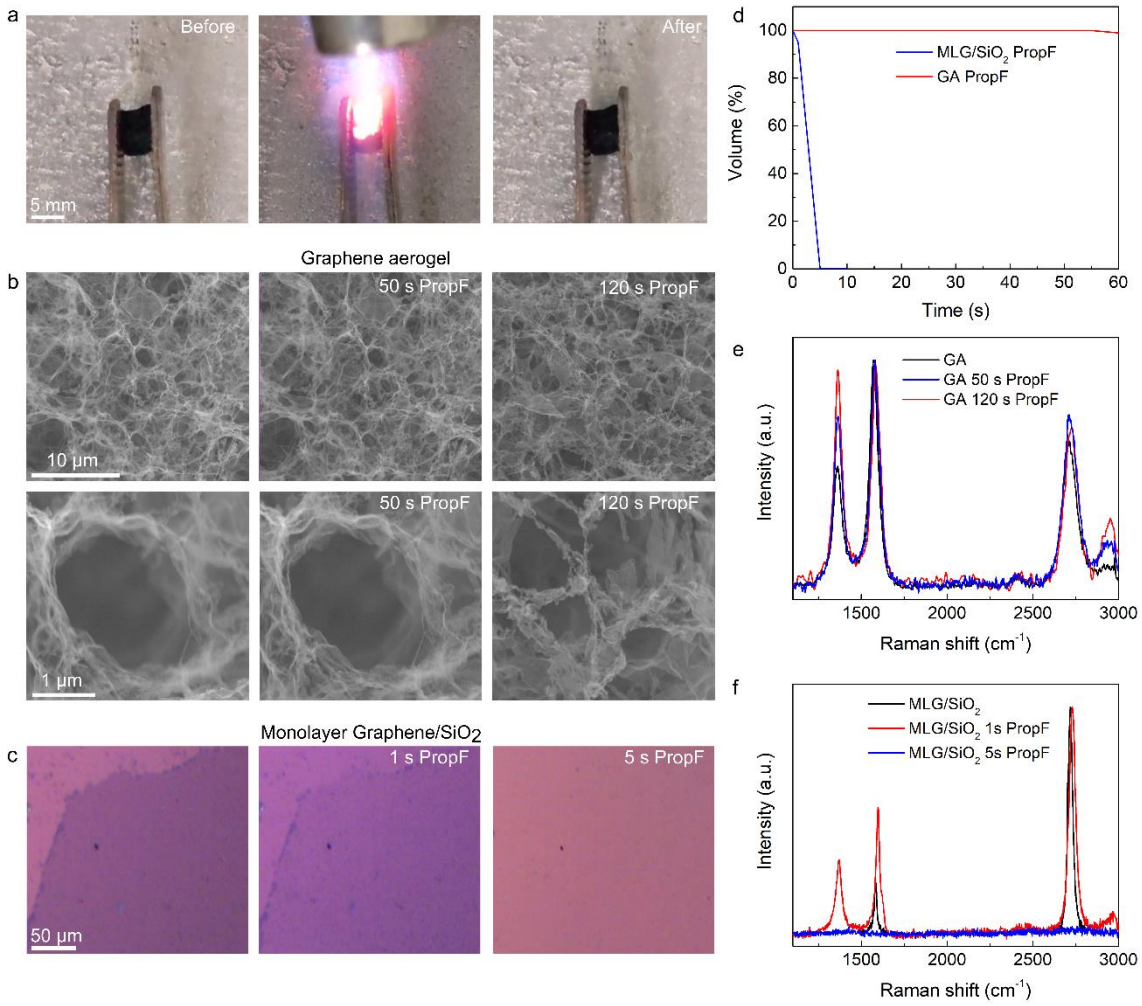

Figure 6.3 Flame resistance testing of the graphene aerogel (GA) and monolayer graphene on SiO_2 using a propane flame. (a) Demonstration of graphene aerogel interaction with the propane flame for 30 s. (b) SEM micrographs showing the same spots on the graphene aerogel before and after exposing it to the propane flame for 50 s and 120 s. (c) Optical images of monolayer graphene on SiO_2 before and after the exposure to the propane flame for 1 and 5 s. (d) Volume changes of the graphene aerogel (GA) and monolayer graphene (MLG) after propane flame exposure. Raman spectra of (e) the graphene aerogel and (f) the graphene on SiO_2 before and after subjecting it to the propane flame.

6.4.2 Combustion of graphene and graphene aerogel in various flames

A detailed study of the flame resistance and burning behavior of graphene aerogels in different types of flames is presented in Figure 6.4. The testing of the samples was carried out using hydrogen, propane, candle, and IPA flames. The exposure of the graphene

aerogels to the flames is illustrated in Figure 6.4a. Each of the flames induced a different temperature on the surface of the sample. The sample temperature was 550, 800, 1200, and 1500 °C for IPA, candle, propane, and hydrogen flames, respectively. The temperature was calibrated using a thermocouple. Thermal camera imaging revealed a significant temperature gradient across the graphene aerogel exposed to the flames (Figure 6.4b). The temperature dropped from 1500 °C on one side of the sample over a 5 mm thick graphene aerogel down to room temperature on the other side of the sample, demonstrating effective shielding of the heat from the high-temperature flame. Such a high gradient is attributed to an extremely low thermal conductivity of the graphene aerogel, as has been reported in previous studies.[35]

The burning process of the graphene aerogel consists of two phases (Figure 6.4c). In phase 1, graphene aerogel resists the flame, demonstrating self-extinguishing behavior with no observable change in the size and material properties. The time of the flame resistance phase is found to decrease with increasing temperature (inset in Figure 6.4c). In a hot hydrogen flame at 1500 °C, the resistant phase lasted only for 40 s. While it was longer in the low-temperature IPA flame, in which the graphene aerogel remained unchanged at 550 °C after an hour of exposure. In phase 2, graphene aerogel starts to burn, and a reduction of the sample volume is observed (Figure 6.4c). The combustion of graphene flakes happens at the surface of the aerogel in the area with the highest temperature and slowly proceeds towards the interior of the aerogel. In this phase, there is also observed an increase in the D band in Raman spectroscopy (Figure 6.3e), which confirms the formation of defects in the free-standing graphene flakes during burning. Interestingly, no transition from phase 1 to phase 2 was observed in the IPA flame, which suggests that graphene aerogels can become fire-resistant under specific conditions.

The burning rate of the graphene aerogel exhibits roughly a linear relationship with time for all tested flames (Figure 6.4d). As expected, the burning rate is slower at low temperatures and increases in hot flames. Even though graphene aerogel could resist the flames for longer and at higher temperatures than graphene on a substrate, the burning rate of the graphene aerogel is found to be an order of magnitude higher than that of the monolayer graphene on SiO_2. This can be explained by the fact that reactive oxidation species in the flame can access both sides of the free-standing graphene walls in the graphene aerogel, whereas the substrate protects one side of graphene on SiO_2. Therefore, the collision probability of the reactive oxidation species is higher in free-standing graphene, which leads to a faster burning rate.

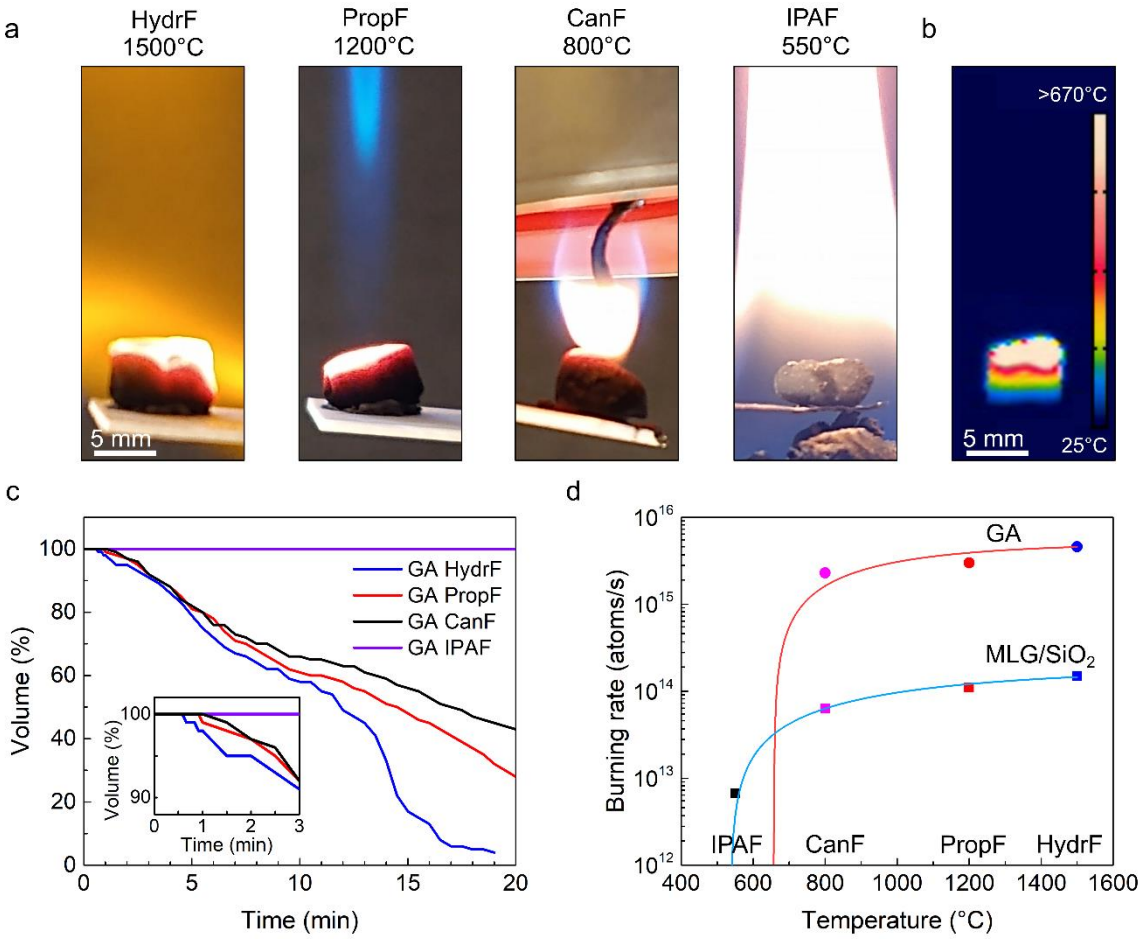

Figure 6.4 Flame resistance and burning behavior of graphene aerogels (GA) in different types of flames. (a) Illustration of different flames used in burning experiments. (b) Thermal imaging of graphene aerogel when exposed to a hydrogen flame using an infrared (IR) camera. (c) Volume changes of graphene aerogels after exposing them to different flames. (d) Burning rate of graphene aerogel and monolayer graphene on SiO_2 as a function of temperature and flame type.

6.4.3 Fire resistance of graphene aerogel to low-temperature flames

Of particular interest is the remarkably high resistance of graphene aerogels to the IPA flame, in which no burning of the sample was observed at 550 °C even after hours of exposure to the reactive flame containing oxidizing ions and radicals. To gain more insight into this unusual behavior, we examine the difference between graphene aerogel and graphene on SiO_2 after the IPA flame exposure using optical microscopy, SEM, and Raman spectroscopy in Figure 6.5. Both Raman spectroscopy and SEM micrographs confirm that the structure of the graphene aerogel was not affected by placing it in the IPA

flame for 60 minutes (Figure 6.5a,b). On the other hand, graphene on SiO_2 demonstrates rapid degradation when exposed to the same IPA flame (Figure 6.5c,d), similarly to the propane flame (6.3c,f). The optical images show that graphene on SiO_2 is significantly etched away after 10 s, as seen by the disappearance of graphene near the straight scratches and the appearance of bright spots on the surface. The graphene layer completely disappears in the flame after 80 s. The observed dark layer on the surface after 120 s corresponds to soot from the incomplete burning of IPA flame. Raman spectroscopy reveals that the burning of the monolayer graphene results in a decrease of the 2D peak, broadening of the G peak, and rise of the D peak (Figure 6.5d). The broad D and G bands seen in the spectra at 10-120 s correspond to a non-graphene-like Raman spectrum of the soot. This is in striking contrast to the graphene aerogel exposed to the IPA flame (Figure 6.5b), where no change in the Raman spectra is observed even after 60 minutes of the exposure.

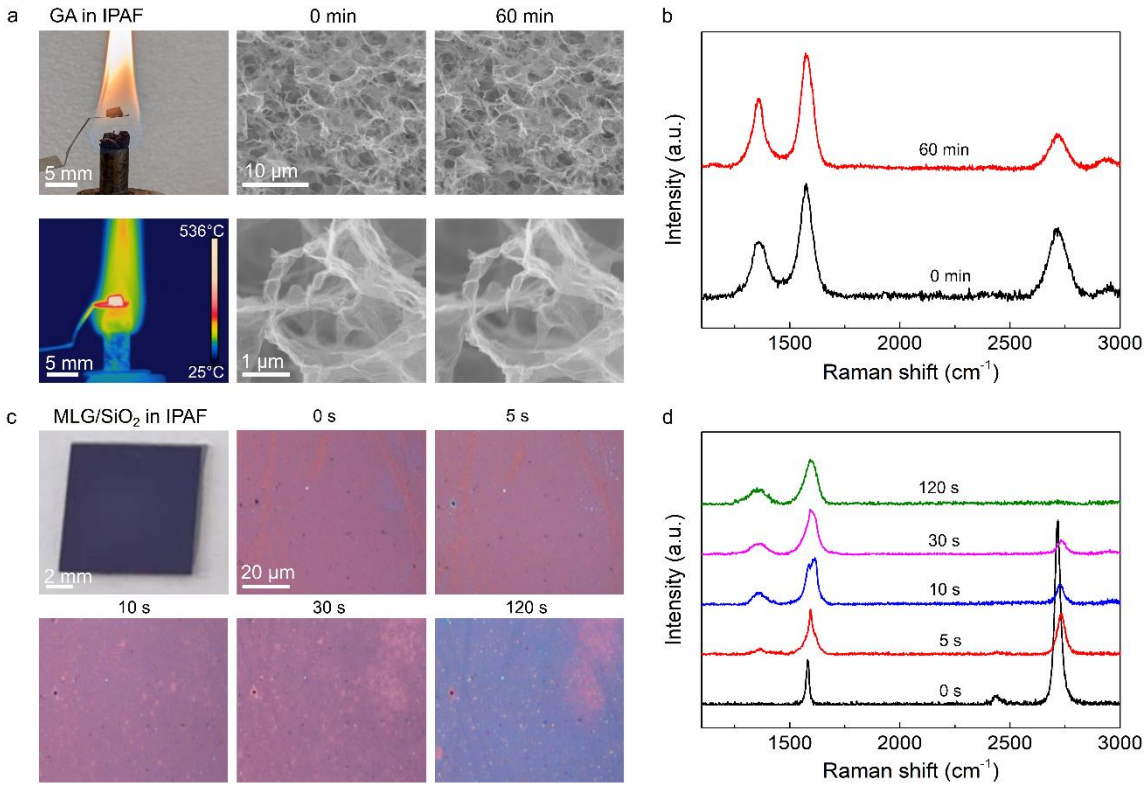

Figure 6.5 Flame resistance testing of the graphene aerogel (GA) and monolayer graphene on SiO_2 using an isopropanol flame (IPAF). (a) Optical, IR, and SEM images of a graphene aerogel exposed to the IPA flame for 60 minutes. (b) Raman spectra of the graphene aerogel before and after the exposure to the IPA flame. (d) Optical images and (e) Raman spectra of monolayer graphene on SiO_2 exposed to the IPA flame for different time periods.

6.4.4 Elemental analysis of graphene aerogel exposed to flames

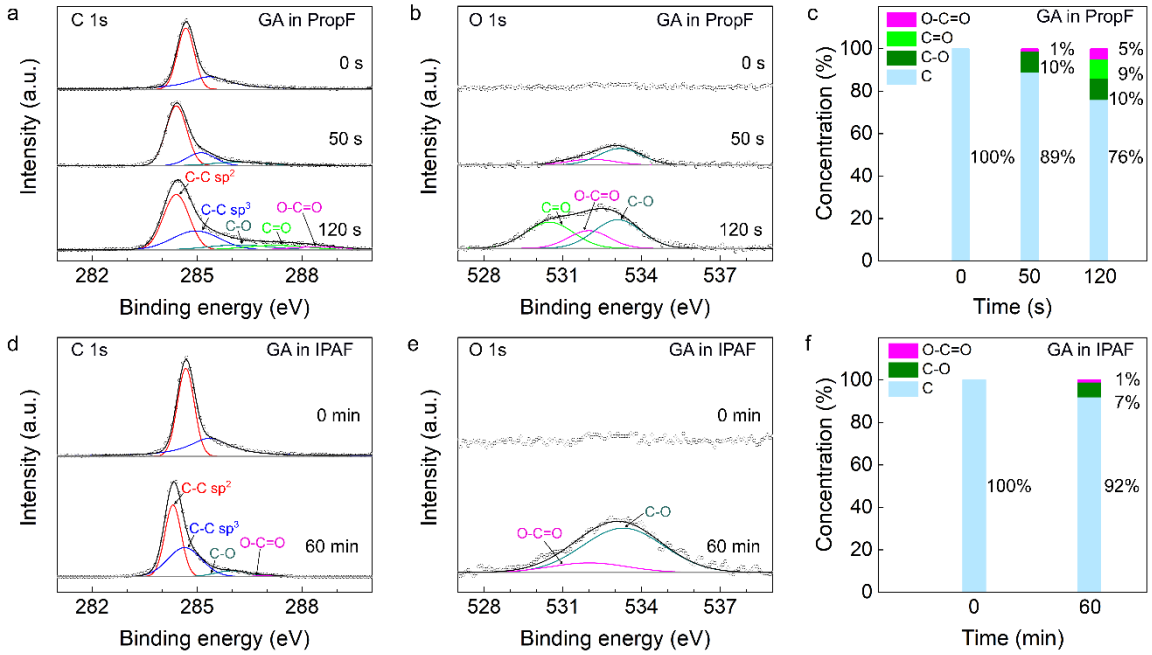

Figure 6.6 X-ray photoelectron spectroscopy analysis of graphene aerogels exposed to propane and IPA flames. (a) C 1s and (b) O 1s spectra of a graphene aerogel exposed to a propane flame. (c) Evolution of the concentration of carbon and different oxygen bonds in the graphene aerogel exposed to the propane flame as a function of time. (d) C 1s and (e) O 1s spectra of a graphene aerogel exposed to an IPA flame. (f) Evolution of the concentration of carbon and different oxygen bonds in the graphene aerogel before and after the exposure to the IPA flame.

Figure 6.6 shows the elemental analysis of graphene aerogels exposed to propane and IPA flames using XPS. XPS reveals the evolution of carbon and oxygen bonding in the pristine and flame-exposed graphene aerogels during the flame-resistant phase (phase 1) and burning phase (phase 2). The typical signatures of phase 1 can be seen in the graphene aerogel exposed to the IPA flame for 60 min. The graphene aerogel exposed to propane flame shows both phases. Phase 1 is seen in the sample exposed to the propane flame for 50 s and phase 2 in the sample exposed for 120 s. The C 1s and O 1s spectra (C 1s and O 1s) of the pristine aerogel (0 s) show that the sample does not contain any oxygen prior to the flame exposure, only carbon. After exposing the aerogels to both the flames, the amount of oxygen increases. In phase 1, the oxygen content increases to 8-11%. The deconvolution analysis of the oxygen bonds shows that the majority comprises single-bonded oxygen to carbon (7-10%). There are also seen carboxyl bonds (1%), but no carbonyl bonds. In phase 2, the amount of carboxyl and carbonyl bonds increased

significantly to 9% and 5%, respectively, as seen in the sample exposed to the propane flame for 120 s. These data show a noticeable trend that the non-flammability is interconnected with the amount of double-bonded oxygen. Once there is no double-bonded oxygen or just fractions, the graphene aerogel survives in the flame. As soon as the amount of double-bonded oxygen is increased, the graphene aerogel starts to burn.

6.4.5 Thermal stability of graphene aerogel

Although the inability to form carbonyl defects in free-standing graphene can partially explain the fire resistance of the graphene aerogels, it cannot explain why they can survive highly oxidizing flames at temperatures well above the oxidation stability of graphene. To determine the thermal stability of graphene aerogels, we conducted thermogravimetric analysis (TGA) and combustion gas analysis under air, air/CO_2, Ar, Ar/O_2, CO_2, and CO_2/O_2 atmospheres (Figure 6.7). The atmospheres containing different concentrations of CO_2/O_2 were studied because carbon dioxide is the main product of the combustion of graphene and organic fuels in flames. Due to the porous structure of graphene aerogels, CO_2 might get trapped in the porous structure of graphene aerogel and reduce the amount of available oxygen during flame exposure. TGA and differential TGA (DTGA) curves reveal that the graphene aerogels have oxidation stability above 615 °C in Ar/O_2 (Figure 6.7a,b). The primary mass loss is observed in the range of 615-780 °C under the Ar/O_2 atmosphere. The small mass loss (10%) observed at lower temperatures is most probably caused by the desorption of the adsorbed molecules (H_2O and aromatic molecules) from the porous structure of the graphene aerogel. The combustion temperature of the graphene aerogel in a synthetic air atmosphere (20% of O_2 in Ar) is 670 °C. The combustion temperature was determined from the DTGA curves at a temperature with the maximum mass loss. Mass spectroscopy determined that the main combustion products of the graphene aerogel are CO_2 and H_2O. TGA and DTGA curves of the graphene aerogel heated under CO_2/O_2 and air/CO_2 atmospheres show that increasing CO_2 concentration and decreasing concentration of O_2 can significantly increase the combustion temperature of graphene aerogels. When the concentration of O_2 is decreased below 5% (Figure 6.7c,d), the combustion temperature of the graphene aerogel rises well above 700 °C. Similarly, the combustion temperature increases significantly in high concentrations of CO_2 in air when a graphene aerogel is heated on a heating element (Figure 6.7e,f). With the increasing amount of CO_2 in the reaction chamber up to 50%, the combustion temperature gradually rises from 725 to 815 °C. In a

pure CO_2 atmosphere, the combustion temperature was higher than the measurable limit (> 1000 °C).

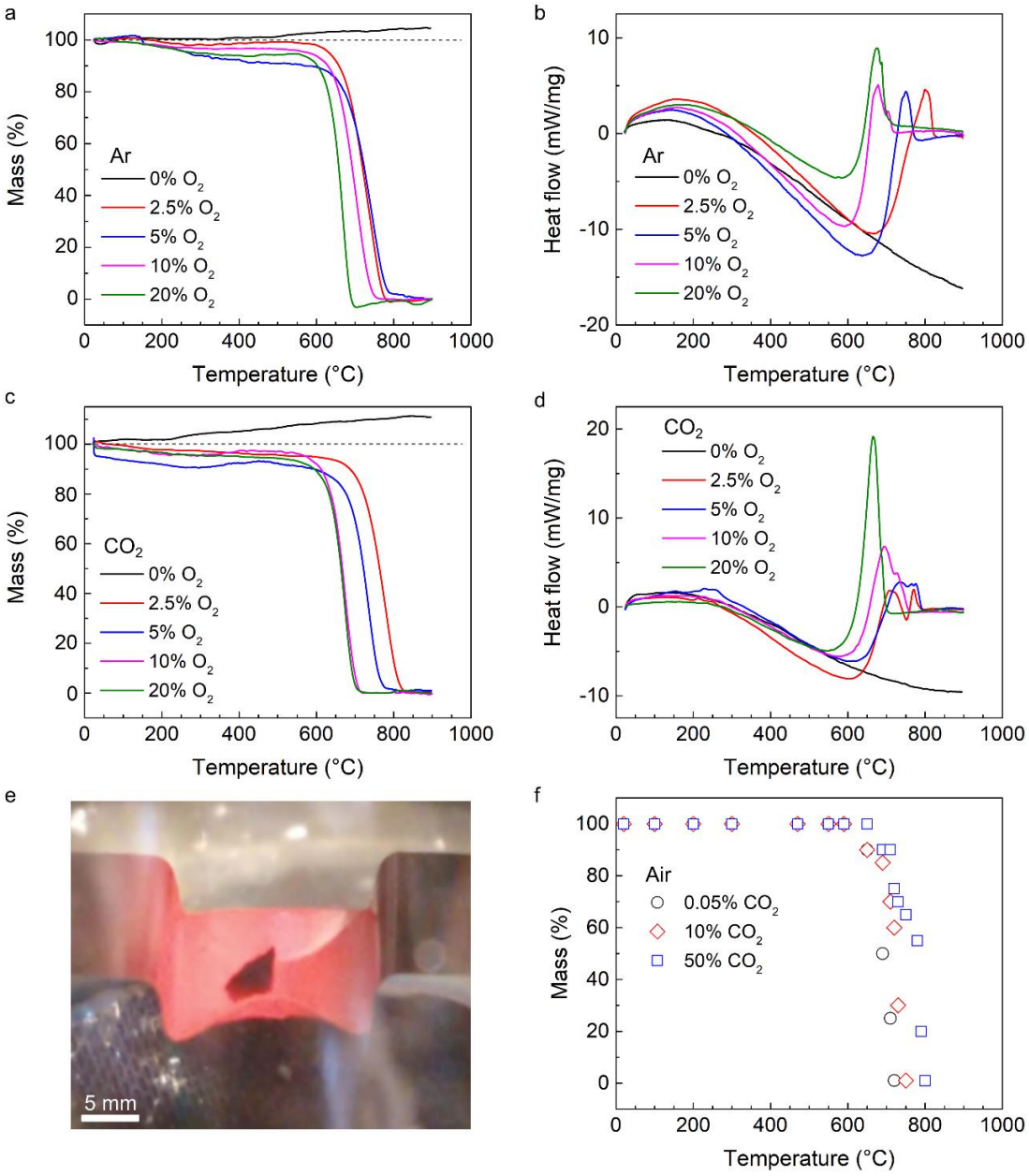

Figure 6.7 Thermogravimetric analysis of graphene aerogels under different atmospheres. (a) TGA and (b) DTGA graphs of graphene aerogel in an Ar atmosphere with a different oxygen concentration. (c) TGA and (b) DTGA graphs of graphene aerogel in a CO_2 atmosphere with a different oxygen concentration. (e) Optical image of a graphene aerogel sample heated on a tungsten heating element in a reaction chamber containing an air/CO_2 mixture. (f) Mass loss of graphene aerogel as a function of temperature in an air atmosphere with a different CO_2 concentration

6.4.6 Flame resistance and retardancy mechanism

The observed flame retardancy and resistance of graphene aerogels from 550 up to 1500 °C can be understood based on the combination of several effects, as schematically shown in Figure 6.8. Firstly, the pores on the surface of the graphene aerogel are filled by CO_2. They provide a non-flammable protective gas layer. The high concentration of CO_2 in the pores of the graphene aerogel blocks the supply of oxygen and restricts the combustion of graphene even at temperatures above its oxidation stability temperature. It is assumed that CO_2 is generated most probably from the burning of weekly bonded species (organic molecules) on the surface of the aerogel, which are decomposed at lower temperatures than graphene. This can also explain why graphene aerogel can survive in the hydrogen flame, whose combustion products do not involve CO_2. The second important effect involves the self-healing and self-extinguishing properties of graphene. Free-standing graphene plays a key role in this mechanism because it can suppress the creation of double-bonded oxygen groups on the surface, restricting the graphene combustion in the flame. The last important effect involves the extremely low thermal conductivity of graphene aerogels that provides effective thermal shielding of the subsurface material from the heat generated by the flame.

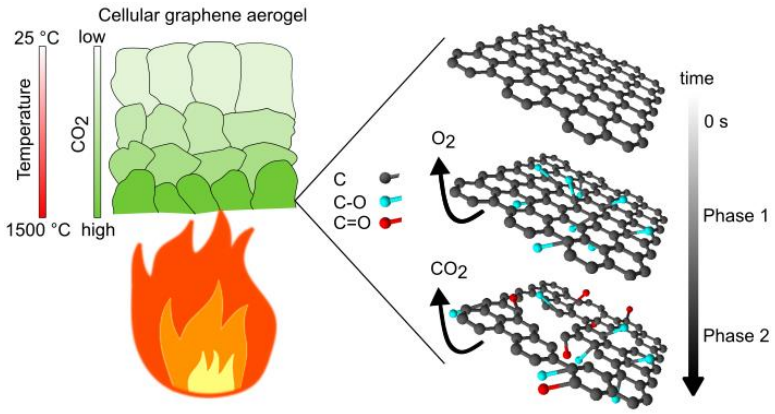

Figure 6.8 Schematic of the flame resistant and burning mechanisms in graphene aerogels. It shows a capture of CO_2 in the pores, which leads to a decrease in the oxygen levels in the material and the gas-phase flame-retardant mechanism in the graphene aerogels. The schematic on the right shows the atomic model of free-standing graphene before flame exposure in the fire-resistant (phase 1) and burning phases (phase 2).

6.5 Conclusions

In this chapter thermal properties of the GA were studied. The GA exhibits an extremely low thermal conductivity of 0.026 $W.m^{-1}.K^{-1}$, which is comparable with the lowest conductivity reported in 3D graphene materials in the literature. Therefore, the GA is highly thermally insulating and provides a huge temperature gradient. When one side of the GA sample is heated to 1500 °C, it shows room temperature on the other side for a thickness over a 5 mm.

The flammability and the behavior of the GA under flame exposure in air was deeply studied. It was found that the burning of the GA consists of two phases. In the first flame resistant phase, there is not even a microscopic change in the 3D structure, and the GA can resist the flame. The length of the flame resistance is dependent on the temperature. The GA can resist flame at 1500 °C for at least 40 s, while the GA can sustain in the flame with a temperature of 550 °C for at least 60 min without any damage. In the second phase, the GA starts to slowly burn with a burning rate in the range of 10^{15} $atoms.s^{-1}$. This observation is different than for monolayer graphene on a substrate. The burning of the monolayer graphene in flame contains only the second burning phase, or if there is also a non-burning phase, it is shorter than 1 s. On the other hand, the burning rate for monolayer graphene is of around 10^{13} $atoms.s^{-1}$, which is slower than the GA. Interestingly, the GA can sustain in the flame without any damage above the oxidation temperature of monolayer graphene. This is because the oxidation temperature of the GA determined using TGA under Ar/O_2 atmosphere is around 615 °C.

The explanation of the unique non-burning phase and the flame resistance of the GA was proposed as a combination of several effects, including low thermal conductivity, pores filled with CO_2, and a self-healing defect mechanism. The presence of the non-burning phase and huge temperature gradient gives an opportunity to use the GA as a fire protective material for tools, clothes, materials, and devices. The results also provide important guidelines for designing other carbon-based flame resistant and retardant materials.

References

1. Lazar, S. T., Kolibaba, T. J. & Grunlan, J. C. Flame-retardant surface treatments. *Nat Rev Mater* **5**, 259–275 (2020).

2. Li, X., Dong, G., Liu, Z. & Zhang, X. Polyimide Aerogel Fibers with Superior Flame Resistance, Strength, Hydrophobicity, and Flexibility Made via a Universal Sol–Gel Confined Transition Strategy. *ACS Nano* **15**, 4759–4768 (2021).
3. Köklükaya, O., Carosio, F., Grunlan, J. C. & Wågberg, L. Flame-Retardant Paper from Wood Fibers Functionalized via Layer-by-Layer Assembly. *ACS Appl. Mater. Interfaces* **7**, 23750–23759 (2015).
4. Meng, D. *et al.* Self-healing polyelectrolyte complex coating for flame retardant flexible polyurethane foam with enhanced mechanical property. *Composites Part B: Engineering* **219**, 108886 (2021).
5. Chen, S., Li, X., Li, Y. & Sun, J. Intumescent Flame-Retardant and Self-Healing Superhydrophobic Coatings on Cotton Fabric. *ACS Nano* **9**, 4070–4076 (2015).
6. Pethsangave, D. A., Khose, R. V., Wadekar, P. H. & Some, S. Novel Approach toward the Synthesis of a Phosphorus-Functionalized Polymer-Based Graphene Composite as an Efficient Flame Retardant. *ACS Sustainable Chem. Eng.* **7**, 11745–11753 (2019).
7. Li, Y.-C. *et al.* Flame Retardant Behavior of Polyelectrolyte−Clay Thin Film Assemblies on Cotton Fabric. *ACS Nano* **4**, 3325–3337 (2010).
8. Seo, H. J. *et al.* Enhancing the flame-retardant performance of wood-based materials using carbon-based materials. *J Therm Anal Calorim* **123**, 1935–1942 (2016).
9. Babu, K. *et al.* A Review on the Flammability Properties of Carbon-Based Polymeric Composites: State-of-the-Art and Future Trends. *Polymers (Basel)* **12**, 1518 (2020).
10. Ahankari, S., Paliwal, P., Subhedar, A. & Kargarzadeh, H. Recent Developments in Nanocellulose-Based Aerogels in Thermal Applications: A Review. *ACS Nano* **15**, 3849–3874 (2021).
11. Salmeia, K. A., Fage, J., Liang, S. & Gaan, S. An Overview of Mode of Action and Analytical Methods for Evaluation of Gas Phase Activities of Flame Retardants. *Polymers* **7**, 504–526 (2015).
12. Schartel, B. *et al.* Flame Retardancy of Polymers: The Role of Specific Reactions in the Condensed Phase. *Macromolecular Materials and Engineering* **301**, 9–35 (2016).
13. Cao, X., Lu, K. & Li, Y. Isolated Protective Char Layers by Nanoclay Network: Significantly Improved Flame Retardancy and Mechanical Performance of TPV/MH Composites by Small Amount of Nanoclay. *Ind. Eng. Chem. Res.* **54**, 6912–6921 (2015).
14. Ishimaru, K., Hata, T., Bronsveld, P., Nishizawa, T. & Imamura, Y. Characterization of sp2- and sp3-bonded carbon in wood charcoal. *J Wood Sci* **53**, 442–448 (2007).

15. Gan, W. *et al.* Dense, Self-Formed Char Layer Enables a Fire-Retardant Wood Structural Material. *Advanced Functional Materials* **29**, 1807444 (2019).
16. Lin, B. *et al.* Experimental and numerical perspective on the fire performance of MXene/Chitosan/Phytic acid coated flexible polyurethane foam. *Sci Rep* **11**, 4684 (2021).
17. Ma, Z. *et al.* Formation of an external char layer during subcritical water hydrolysis of biomass. *Sustainable Energy Fuels* **1**, 1950–1959 (2017).
18. Xue, B. *et al.* Influence of graphitization degree of carbon microspheres on properties of PET flame retardant. *Polymer Engineering & Science* **58**, 1399–1408 (2018).
19. Araby, S. *et al.* Recent advances in carbon-based nanomaterials for flame retardant polymers and composites. *Composites Part B: Engineering* **212**, 108675 (2021).
20. Jeong, Y. R. *et al.* Highly Stretchable and Sensitive Strain Sensors Using Fragmentized Graphene Foam. *Advanced Functional Materials* **25**, 4228–4236 (2015).
21. Weng, D. *et al.* Review on synthesis of three-dimensional graphene skeletons and their absorption performance for oily wastewater. *Environ Sci Pollut Res* **28**, 16–34 (2021).
22. Liu, Z. F. *et al.* Hierarchically buckled sheath-core fibers for superelastic electronics, sensors, and muscles. *Science* **349**, 400–404 (2015).
23. Cui, G. *et al.* A comprehensive review on graphene-based anti-corrosive coatings. *Chemical Engineering Journal* **373**, 104–121 (2019).
24. Nine, M. J., Cole, M. A., Tran, D. N. H. & Losic, D. Graphene: a multipurpose material for protective coatings. *J. Mater. Chem. A* **3**, 12580–12602 (2015).
25. Kausar, A., Rafique, I., Anwar, Z. & Muhammad, B. Recent Developments in Different Types of Flame Retardants and Effect on Fire Retardancy of Epoxy Composite. *Polymer-Plastics Technology and Engineering* **55**, 1512–1535 (2016).
26. Qi, B. *et al.* Mechanical and thermal properties of epoxy composites containing graphene oxide and liquid crystalline epoxy. *Fibers Polym* **15**, 326–333 (2014).
27. Liu, F., Wang, M., Chen, Y. & Gao, J. Thermal stability of graphene in inert atmosphere at high temperature. *Journal of Solid State Chemistry* **276**, 100–103 (2019).
28. Nan, H. Y. *et al.* The thermal stability of graphene in air investigated by Raman spectroscopy. *Journal of Raman Spectroscopy* **44**, 1018–1021 (2013).

29. Shang, N. G. *et al.* Controllable selective exfoliation of high-quality graphene nanosheets and nanodots by ionic liquid assisted grinding. *Chem. Commun.* **48**, 1877–1879 (2012).
30. Farivar, F. *et al.* Unlocking thermogravimetric analysis (TGA) in the fight against “Fake graphene” materials. *Carbon* **179**, 505–513 (2021).
31. Lee, W., Kihm, K. D. & Ko, S. H. Thermal conductivity reduction of multilayer graphene with fine grain sizes. *JMST Adv.* **1**, 191–195 (2019).
32. Shahil, K. M. F. & Balandin, A. A. Thermal properties of graphene and multilayer graphene: Applications in thermal interface materials. *Solid State Communications* **152**, 1331–1340 (2012).
33. Chen, W. *et al.* The preparation and application of a graphene-based hybrid flame retardant containing a long-chain phosphaphenanthrene. *Sci Rep* **7**, 8759 (2017).
34. Cheng, Y. *et al.* Enhanced mechanical, thermal, and electric properties of graphene aerogels via supercritical ethanol drying and high-temperature thermal reduction. *Sci Rep* **7**, 1439 (2017).
35. Xie, Y. *et al.* Interface-mediated extremely low thermal conductivity of graphene aerogel. *Carbon* **98**, 381–390 (2016).
36. Li, J. *et al.* Ultra-light, compressible and fire-resistant graphene aerogel as a highly efficient and recyclable absorbent for organic liquids. *J. Mater. Chem. A* **2**, 2934–2941 (2014).
37. Wang, Z. *et al.* Ultralight, highly compressible and fire-retardant graphene aerogel with self-adjustable electromagnetic wave absorption. *Carbon* **139**, 1126–1135 (2018).
38. Hu, C. *et al.* Scalable Preparation of Multifunctional Fire-Retardant Ultralight Graphene Foams. *ACS Nano* **10**, 1325–1332 (2016).
39. Picard, S., Burns, D. T. & Roger, P. Determination of the specific heat capacity of a graphite sample using absolute and differential methods. *Metrologia* **44**, 294–302 (2007).
40. Cai, W. *et al.* Thermal Transport in Suspended and Supported Monolayer Graphene Grown by Chemical Vapor Deposition. *Nano Lett.* **10**, 1645–1651 (2010).
41. Kang, S., Choi, J. Y. & Choi, S. Mechanism of Heat Transfer through Porous Media of Inorganic Intumescent Coating in Cone Calorimeter Testing. *Polymers* **11**, 221 (2019).
42. Lu, X., Nilsson, O., Fricke, J. & Pekala, R. W. Thermal and electrical conductivity of monolithic carbon aerogels. *Journal of Applied Physics* **73**, 581–584 (1993).

43. Lu, X. *et al.* Thermal Conductivity of Monolithic Organic Aerogels. *Science* **255**, 971–972 (1992).
44. Yue, C., Feng, J., Feng, J. & Jiang, Y. Low-thermal-conductivity nitrogen-doped graphene aerogels for thermal insulation. *RSC Adv.* **6**, 9396–9401 (2016).
45. Tang, G. *et al.* Three dimensional graphene aerogels and their electrically conductive composites. *Carbon* **77**, 592–599 (2014).
46. Limam, A., Zerizer, A., Quenard, D., Sallee, H. & Chenak, A. Experimental thermal characterization of bio-based materials (Aleppo Pine wood, cork and their composites) for building insulation. *Energy and Buildings* **116**, 89–95 (2016).
47. Han, W. *et al.* Enhanced thermal conductivity of commercial polystyrene filled with core-shell structured BN@PS. *Composites Part A: Applied Science and Manufacturing* **102**, 218–227 (2017).
48. Ganta, D., Dale, E. B., Rezac, J. P. & Rosenberger, A. T. Optical method for measuring thermal accommodation coefficients using a whispering-gallery microresonator. *J. Chem. Phys.* **135**, 084313 (2011).
49. Dontschuk, N. *et al.* A graphene field-effect transistor as a molecule-specific probe of DNA nucleobases. *Nat Commun* **6**, 6563 (2015).

7 Summary

This thesis is focused on the transformation of graphene into three-dimensional material. Here, graphene aerogel was chosen as the most appropriate form of three-dimensional graphene because it offers extremely low density and high porosity. A template-free synthesis method of covalently cross-linked graphene aerogels is developed using hydrothermal synthesis, freeze-drying, and high-temperature annealing. The method converts graphene oxide into 3D graphene aerogel. The method can control the resulting properties of the aerogel by tuning the density, amount of carbon, oxygen and defects, and bonding among individual graphene sheets. The as-prepared graphene aerogel was characterized using SEM, Raman scattering, XPS, FTIR, and XRD. The thesis also investigated its mechanical, electrical and thermal properties and resistance against fire. The graphene aerogel demonstrates unique properties in all these areas. The unique properties originate from the combination of the properties of individual atomically thin graphene sheets, the interaction between them, and the cellular structure of the aerogel. The thesis provides a new strategy for transferring properties of two-dimensional material into a macroscopic form, opening new possibilities for developing new advanced light-weight materials and devices which can be used in various biomedical, engineering and electronic applications.

The fabricated graphene aerogel exhibits mechanical robustness and especially superelastic behavior over a wide range of strain and stress. The demonstrated strength and elastic range exceed all previously reported 3D graphene structures. The elastic limit of the graphene aerogel is found at 4.5 GPa at 92% of a strain in compression. In tension, this material exhibits the most considerable elastic deformation up to 68% of strain, with an elastic yield strength of 0.6 MPa. The high strength in tension provides indirect proof of the creation of covalent cross-linking in the aerogels because no other bond would be able to sustain such high stress. Moreover, the aerogel demonstrates an immediate elastic response to the applied force when deformed. The response time of the aerogel was found in the range of nanoseconds, which is much faster than in other 3D graphene structures. This property is explained by the ability to elastically damp mechanical vibration using elastic scattering of mechanical waves in the material. The unusual elastic properties of the graphene aerogels are explained by a new analytical model based on the gradual buckling of individual pores. This model fits the experimental data and provides new insight into the deformation mechanism of graphene aerogels under compression.

The graphene aerogel, when subjected to deformation, changes its electrical conductivity. This feature is used for the construction of pressure/strain sensors. The major advances of the sensor based on the graphene aerogel are a wide range of pressure/strain, an ultrafast response time of 5.2×10^{-4} s, high sensitivity with a gauge factor of 11.6 in the compression and 3.4 in the tensile mode, the detection limit of 326 μN, and high durability of more than 5000 compression cycles. These parameters qualify the sensor for monitoring various human bodily actions and robotic applications. These remarkable sensing properties are not only caused by the graphene aerogel itself but also due to a new type of sensing mechanism in these sensors. The new sensing mechanism is based on the mechanically variable contact resistance between the graphene aerogel and solid metal contacts. It is demonstrated that this mechanism can cover a much wider pressure range than other common mechanisms which are based on the change in the bulk material´s conductivity.

The graphene aerogel possesses extremely low thermal conductivity of 0.026 $W.m^{-1}.K^{-1}$ in air, which is one of the lowest conductivity within 3D graphene structures. It also exhibits exceptional fire resistance and self-extinguishing behavior. This fire-resistant mechanism consists of two phases, where the material in phase 1 resists even hydrogen flame (1500 °C on the surface) for 40 s. In phase 2, the graphene aerogel starts to burn slowly. The presence of the non-burning phase 1 was explained by a combination of extremely low thermal conductivity, 3D porous structure, and capturing the CO_2 molecules into pores. The results provide important guidelines for designing highly flame-resistant carbon-based materials which can be used in many industrial, academic, and life safety applications.

The thesis explored several exciting properties of the covalently cross-linked graphene aerogels. It is anticipated that future studies of these materials can improve their properties even further. Notably, it is worth trying to decrease the thermal conductivity of the graphene aerogel to obtain the most insulating material. Mechanical and electrical properties can also be improved by increasing the covalent crosslinking and decreasing porosity of the aerogels. It would be interesting to study the optical and magnetic properties of graphene aerogels in the future. The optical properties in the THz range of graphene aerogels might be particularly interesting because they fill the gap between the current electronic and photonic era. In this range, there is still a lack of devices/materials which can control and manipulate THz radiation. As the material is superelastic and possesses electromechanical behavior, optical properties under compression might also lead to some unique optomechanical behavior and devices.

List of publications related to the dissertation

Šilhavík, M.; Kumar, P.; Zafar, Z. A.; Míšek, M.; Čičala, M.; Piliarik, M.; Červenka, J. Anomalous Elasticity and Damping in Covalently Cross-Linked Graphene Aerogels. *Commun. Phys.* **2022**, *5* (1), 1–8.

Kumar, P.; Šilhavík, M.; Zafar, Z. A.; Červenka, J. Contact Resistance Based Tactile Sensor Using Covalently Cross-Linked Graphene Aerogels. *Nanoscale* **2022**, *14* (4), 1440–1451.*

**First two authors contributed equally to this work*

Šilhavík, M. et al. High-Temperature Fire Resistance and Self-Extinguishing Behavior of Cellular Graphene. ACS Nano – Under review.

List of patents related to the dissertation

Šilhavík, M., Kumar, P. Zafar, Z. A., Červenka, J. Highly Thermally Insulating and Electrically Conductive Graphene Aerogel and Method of Manufacturing Thereof. LU502730 – Pending.

Other publications

Zafar, Z. A.; Abbas, G.; Knizek, K.; Silhavik, M.; Kumar, P.; Jiricek, P.; Houdková, J.; Frank, O.; Cervenka, J. Chaotropic Anion Based “Water-in-Salt” Electrolyte Realizes a High Voltage Zn–Graphite Dual-Ion Battery. *J. Mater. Chem. A* **2022**, *10* (4), 2064–2074.

Zafar, Z. A.; Abbas, G.; Silhavik, M.; Knizek, K.; Kaman, O.; Sonia, F. J.; Kumar, P.; Jiricek, P.; Houdková, J.; Frank, O.; Cervenka, J. Reversible Anion Intercalation into Graphite from Aluminum Perchlorate “Water-in-salt” Electrolyte. *Electrochimica Acta* **2022**, *404*, 139754.

Hývl, M.; Müller, M.; Stuchlíková, T.-H.; Stuchlík, J.; Šilhavík, M.; Kočka, J.; Fejfar, A.; Červenka, J. Nucleation and Growth of Metal-Catalyzed Silicon Nanowires under Plasma. *Nanotechnology* **2020**, *31* (22), 225601.

Šilhavík, M.; Müller, M.; Stuchlík, J.; Stuchlíková, H.; Klementová, M.; Kočka, J.; Fejfar, A.; Červenka, J. Comparative Study of Catalyst-Induced Doping and Metal Incorporation in Silicon Nanowires. *Appl. Phys. Lett.* **2019**, *114* (13), 132103.

List of patents

Zafar, Z. A., Silhavik, M.; Cervenka, J.;An Aqueous-Based Energy Storage System Containing an Electrolyte of Metal Perchlorate. LU101731B1, October 14, 2021.

Conferences

Šilhavík, M., Levinský, P., Hejtmánek, J., Červenka, J. Probing Thermal Conductivity of Extremely Porous Media, oral presentation, Journée Virtuelle de la Thermoélectricité 2021, online, December 2021.

Šilhavík, M., Zafar, Z. A., Kumar, P., Červenka, J. Synthesis of Superelastic Graphene Aerogels, oral presentation, Virtual Graphene2021, online, November 2021.

Šilhavík, M., Zafar, Z. A., Červenka, J. The Role of High-Temperature Annealing on Graphene Aerogels, poster, 2019 MRS Fall Meeting, Boston, USA, December 2019.

Šilhavík, M., Zafar, Z. A., Červenka, J. The Role of High-Temperature Annealing on Graphene Aerogels, poster, Chem2Dmat 2019, Dresden, Germany, September 2019.

Šilhavík, M., Zafar, Z. A., Červenka, J. Catalyst-Induced Doping and Metal Incorporation in Silicon Nanowires, poster, ICN-T 2018, Brno, Czech Republic, July 2018.